NYUSIM User Manual

by
Shihao Ju, Shu Sun, and Theodore. S. Rappaport

Version 3.1
Copyright 2016 - 2022
New York University and NYU WIRELESS

January 12, 2022

NYUSIM — User License

Copyright (c) 2016 - 2022 New York University and NYU WIRELESS

NYUSIM Overview

Update: NYUSIM 3.1 January 12, 2022

NYU WIRELESS conducted millimeter-wave (mmWave) and sub-Terahertz (THz) measurements from 2012 through 2020, having acquired a total of over 1 TB of data, at frequencies from 28 to 142 GHz in various outdoor and indoor environments such as urban microcell (UMi), urban macrocell (UMa), rural macrocell (RMa), and indoor hotspot for office (InH). The measurements and analysis done in [1]–[21] led to the development of the NYUSIM channel simulator. Built upon the NYUSIM version 2.01, the new NYUSIM version 3.0 brings the capability of simulating wireless channels in the indoor office scenario for carrier frequencies from 500 MHz to 150 GHz.

NYUSIM provides an accurate rendering of actual channel impulse responses in both time and space, as well as realistic signal levels that were measured, and may be utilized to support realistic physical layer and link layer simulations such as those conducted in [8], [22]–[24]. The models and simulation approach in NYUSIM involves the research of more than a dozen graduate and undergraduate students, and as of 2021, over 80,000 downloads of NYUSIM have been recorded.

The current NYUSIM software package, version 3.0, extends the simulation scenario from outdoor to indoor environments developed based on the conventional drop-based statistical channel model. Previously, NYUSIM version 1.x implemented the initial drop-based channel model for outdoor scenarios for carrier frequencies from 0.5 GHz to 100 GHz [13], [25]. Then, NYUSIM version 2.x implemented a spatial consistency-enabled channel model with human blockage, and outdoor-to-indoor penetration loss modeling components for outdoor scenarios [14]–[16]. The new NYUSIM version 3.0 introduces the indoor scenario in the drop-based channel model and allows the carrier frequency range for the indoor scenario from 0.5 GHz to 150 GHz. Note that the frequency range from 100 to 150 GHz for outdoor scenarios and the spatial consistency mode for indoor scenario are not available yet and will be added in future releases.

It is worth noting that in the 3GPP TR 38.901 outdoor channel model for frequencies above 0.5 GHz [26]–[28], the number of clusters is unrealistically large. For example, in the UMi street canyon scenario, the number of clusters in the line-of-sight (LOS) environment is as high as 12, and 19 in the non-line-of-sight (NLOS) environment, which is not supported by the real-world measurements at mmWave bands [1]–[4]. In contrast, in the outdoor statistical spatial channel model (SSCM) implemented in NYUSIM [3], the number of time clusters ranges from 1 to 6, and the mean number of spatial lobes is about 2 and is upper-bounded by 5, which are obtained from field observations and are much smaller than those in the 3GPP channel model [8], [11], [13], [26].

Similarly, for the InH scenario in the 3GPP TR 38.901 indoor channel models, the number of clusters in the LOS and NLOS environments are set to 15

and 19, respectively, and the number of subpaths per cluster is 20. In contrast, the measurements conducted in a typical office environment showed that the maximum number of observed time clusters was 10 and 12 in the LOS and NLOS scenarios. Thus, the NYUSIM SSCM models the number of time clusters and the number of subpaths per cluster as random variables with mean 5.4 and 6.3 for the NLOS scenario, respectively [18]. The upper bounds of these channel statistics are determined from empirical measurements [7], [17], [18]. The impractical number of clusters in the 3GPP channel model is likely to result in a higher rank of mmWave channels, unrealistic eigen-channel distributions, and thereby inaccurate spectral efficiency prediction for 5G mmWave channels [8], [11].

Besides this user manual, five other files/folders are provided and available for download from the website: http://wireless.engineering.nyu.edu/5g-millimeter-wave-channel-modeling-software/. The other five files are listed and explained as follows:

☐ NYUSIM — Channel Model Simulator Application: A standalone application that contains a graphical user interface (GUI) for NYU's channel simulator, which will be detailed in the first two sections of this user manual. This application can run on computers with Windows 7 or higher and Mac operating systems (with or without MATLAB installed).

☐ Base Code: The MATLAB code used in the current version of NYUSIM to generate various channel parameters, which is created according to the mmWave broadband SSCM presented in [3]. The "Base Code" is applicable to arbitrary center carrier frequencies ranging from 500 MHz to 150 GHz, arbitrary RF bandwidths from 0 to 800 MHz, and multi-antenna systems. Additionally, atmospheric attenuation effects, which includes the attenuation induced by dry air (containing oxygen), vapor, haze/fog, and rain, are also considered in the path loss model in the "Base Code" (more details can be found in Section 3 of this user manual).

☐ Time cluster - spatial lobe approach to cluster any measured or Ray traced data: The MATLAB code implementing the time cluster - spatial lobe (TCSL) algorithm used in the SSCM [3], [27]. Both outdoor and indoor channel statistics were extracted using the TCSL algorithm [18], [25].

☐ User License: The user license for NYUSIM, which is also shown on the previous page of this user manual. This open-source license allows anyone to use and modify the code provided copyright notices and citations to the key papers of this work are provided. See the user license for specific terms.

☐ Application Example Code: The example MATLAB code for possible applications that make use of NYUSIM.

New Features in Version 3.1

NYUSIM 3.1 enables simultaneous channel simulations with different transmitter and receiver antenna polarizations. NYUSIM 3.0 and earlier can only simulate one polarization, either co-polarization or cross-polarization, for a single channel realization while NYUSIM 3.1 can simulate one polarization (co- or cross-polarization), two polarizations (co- and cross-polarizations), or four polarizations (namely, vertical-to-vertical (V-V), horizontal-to-horizontal (H-H), vertical-to-horizontal (V-H), and horizontal-to-vertical (H-V) polarizations) for every single channel realization.

Cross-polarization discrimination (XPD) is defined as the signal power attenuation (in dB) when the transmit antenna is vertically polarized and the receive antenna horizontally polarized (i.e., cross-polarization) compared to the case that both transmit and receive antennas are vertically or horizontally polarized (i.e., co-polarization) including channel effect. XPD values over microwave and millimeter-wave frequencies at various indoor and outdoor environments have been reported in the literature [2], [7], [18], [29]–[37], showing that the XPD increases as the carrier frequency increases. Thus, a linear function of frequency is used to fit the reported XPDs and calculate the XPD over the NYUSIM supported frequency range (500 MHz to 150 GHz). In addition, the XPDs are found larger in LOS environments than those in NLOS environments since the boresight path generally does not have a depolarization effect. Two linear functions with different values are used for the LOS and NLOS environments, respectively. A single XPD is applied to the total received power instead of different XPDs to different multipath components (MPCs) due to the limited available MPC-wise XPD values in the literature, which makes the the polarization model succinct yet valid.

Similarly, co-polarization discrimination (CPD) can be defined as the power difference (in dB) between the V-V and H-H polarization settings or the V-H and H-V polarization settings. The studies on the CPD are very limited [29], [33], [38], [39] and are commonly regarded as negligible, which leads to a simple model generating the H-H (H-V) power from the V-V (V-H) power by adding a zero-mean Gaussian random variable with a small standard deviation (1.6 dB used in NYUSIM 3.1).

Polarization has been widely used at mmWave frequencies as a degree of freedom other than time, frequency, and space, to support multiple input multiple output (MIMO) diversity and multiplexing [40]–[42]. The sub-THz channels have been observed to be more sparse than mmWave channels [18], [20]. Thus, the dual-polarized transmit and receive antenna arrays are necessary to deliver more signal energy and increase channel rank. NYUSIM 3.1 can satisfy such simulation requirements to generate different antenna polarization combinations for the same channel realization. More details regarding the polarization modeling can be found in Section 3.9.

Fixes and Updates

- NYUSIM 3.1 allows decimal inputs under the spatial consistency mode. Specifically, the inputs for the correlation distances of shadow fading and LOS/NLOS condition, update distance, moving distance, side length for hexagon track can be decimals. **Note that the correlation distance of shadow fading, moving distance, and side length for hexagon track need to be multiples of the update distance** so that the number of channel snapshots is an integer. Warnings related to the user-specified inputs were added.

- NYUSIM 3.1 was compiled with the latest Matlab 2021b to tackle potential system compatibility issues.

Acknowledgements

Revision History

1.

   Version 3.1 enables channel simulations with one polarization (co- or cross-polarization), two polarizations (co- and cross-polarizations), or four polarizations (namely, vertical-to-vertical (V-V), horizontal-to-horizontal (H-H), vertical-to-horizontal (V-H), and horizontal-to-vertical (H-V) polarizations) for every single channel realization. Note that multiple-polarization (i.e., "Co/X-Pol" and "All-Pol") options are currently only enabled for the drop-based simulations. Considering the potentially massive number of output figures and files under the spatial consistency mode, the options, "Co/X-Pol" and "All-Pol", will only generate co-polarized channels in the spatial consistency simulations.

   NYUSIM 3.1 allows users to input decimals for the correlation distances of shadow fading and LOS/NLOS condition, update distance, moving distance, side length for hexagon track. **Note that the correlation distance of shadow fading, moving distance, and side length for hexagon track need to be multiples of the update distance** so that the number of channel snapshots is an integer.

2. Ver 3.0: March 22, 2021

   Version 3.0 introduces an indoor statistical channel model following the mathematical framework of the existing NYUSIM outdoor channel modeling approach, which can simulate indoor channel impulse responses from 500 MHz to 150 GHz with 0 Hz to 800 MHz RF bandwidth. The indoor channel model was developed based on channel statistics extracted from channel measurements conducted in an office building at 28 GHz and 140 GHz [18].

3. Ver 2.01a: February 20, 2020

   Version 2.01a modifies the example code "getChannelMatrix.m" in the "Application Example Code" folder.

   The multipath delay stored in the data "DirPDPInfo" is in the unit of nanoseconds. A 10^{-9} was missing in Line 110 in the calculation of the channel matrix to have the unit as second (s). In NYUSIM 2.01a, the multipath delay is multiplied by 10^{-9} to have the correct unit as seconds.

4. Ver 2.01: November 1, 2019
   Version 2.01 provides two fixes in the function "getPowerInfo.m" and the function "getLocalCIR.m", respectively.

   (a) The list of input parameters for the function "getPowerInfo.m" is corrected to calculate large-scale path loss for the RMa scenario in the spatial consistency mode.

   (b) The unit inconsistency in the function "getLocalCIR.m" was fixed. Because the default unit of the user-specified antenna spacing in

NYUSIM is wavelength, the equation implemented in NYUSIM for calculating antenna array response vector is given by

$$\mathbf{a}(\phi) = [1, e^{j2\pi d_\lambda \cos(\phi)}, e^{j2\pi 2 d_\lambda \cos(\phi)}, ..., e^{j2\pi(N-1)d_\lambda \cos(\phi)}] \quad (1)$$

5. Ver 2.0: June 7th, 2019
   Version 2.0 provides three new channel modeling components, spatial consistency, human blockage, and O2I penetration loss.

   (a) Spatial consistency indicates continuous and realistic channel evolution along the user terminal (UT) trajectory in a local area. To realize spatial consistency, spatially correlated large-scale parameters such as shadow fading, line-of-sight (LOS)/non-LOS (NLOS) condition are generated, and time-variant small-scale parameters such as angles, power, delay, phase of each MPC are generated [43], [44]. Specifically, a geometry-based approach using multiple reflection surfaces is implemented to update spatially correlated and time-variant angular information [45].

   (b) A human blockage event usually causes a temporal shadowing loss, which may last about several hundreds of milliseconds. A typical blockage event can be divided into four stages, unshadowed, decay, shadowed, rising shown in Fig. 4 in [46], and a four-state Markov model corresponding to four stages was proposed to characterize blockage events [46], [47]. Such human blockage shadowing loss model is implemented in NYUSIM 2.0 for both omnidirectional and directional channels.

   (c) O2I penetration loss becomes more prominent at mmWave frequencies as shown in measurements and models [30], [48]–[50]. Many modern buildings are constructed by concrete and have infrared reflecting (IRR) glass, which induce a large penetration loss when a mmWave signal is transmitted from outdoor to indoor or vice versa [50]. A parabolic model for building penetration loss from [50], [51] is implemented in NYUSIM, which has either a low loss or a high loss form, depending on the type of building surface. The low loss model works for external building materials like standard glass and wood while the high loss model works for external building materials like IRR glass and concrete [50].

6. Ver 1.6.1: November 7th, 2018
   Version 1.6.1 provides two major improvements to NYUSIM, based on user feedback. The first improvement provides a complete MIMO channel representation. The second improvement fixes a crash when the RF bandwidth is set to be smaller than 800 MHz.

   (a) Fix 1: In Version 1.6 and earlier versions, NYUSIM only used the first TX antenna element with all RX antenna elements to generate the MIMO channel impulse responses, where NYUSIM should have used all TX antenna elements (N_{TX}) with all RX

antenna elements (N_{RX})when producing the MIMO channel impulse responses. In other words, earlier versions of NYUSIM only generated 1 x N_{RX} complex voltages for a particular multipath component. However, for proper MIMO channel modeling, N_{TX} x N_{RX} complex voltages of a particular multipath component are needed. The MIMO channel function is improved to generate a full MIMO impulse response (channel matrix) with respect to the number of TX antennas and the number of RX antennas. The parameter "CIR_MIMO" is expanded for all TX antenna elements for actual MIMO implementations and adjusted according to the user-specific RF bandwidth.

(b) Fix 2: In Version 1.6, a bug occurs when the RF bandwidth is set to be less than 800 MHz. The time resolution of the system becomes more coarse as the bandwidth is set by the user to be narrower than 800 MHz. Thus, fewer multipath components can be resolved at narrower bandwidth compared to the 800 MHz bandwidth. Thus, multipath components that arrive within a time bin are vectorially summed, and the function "getNewPowerSpectrum.m" in v 1.6.1 will correctly generate the band-adjusted power spectrum. AOA and AOD information retain 800 MHz bandwidth resolution, even if the user decreases the RF bandwidth.

7. Ver 1.6: December 15th, 2017

(a) In the base code package of NYUSIM, a new MATLAB script with the name "NYUSIM_MainCode" is added which acts as the main code of NYUSIM, such that users can obtain all the output figures and data files by setting the input parameters in the main code, and modify channel parameters and output files per users' own needs, without opening the GUI. The meaning of each parameter is annotated in "NYUSIM_MainCode".

(b) For the LOS environment, the first cluster of multipath components sometimes does not put the strongest multipath component as the first arriving component. While strong reflections could cause later arriving multipath components to be stronger than the first arriving multipath component, generally it has been found in the field that the first arriving multipath component will always be the strongest for LOS conditions. Therefore, Version 1.6 swaps (when necessary) the power level of the first arriving multipath component with the strongest multipath component in the first cluster of arriving components to ensure the first arriving multipath component is the strongest for LOS. This provides a realistic physical definition of the first arriving (shortest delay) multipath component in LOS situations. Additionally, for LOS environments, Version 1.5 and earlier did not keep track of the boresight angles at the TX and RX, thus the AoD and AoA of the LOS (strongest) multipath component may not be aligned on boresight, as shown in the upper plot of Fig. 1. In Version 1.6, the AoD and AoA of the LOS (strongest) multipath component
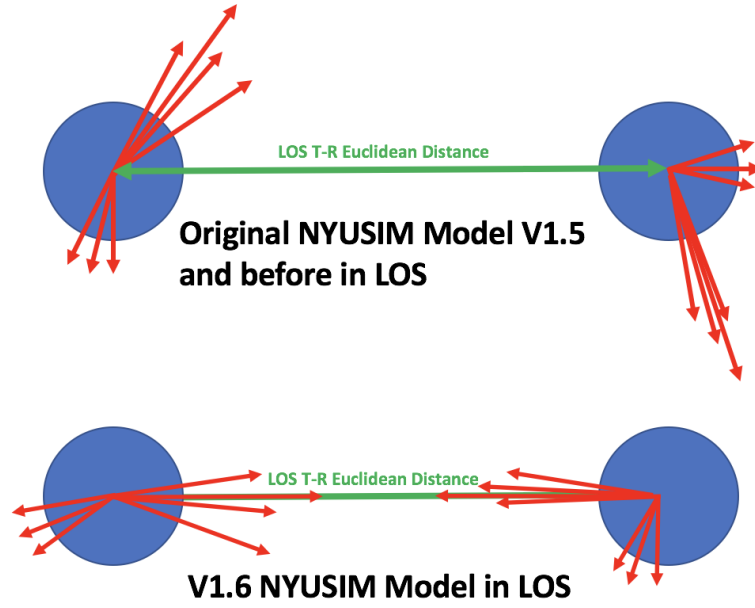
FIGURE 1: Illustration of how the AoD and AoA of the LOS (strongest) multipath component are aligned on boresight in LOS environments in NYUSIM Version 1.6.

are aligned on boresight for LOS environments, such that its azimuth AoD and azimuth AoA differ by 180°, and its elevation AoA is the additive inverse of its elevation AoD, to match the physics of on-boresight communication. The AoDs and AoAs of all the other multipath components are shifted accordingly in relation to the LOS multipath component, as illustrated in the lower plot of Fig. 1. The "NYUSIM_MainCode" is documented to show this, and this change was requested by industry users who are performing 5G system simulations. No such changes are made to NLOS environments.

(c) The PLE in the UMa NLOS scenario is changed from 3.2 to 2.9 to make it more accurate according to the data from extensive measurements presented in [5]. This change is made inside the GUI code that is inaccessible to users, but is also reflected in "NYUSIM_MainCode" mentioned above that is available to users, where the PLE is represented by the variable n as annotated in the code itself.

(d) A new input parameter named "Distance Range Option" is added to the GUI in Version 1.6, which has two options: standard (10-500 m) (used in Version 1.5 and earlier versions) and extended (10-10,000 m). The NYUSIM channel model predicts accurate results for standard distance range (10-500 m). The extended distance range beyond 500 m should be set with caution, since NYUSIM is developed based on field measurements within 500 m, as explained in Section 3.1.1 of this user manual. The extended distance range is added based on users' requests. For the distance range no larger than 500 m, the dynamic range (i.e., largest possible path loss) is set to 190 dB in NYUSIM based

on field measurement results [1], [2], [5], while for the distance range beyond 500 m, the dynamic range is set to 220 dB.

(e) Another new input parameter named "Base Station Height" is added to the GUI and output data files for the RMa scenario in Version 1.6, which is utilized for calculating path loss in the RMa scenario. This variable name is annotated in the "NYUSIM_MainCode" itself.

(f) Both LOS and NLOS path loss models in the RMa scenario are modified to incorporate the dependence on the base station height based on Eqs. (21) and (22) in [12].

(g) For the RMa scenario, the number of time clusters and the number of spatial lobes are both set to one, and the maximum number of multipath components is set to two, based on our RMa mmWave field measurements which show sparsity for rural scenarios [12].

(h) In the title or text in output figures, the scenario type (i.e., UMi, UMa, or RMa) is added in addition to the environment type (i.e., LOS or NLOS).

(i) In the output AoD and AoA spectra, the multipath component with the minimum received power is also shown as a line (it was shown as a dot in the center in previous versions due to a different plotting setting). Furthermore, the view point of the AoD and AoA spectra is changed in Version 1.6 to be along the z-axis, and the legend position is adjusted to avoid overlapping with the spectrum. For the path loss scatter plot, the x-axis is extended to 10 km even if the standard distance range is used.

(j) The Ricean K-factor is now calculated for every PDP, and is an output parameter in the data file for each simulation run, where the K-factor refers to the ratio of the power of the strongest multipath component in the PDP to the sum of powers of all the other multipath components in the PDP [4]. For Version 1.6, in LOS environments, this will be the ratio of the power of the first arriving multipath component to the sum of powers of all later arriving multipath components. This was suggested by industry users.

(k) New warning messages are added that will occur when input parameters are not reasonable or exceed their predefined ranges shown on the GUI, as explained in detail in Section 2 of this user manual.

(l) More references, such as [8] and [11], are added in the user manual regarding the comparison between the 3GPP [26] and NYUSIM channel models, and the significant impact of the choice of channel models on wireless system performance evaluation.

8. Ver 1.5: April 5th, 2017

(a) A more detailed overview about the mmWave measurements on which NYUSIM has been built, the related publications, and key differences/advantages of the NYUSIM channel model as compared to the 3GPP TR 38.900 Release 14 channel model are added in NYUSIM Overview on Page ii of this user manual.

(b) The name of the output figure "Omni. PDP with Directional Antenna Gains" is changed to "Directional PDP with Strongest Power" to make it more accurate. Textual information on channel parameter values, such as frequency, environment, distance, root-mean-square (RMS) delay spread, received power, path loss, is added to the output figure "Directional PDP with Strongest Power", in which the path loss equals the transmit power subtracted by the transmitter (TX) and receiver (RX) antenna gains and the received power.

(c) One additional output figure entitled "PathLossPlot" is added if the user performs N ($N \geq 1$) continuous simulation runs with the same input parameters but with varying distances. The figure "PathLossPlot" illustrates a scatter plot of omnidirectional path loss and directional path loss values for over the entire distance range generated from the N ($N \geq 1$) continuous simulation runs, along with the fitted path loss exponent (PLE) and shadow fading standard deviation. Detailed information about the figure "PathLossPlot" is provided in Section 2.2.1 of this user manual.

(d) Four additional output data files, namely, "OmniPDPInfo.txt", "DirPDPInfo.txt", "OmniPDPInfo.mat", and "DirPDPInfo.mat", are added after N ($N \geq 1$) continuous simulation runs with the same input parameters are performed by the user. "Omni" denotes omnidirectional, while "Dir" stands for directional. Detailed descriptions about these four files were added in Section 2.2.2 of this user manual.

(e) The output files "BasicParameters.txt" and "BasicParameters.mat" are generated only once for all N ($N \geq 1$) continuous simulation runs with the same input parameters, instead of being generated for each individual simulation run, since the parameters contained in these two files remain the same for N ($N \geq 1$) continuous simulation runs.

(f) Two parameter values in each of the two output files "BasicParameters.txt" and "BasicParameters.mat", i.e., omnidirectional received power and omnidirectional path loss, are removed since they are now included in the new output files "OmniPDPInfo.txt" and "OmniPDPInfo.mat".

(g) Detailed explanation on how the directional PDP with strongest power is generated is added in Section 2.2.1 of this user manual.

(h) Examples of the six output figures from NYUSIM are added in Section 2.2.1 of this user manual.

(i) Error warnings are added for the cases where the input antenna HPBW by the user exceeds the pre-defined range on the GUI. Explanations are detailed in Section 2.1.5 of this user manual.

(j) Figs. 3.1 and 3.2 in Section 3.1 are modified where the humidity is changed from 98% to 80%, and temperature is changed from -20°C to 20°C, to reflect more realistic atmospheric conditions.

(k) A new chapter (Chapter 4) is created to present a variety of applications of NYUSIM. The original application section in Chapter 2 is also moved to Chapter 4.

(l) The MATLAB code "getChannelMatrix" and the associated explanation in the NYUSIM application code package are updated according to the new output data files.

(m) The root folder for users to select from to save output files is changed from the C drive to the folder "Users".

(n) A new version of the NYUSIM software is created for the Mac operating system, with all of the above updates implemented. Installation instructions are provided in Section 1.

9. Ver 1.4: October 31st, 2016

(a) More operation steps were added on the top part of the simulator GUI to better instruct users.

(b) Detailed explanations of the half-power beamwidth (HPBW) and gain of the antenna array, and examples of how to create an antenna pattern given the HPBW and gain, were added in Section 2.1.1 of this user manual.

(c) The .mat format of the output data files was provided in the simulator, in addition to the existing .txt files. Descriptions of the newly added files were provided in Section 2.2.2 of this user manual. A new option was added on the GUI that allows users to select the output file type (text file, MAT file, or both).

(d) A new set of output data file named "BasicParameters" was added with both .txt and .mat formats available, which contains all the input parameter values as shown on the GUI when running the simulation and some relevant output parameters, as detailed in Section 2.2.2.

(e) An example of the applications of the output data files was demonstrated in Section 2.2.3, namely, calculating the condition number and rank of multiple-input multiple-output (MIMO) orthogonal frequency division multiplexing (OFDM) channel matrices, and the corresponding MATLAB script was provided in the package named "Application Example Code" available on the NYUSIM downloading website.

10. Ver 1.3: August 19th, 2016

(a) Descriptions of the numbers of matrix columns and rows in the output .txt files containing the complex channel coefficients (H), phases (HPhases), and powers (HPowers) were corrected in Section 2.2.2 of this user manual.

(b) The rural macrocell (RMa) path loss parameters in the close-in reference distance (CI) path loss model have been slightly changed in the simulator and Section 3.1 of this user manual, based on the new mmWave rural path loss study in [9].

(c) The new frequency range of the simulator has been tested and is usable from 500 MHz to 100 GHz.

11. Ver 1.2: August 2nd, 2016

    (a) Four new input parameters, i.e., Polarization, Foliage Loss, Distance Within Foliage, and Foliage Attenuation, were added to the input parameters on the NYUSIM GUI, the corresponding code was added to the base code, and the corresponding descriptions of the four new input parameters were added in Section 2 of the user manual.

    (b) The NYU CI RMa path loss model was added to the simulator and user manual, and the option "RMa" was added to the "Scenario" parameter on the GUI.

    (c) More background regarding the creation and application of NYUSIM was added to the section *NYUSIM Overview*, and two related citations were added to the reference list.

    (d) A 32-bit version of NYUSIM was generated, in addition to the existing 64-bit version.

12. Ver 1.1: July 16th, 2016

    (a) Four new input parameters, i.e., Barometric Pressure, Humidity, Temperature, and Rain Rate, were added to the input parameters on the NYUSIM GUI, the corresponding code was added to the base code, and the corresponding descriptions of the four new input parameters were added in Section 2 of the user manual.

Contents

List of Figures

1. Installation of Software Package

1.1 System Requirements

1.1.1 Operating System

Minimum requirement: Windows 7 (or higher), or Macintosh operating systems (Mac OS X)

The Windows version of NYUSIM runs on Windows operating systems only, and the Mac version of NYUSIM runs on Mac OS X only.

1.2 Installation

The required program files of the NYUSIM software suite are provided by NYU WIRELESS via Internet download at http://wireless.engineering.nyu.edu/5g-millimeter-wave-channel-modeling-software/.

1.2.1 Windows Operating System

The Windows version of NYUSIM is delivered as an installer package for Windows operating systems. All components required to run the applications are automatically installed after double clicking on the setup executable (NYUSIM_V3_WIN.exe file).

1.2.2 Mac OS X

The Mac version of NYUSIM is delivered as an installer package for Mac OS X. All components required to run the applications are automatically installed after double clicking on the setup executable (NYUSIM_V3_MAC.app file).

One potential problem is that the recent Mac system (High Sierra 10.13 and later) introduced a new security feature called gatekeeper path randomization. This security feature makes it difficult to run applications installed outside of the Mac App Store. If a popup window shows an error during the installation as shown in Fig. 1.1, please execute the following command in the terminal command line:

    sudo xattr -d com.apple.quarantine NYUSIM_V3_MAC.app
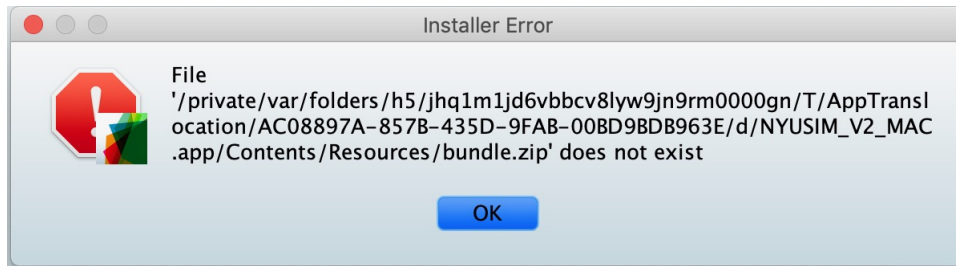
FIGURE 1.1: Possible installation error for Mac system.

For additional support, please contact nyusim@nyuwireless.com.

2. Basics

2.1 Graphical User Interface and Simulator Basics

The screenshot in Fig. 2.1 shows the GUI of NYUSIM 3.0. The simulator performs Monte Carlo simulations, generating samples of CIRs at specific T-R separation distances. Note that the range of T-R separation is provided by the user, and the actual T-R separation distance is uniformly selected from the user-specified distance range. Two running modes, drop-based mode and spatial consistency mode are made available from NYUSIM 2.0. When the spatial consistency button is "on", NYUSIM runs spatial consistency procedure and generates successive and correlated CIRs along the UT trajectory. When the spatial consistency button is "off", NYUSIM runs the drop-based model which is the same as previous versions of NYUSIM and generates independent CIRs for different distances. Note that human blockage module works for both drop-based mode and spatial consistency mode. While earlier versions of NYUSIM provided outdoor channel models as well as outdoor-to-indoor penetration, NYUSIM 3.0 introduces the indoor office scenario (only in the drop-based mode). The indoor scenario can be selected under the "Scenario" drop-down list. The spatial consistency feature for indoor scenario will be implemented in future release.
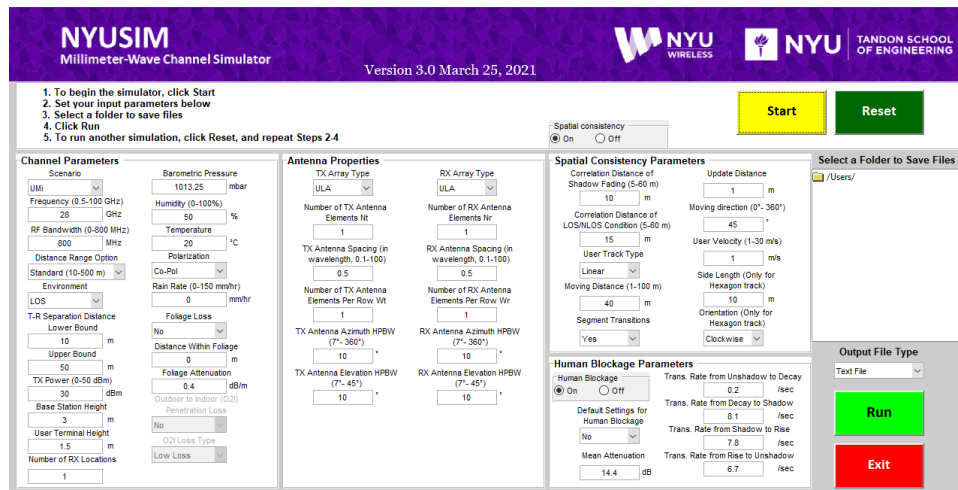
FIGURE 2.1: Graphical User Interface (GUI) of NYUSIM 3.0 with four panels: channel parameters, antenna properties, spatial consistency parameters, human blockage parameters.

2.1.1 Input Parameters

There are 49 input parameters to the channel simulator, which are grouped into four main categories: *Channel Parameters*, *Antenna Properties*, *Spatial Consistency Parameters*, and *Human Blockage Parameters*, as shown on the GUI in Fig. 2.1. Note that two input parameters for O2I penetration loss are put into the panel *Channel Parameters*.

The panel *Channel Parameters* contains 19 fundamental input parameters about the propagation channel, as listed and explained below:

1. Scenario: a selectable parameter denoting the scenario. Four channel scenario options, urban microcell ("UMi"), urban macrocell ("UMa"), rural macrocell ("RMa"), and indoor hotspot ("InH") are applicable. The default scenario option is "UMi". Selecting the "InH" option will change the allowable carrier frequency range from 0.5-100 GHz (for outdoor scenarios) to 0.5-150 GHz, distance range option from "Standard (10-500m)" to "Indoor (5-50 m), the upper limit of base station height from 150 m (for outdoor scenarios) to 3 m. Selecting the "InH" option will also disable following options: "Rain Rate", "Foliage Loss", "Distance Within Foliage", "Foliage Attenuation", "Outdoor to Indoor (O2I) Penetration Loss", "O2I Loss Type", and spatial consistency mode.

2. Frequency (GHz): an editable parameter denoting the carrier frequency in GHz. The default value is 28 (GHz), and it can be varied from 0.5 to 100 (GHz) with at most one decimal place for UMi, UMa, and RMa scenarios. When "InH" is selected, the allowable carrier frequency range will range from 0.5 to 150 (GHz).

3. RF Bandwidth (MHz): an editable parameter denoting the RF bandwidth of the transmitted signal in MHz. The default value is 800 MHz, and it can be varied from 0 to 800 MHz. As the simulator was developed from real-world measurements obtained with an RF bandwidth of 800 MHz, it can only scale down from 800 MHz.

4. Distance Range Option: a selectable parameter denoting the distance range. Three options, "Standard (10-500 m)", "Extended (10-10,000 m)", and "Indoor (5-50 m)" are applicable. The default setting is "Standard (10-500 m)". For distances less than 500 m, the dynamic range (i.e., largest possible path loss) is set to 190 dB in NYUSIM based on field measurement results [1], [2], [5], while for the distance range beyond 500 m, the dynamic range is set to 220 dB. When "InH" is selected, the "Distance Range Option" is fixed to be "Indoor (5-50 m)" option.

5. Environment: a selectable parameter denoting the environment, either line-of-sight (LOS) or non-line-of-sight (NLOS). The default setting is LOS.

6. Lower Bound of T-R Separation Distance (m): an editable parameter denoting the smallest distance between the transmitter (TX) and receiver (RX) in meters with at most one decimal place. The default value is 10 m, and it can be varied from 10 m to 500 m for the standard range (verified by extensive measurements by NYU), 10 m to 10 km for the extended range, and 5 m to 50 m for the indoor range but no more than the upper bound of the T-R separation distance.

7. Upper Bound of T-R Separation Distance (m): an editable parameter denoting the largest distance between the TX and RX in meters with at most one decimal place. The default value is 500 m, and it can be varied from 10 m to 500 m for the standard range (verified by extensive measurements by NYU), and 10 m to 10 km for the extended range, and 5 m to 50 m for the indoor range, but no less than the lower bound of the T-R separation distance.

8. TX Power (dBm): an editable parameter denoting the transmit power in dBm. The default value is 30 (dBm), and can be set to any value ranging from 0 to 50 (dBm).

9. Base Station Height (m): an editable parameter denoting the base station height in meters. The default value is 35 (m) [26], and can be set to any value ranging from 10 to 150 (m) [12]. This base station height is only applicable to RMa modeling and is ignored for UMi and UMa scenarios. The maximum height of stations is 3 m for the InH scenario.

10. User Terminal Height (m): an editable parameter denoting the UT height in meters. The default value is 1.5 (m) [26], and can be set to any value ranging from 1 to 10 (m) above the ground [12].

11. Barometric Pressure: an editable parameter denoting the barometric pressure in mbar used in evaluating propagation path loss induced by dry air. The default and typical value is 1013.25 mbar (millibar) (i.e., nominal for sea level), and may range from 10^{-5} to 1013.25 (mbar) [52].

12. Humidity: an editable parameter denoting the relative humidity in percentage used in evaluating propagation path loss induced by vapor. The default value is 50 (%), and can be set to any number between 0 and 100 (%).

13. Temperature: an editable parameter denoting the temperature in degrees Celsius used in evaluating propagation path loss induced by haze/fog. The default and typical value is 20 (°C), and may range from -100 to 50 (°C) [52].

14. Rain Rate: an editable parameter denoting the rain rate in mm/hr used in evaluating additional propagation path loss induced by rain. The default value is 0 (mm/hr), and the typical range is 0 to 150 (mm/hr) [1]. This option is disabled for the InH scenario.

15. Polarization: a selectable parameter denoting the polarization relation between the TX and RX antennas or antenna arrays. The default setting is Co-Pol (co-polarization), and can be changed to X-Pol (cross-polarization), Co/X-Pol (co- and cross-polarization), and all-Pol (V-V, H-H, V-H, and H-V polarization). The cross-polarization discrimination (XPD) can vary from 5 dB to 27 dB [53]–[55], depending on the frequency and environment. In this simulator, for Co-Pol, no extra loss will be added to the path loss, while an extra scenario- and frequency-dependent loss will be added to the path loss for X-Pol due to polarization mismatch based on the measurement results in [55]. In addition, a zero-mean Gaussian random variable will be added to generate the H-H (H-V) power from the V-V (V-H) power. For more detailed background, please refer to Section 3.9.

16. Foliage Loss: a selectable parameter indicating whether or not foliage loss will be considered in the simulation. The default setting is "No" (which implies foliage loss will not be considered), and can be changed to "Yes" (which means foliage loss will be considered). This option is disabled for the InH scenario.

17. Distance Within Foliage: an editable parameter representing the distance in meters that the transmitted signal travels within foliage. The default value is 0, and can be set to any non-negative number no larger than the lower bound of the T-R separation distance. This option is disabled for the InH scenario.

18. Foliage Attenuation: an editable parameter denoting the propagation loss induced by foliage in dB/m. The default value is 0.4 (dB/m) based on the measurement results in [55], and can be set to any value between 0 and 10 (dB/m). For more detailed background, please refer to [55]. This option is disabled for the InH scenario.

19. Number of RX Locations: an editable parameter denoting the number of RX locations. It can be any positive integer number. The default value is 1, and can be set to any integer from 1 to 10,000.

20. Outdoor to Indoor (O2I) Penetration Loss: a selectable parameter denoting that a UT is in an indoor or outdoor scenario. Two options, "Yes" and "No", are provided. The default value is "No". If "Yes" is selected, additional building penetration loss will be added to the total received power before small-scale parameters are generated [51], [56]. If "No" is selected, penetration loss is not considered. This option is disabled for the InH scenario.

21. O2I Loss Type: a selectable parameter denoting the O2I loss type. Two option, "Low Loss" and "High Loss", are provided. The "Low Loss" model corresponds to low loss building materials such as standard glass and wood [50], [51]. The "High Loss" corresponds to high loss building materials such as infrared reflecting (IRR) glass and concrete [50], [51]. This option is disabled for the InH scenario.

The panel *Antenna Properties* contains 12 input parameters related to the TX and RX antenna arrays, as listed and explained below:

1. TX Array Type: a selectable parameter denoting the TX antenna array type. The default setting is ULA (uniform linear array), and can be changed to URA (uniform rectangular array).

2. RX Array Type: a selectable parameter denoting the RX antenna array type. The default setting is ULA, and can be changed to URA.

3. Number of TX Antenna Elements N_t: an editable parameter denoting the total number of TX antenna elements in the array. The default value is 1, and can be set to any integer from 1 to 128.

4. Number of RX Antenna Elements N_r: an editable parameter denoting the total number of RX antenna elements in the array. The default value is 1, and can be set to any integer from 1 to 64.

5. TX Antenna Spacing (in wavelength): an editable parameter denoting the spacing between adjacent TX antennas in the array in terms of the carrier wavelength. The default value is 0.5, and can be set to any positive number with up to one decimal place from 0.1 to 100.

6. RX Antenna Spacing (in wavelength): an editable parameter denoting the spacing between adjacent RX antennas in the array in terms of the carrier wavelength. The default value is 0.5, and can be set to any positive number with up to one decimal place from 0.1 to 100.

7. Number of TX Antenna Elements Per Row W_t: an editable parameter denoting the number of TX antennas in one dimension when the TX Array Type is ULA or URA, which should divide the number of TX antenna elements. The default value is 1.

8. Number of RX Antenna Elements Per Row W_r: an editable parameter denoting the number of RX antennas in one dimension when the RX Array Type is ULA or URA, which should divide the number of RX antenna elements. The default value is 1.

9. TX Antenna Azimuth HPBW (degrees): an editable parameter denoting the azimuth half-power-beamwidth (HPBW) of the TX antenna (array) in degrees. The default value is $10°$, and can be set to any value from $7°$ to $360°$ (since the smallest azimuth HPBW of the antennas used in the measurements for the simulator was $7°$).

10. TX Antenna Elevation HPBW (degrees): an editable parameter denoting the elevation HPBW of the TX antenna (array) in degrees. The default value is $10°$, and can be set to any value from $7°$ to $45°$ (since the smallest elevation HPBW of the antennas used in the measurements for the simulator was $7°$).

11. RX Antenna Azimuth HPBW (degrees): an editable parameter denoting the azimuth HPBW of the RX antenna (array) in degrees. The default value is $10°$, and can be set to any value from $7°$ to $360°$.

12. RX Antenna Elevation HPBW (degrees): an editable parameter denoting the elevation HPBW of the RX antenna (array) in degrees. The default value is $10°$, and can be set to any value from $7°$ to $45°$.

It is worth noting that the HPBW in the input parameters is for the entire antenna array, instead of for each antenna element, when the number of antenna elements is more than one at the TX and/or RX. Conventionally, the HPBW of an antenna array is a function of the number of antenna elements and the antenna spacing, but in this simulator these three parameters (i.e., the HPBW, number of antenna elements, and antenna spacing) can be independently specified by the user, since there may be a wide range of beamforming approaches (e.g., digital, analog, hybrid), in all of which different individual antenna element types (e.g., patch antennas, vertical antennas, horns) may be used. To make the simulator as general as possible, we specify the number of individual antenna elements (without specifying the gain or combining losses thereof) and the total array HPBW. Note that the antenna pattern and implementation details are only very loosely defined to specify the gain in the particular pointing (maximum gain) direction.

Since some antenna elements may have more gain or loss depending on the specific array type (e.g., ULA); that is, someone may choose to fabricate their individual array with more individual antenna element gain than another person will, and losses vary with fabrication process (e.g., on chip antenna elements have more loss when a lens is not used than if a lens is used). Instead of dealing with the myriad antenna fabrication and connection details needed to make an array — there are numerous variables — we simply allow the total HPBW and the number of elements to be specified, without specifying the individual antenna element gain. For example, assuming there are four elements in an antenna array, where each element has 6 dB gain because they are patch or Yagi/directional or horn antennas for each element, then this array can have the same overall HPBW as a 16-element array with unity gain dipole or vertical elements.

Without specifying the specific antenna elements and their interconnected characteristics, only the HPBW is specified while the beam pattern is left undefined. Consequently, one has the freedom to implement an antenna pattern of their choice for system simulations, which may include interference from signals outside of the main gain direction. Here are some heuristic approaches of constructing one's own antenna pattern based on the specified HPBW, where the antenna gains in the following equations are all relative to an isotropic antenna.

- The antenna pattern employed in [3] has the following form:

$$G(\theta, \phi) = max(G_0 e^{-\alpha\theta^2 - \beta\phi^2}, \frac{G_0}{100})$$
$$\alpha = \frac{4ln(2)}{\theta_{3dB}^2}, \ \beta = \frac{4ln(2)}{\phi_{3dB}^2}, \ G_0 = \frac{41253\eta}{\theta_{3dB}\phi_{3dB}}$$

(2.1)

where $(\theta, \ \phi)$ denote the azimuth and elevation angle offsets from the boresight direction in degrees, G_0 is the maximum directive gain (boresight gain) in linear units, $(\theta_{3dB}, \ \phi_{3dB})$ represent the azimuth and elevation HPBWs in degrees, $(\alpha, \ \beta)$ are parameters that depend on the HPBW values, and $\eta = 0.7$ is a typical average antenna efficiency.

- The antenna pattern used in [6] has the expression below:

$$f(\phi, \theta) = G \left[\text{sinc}^2 \left(a \cdot \sin(\phi) \right) \cos^2(\phi) \right] \\ \cdot \left[\text{sinc}^2 \left(b \cdot \sin(\theta) \right) \cos^2(\theta) \right]$$

(2.2)

where ϕ and θ represent the azimuth and elevation angles with respect to the antenna boresight, respectively, $f(\phi, \theta)$ denotes the radiation power density at the azimuth angle ϕ and elevation angle θ, G is the antenna boresight gain, and a and b are functions of the azimuth (AZ) and elevation (EL) HPBWs of the horn antenna, respectively, i.e.,

$$\text{sinc}^2 \left(a \cdot \sin(\frac{\text{HPBW}_{\text{AZ}}}{2}) \right) \cos^2 \left(\frac{\text{HPBW}_{\text{AZ}}}{2} \right) = \frac{1}{2}$$

(2.3)

$$\text{sinc}^2 \left(b \cdot \sin(\frac{\text{HPBW}_{\text{EL}}}{2}) \right) \cos^2 \left(\frac{\text{HPBW}_{\text{EL}}}{2} \right) = \frac{1}{2}$$

(2.4)

- The radiation pattern of a sectored cell site antenna was employed in [57], where the azimuthal radiation pattern is modeled as a cardioid given by [57]

$$r(\theta) = \alpha[1 + \sin(\theta + \frac{\pi}{2})]$$

(2.5)

where r is the gain of the antenna at azimuth angle θ from its maximum lobe and is a scaling factor. The elevation radiation pattern is an ellipse with the base station at a focus point [57]:

$$\frac{x^2}{a^2} + \frac{y^2}{b^2} = 1$$

(2.6)

9

- A sectored antenna pattern model was introduced in [58], where constant directivity gains are assumed for the main lobe and the side lobe.

The panel *Spatial Consistency* contains 10 input parameters related to the spatial consistency implementation, as listed and explained below: (Spatial consistency mode will be disabled for indoor channel simulation)

1. Correlation Distance of Shadow Fading (5-60 m): an editable parameter denoting the correlation distance of shadow fading. The default value is 10 m. Correlation distance of shadow fading, also known as "local area" determines the length of a channel segment. Correlation distance is the distance beyond which the auto-correlation value of a large-scale parameter (LSP) falls below 0.5 [14]. Within the correlation distance, LSPs are considered spatially correlated during the UT movement. If a UT moves beyond the correlation distance, the LSPs are considered independent and are randomly generated again based on the pre-defined probabilistic distributions [15]. Specifically, a new channel will be initialized and new CIRs will be independently regenerated when a UT moves beyond the correlation distance of shadow fading.

2. Correlation Distance of LOS/NLOS Condition (5-60 m): an editable parameter denoting the correlation distance of LOS/NLOS condition. Correlation distance of LOS/NLOS condition is used to generate spatially correlated LOS/NLOS values, which means a UT that moves in a local area should always experience same visibility condition (LOS or NLOS) [14], [15]. Specifically, the visibility condition does not change within a channel segment, but may change by reading the spatially correlated map based on the UT location when the next segment starts.

3. UT Track Type: a selectable parameter denoting the UT track type. Two options, "Linear" and "Hexagon" are provided to the user. The default option is "Linear" [16].

4. Track Distance (1-100 m): an editable parameter denoting the track length of a UT trajectory. Note that the input track distance for the "Hexagon" track should not be larger than the perimeter of the hexagon. Realistic CIR generation cannot be guaranteed out of the limit. The track distance is divided into multiple channel segments based on the correlation distance of shadow fading.

5. Update Distance (<1 m): an editable parameter denoting the distance interval between two channel snapshots. The default value is 1 m. Decreasing the update distance causes more CIRs to be generated by NYUSIM with the separation between each CIR generated by NYUSIM equal to the update distance. Note that the update distance should not be set too small because it is computationally expensive. Update distances of 0.1, 0.5, and 1 m are suggested.

6. Moving direction (0°-360°): an editable parameter denoting the initial UT moving direction. The default value is $45°$. Both "Linear" and "Hexagon" track require an initial moving direction. For a linear track, the moving direction does not change during the simulation.

For a hexagon track, the moving direction changes based on the track distance and side length of the hexagon.

7. UT Velocity (1 - 30 m/s): an editable parameter denoting the UT velocity. The default value is 1 m/s, close to the typical human walking speed. The UT velocity in concert with the update distance determine the update time which is the time interval between two consecutive CIRs.

8. Side Length: an editable parameter denoting the side length of the hexagon track. This parameter only works for the "Hexagon" track. The default value is 10 m.

9. Orientation: a selectable parameter denoting the orientation of the hexagon track. This parameter only works for the "Hexagon" track. Two options, "Clockwise" and "Counter", are provided.

10. Segment Transitions: a selectable parameter denoting whether the smooth transitions between two segments. Two options, "Yes" and "No" are provided. With "Yes" selected a post-processing is done to "connect" generated channel segments via cluster birth and death. "No" generates independent channel segments, with channel snapshots are spatially correlated in each channel segment [16].

The panel *Human Blockage* contains 6 input parameters related to the human blockage shadowing loss due to a person near the mobile phone (UT), as listed and explained below. Human blockage can be turned "on" or "off". As explained in Section 3, the length of a Markov trace is 20 s long, and the time resolution is 1 ms.

1. Default Settings for Human Blockage: a selectable parameter. Two options, "Yes" and "No", are provided. If the user chooses "Yes", the transition rates and average mean attenuation are implemented based on a linear fit to the data given in [59], and changes to fit the work in [59] as the RX antenna azimuth HPBW changes. If the user chooses "No", the transition rates and mean attenuation are free to edit for user-specified preferences, in case other Markov model parameters are preferred or discovered in the future [47], [59].

2. Mean Attenuation: an editable parameter denoting the mean attenuation of blockage events (SE_{mean}). The default value is 14.4 dB.

3. Trans. Rate from Unshadow to Decay (1/s): an editable parameter denoting the transition rate from unshadowed state to decay state. The default value is 0.20 when the RX antenna azimuth HPBW is $10°$.

4. Trans. Rate from Decay to Shadow (1/s): an editable parameter denoting the transition rate from decay state to shadowed state. The default value is 8.08 when the RX antenna azimuth HPBW is $10°$.

5. Trans. Rate from Shadow to Rise (1/s): an editable parameter denoting the transition rate from shadowed state to rise state. The default value is 7.85 when the RX antenna azimuth HPBW is $10°$.

6. Trans. Rate from Rise to Unshadow (1/s): an editable parameter denoting the transition rate from rise state to unshadowed state. The default value is 6.70 when the RX antenna azimuth HPBW is 10°.

2.1.2 Output Folder Selection

To the right of the above four category panels on the GUI (see Fig. 2.1), there is an option named "Select a Folder to Save Files". This option allows users to select a folder to save the output files (e.g., figures, data files) from the simulator. The default path is the disk that contains the current running folder. Users can select a folder inside the default path by clicking on the desired paths/folders.

2.1.3 Output File Type Selection

To the right of the folder selection option on the GUI, there is an option named "Output File Type". This option allows users to select a file type for the output data files from the simulator. The default type is *Text File*, and can be switched to *MAT File*, and *Both Text and MAT File*.

2.1.4 Operation of the GUI

Five basic steps, as shown on the top left panel on the GUI, need to be executed to run the channel simulator:

1. To begin (reset) the simulator, click Start (Reset)

2. Set your input parameters below

3. Select a folder to save files

4. Click Run

5. To run another simulation, click Reset, and repeat Steps 2-4

The meanings of these steps are detailed as follows.

When opening the GUI for the first time, users shall click on the yellow button "Start" to initiate the simulator and enable the input of the GUI. Next, users can set and/or select the input parameters according to their own needs; the simulator will execute the default values for each parameter if there is no input from the user. Then, users shall select a folder to save all the output files by clicking on the desired paths/folders under the option "Select a Folder to Save Files". Finally, users shall click on the light green button "Run" to run the simulations.

While the simulator is running, a progress bar will pop up at the bottom left of the GUI, which informs users of the progress of the simulations. After the simulation is complete, the progress bar will disappear automatically, and the five figures generated from the first simulation run will pop up on the screen.

To initiate another set of simulation runs (e.g., with different input parameter values), users shall click on the dark green button "Reset", after which

all the input parameters from the previous simulation run will be set as the default input values.

The simulator can be closed at any time by clicking the red button "Exit" on the bottom right of the GUI.

If the input parameter exceeds the predefined range shown on the NYUSIM GUI or is not reasonable/logical, an error message will pop up to let the user either reset the parameter on GUI or modify the NYUSIM source code without using the GUI to meet users' own needs. For example, if the input number of TX antenna elements per row W_t is larger than the input number of TX antenna elements N_t, a corresponding error message will pop up. Users shall click "OK" on the error bar, then click the dark green button "Reset" on the GUI to reset the input parameter, and the following steps are identical to those described above.

2.2   Output Files

Since Version 2.0, NYUSIM provides two running simulation modes, drop-based mode and spatial consistency mode, which depends on that the spatial consistency feature is "on" or "off". The default output figures and files in the drop-based mode are the same as the figures and files output from older version of NYUSIM (e.g. Version 1.6 and earlier). The output figures and files for the drop-based mode and the spatial consistency mode are introduced separately as follows.

2.2.1   Output Figures

— Drop-based Mode

The drop-based mode assumes random and independent channel simulations for any T-R separation distance. An ensemble of random, independent channel responses is easily generated in NYUSIM for a fixed T-R separation distance or a range of T-R separation distances using the drop-based mode. A simulation run may produce hundreds or thousands of channel impulse responses for different T-R separation distances.

For each simulation run, five figures will be generated and stored that are based on the particular results of the simulation that is being run, and an additional figure of path loss scatter plot will be generated and stored after N ($N \geq 1$) continuous simulation runs with the same input parameters are complete. Note that the T-R separation distance is not an input parameter, but, instead, the lower bound and upper bound of the T-R separation distance are input parameters, such that the actual T-R separation distance will vary automatically among different simulation runs. Regardless of the number of simulation runs (RX locations), the five figures generated from the first simulation run, as well as the last figure generated for N ($N \geq 1$) continuous simulation runs with the same input parameters, will pop up on the screen for visual purposes. The contents of those figures are as follows:

- Three-dimensional (3D) AoD power spectrum, as illustrated in Fig. 2.2.

- 3D AoA power spectrum, as shown in Fig. 2.3.

- A sample omnidirectional PDP, as displayed in Fig. 2.4. Some fundamental information such as the frequency, environment, T-R separation distance, RMS delay spread, omnidirectional received power, omnidirectional path loss, and PLE [1], [2] is displayed on the PDP plot. The lower limit of the y-axis denotes the noise threshold (i.e., the minimum received power of each resolvable multipath component) determined by the transmit power, dynamic range of our measurement system (180 dB), and a 10 dB SNR, i.e., the threshold equals the transmit power in logarithmic scale minus 170 dB.

- A sample directional PDP with strongest power, where directional antenna gain patterns are implemented at the TX and/or RX, as depicted in Fig. 2.5. This figure is generated by allowing users to implement arbitrary directional antenna patterns (gains and HPBWs) in an omnidirectional PDP, since directional antennas/antenna arrays will be utilized at the TX and/or the RX in a realistic mmWave communication system to provide gains to compensate for the higher free space path loss at mmWave frequencies. To obtain the directional PDP with the strongest received power, NYUSIM searches for the best pointing angle out of all possible pointing angles, using the specified antenna details (i.e., azimuth and elevation HPBWs of TX and RX antennas) after first generating the omnidirectional PDP, such that the pointing angle of the TX and RX are found that gives the strongest received power. The TX/RX antenna gain pattern is calculated by NYUSIM using Eq. (2.1) in this user manual by employing the azimuth and elevation HPBWs of TX and RX antennas specified by the user on the GUI. This feature makes the channel simulator more valuable as it shows how a PDP will look like in a channel with directional antennas/antenna arrays used at the communication link end. On the directional PDP figure, relevant channel and antenna parameters, such as the frequency, environment, T-R separation distance, directional RMS delay spread, directional received power, directional path loss, directional PLE, and TX and RX antenna HPBWs and gains, are also displayed, where the directional path loss equals the transmit power plus TX and RX antenna gains, minus the directional received power [2], [6], [7].

- A series of PDPs over each receive antenna element obtained using Eq. (3) of [60], as shown in Fig. 2.6, where the antenna array type, number of antenna elements, and antenna element spacing are specified on the GUI by the user.

- A path loss scatter plot entitled "PathLossPlot" generated after N ($N \geq 1$) continuous simulation runs with the same input parameters, as illustrated in Fig. 2.7. This figure shows omnidirectional path loss and directional path loss values for over the entire distance range generated from the N ($N \geq 1$) continuous simulation runs, along with the fitted PLE and shadow fading standard deviation using the minimum-mean-square-error (MMSE) method [5], [7]. In the legend of the figure "PathLossPlot", n denotes the pass loss exponent (PLE),

3-D AOD Power Spectrum - 28 GHz, UMi LOS, 140.9 m T-R Separation

■	-92 dBm
■	-84 dBm
■	-77 dBm
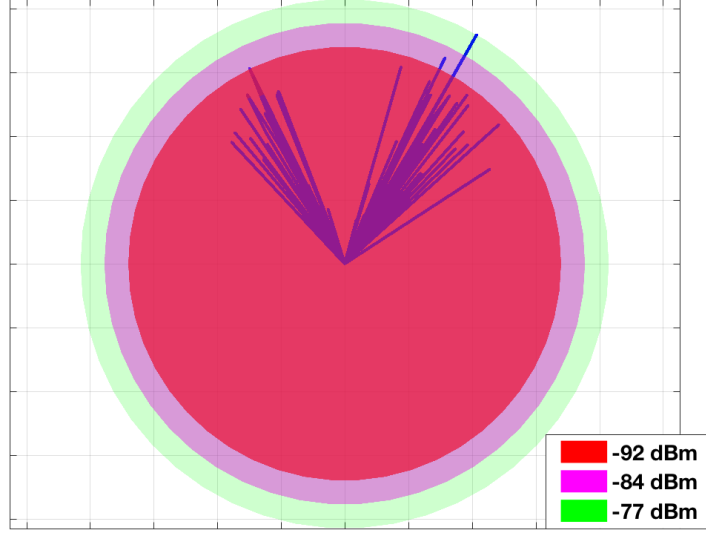
FIGURE 2.2: Example of a 3D AOD power spectrum generated from NYUSIM.

σ is the shadow fading standard deviation, "omni" denotes omnidirectional, "dir" represents directional, and "dir-best" means the direction with the strongest received power. For producing the directional path loss at each RX location, NYUSIM searches for all possible pointing angles in increments of the azimuth and elevation HPBWs of the TX/RX antenna specified by the user on the GUI after first generating the omnidirectional PDP. The TX/RX antenna gain pattern is calculated by NYUSIM using Eq. (2.1) in this user manual based on the azimuth and elevation HPBWs of TX and RX antennas specified by the user on the GUI. The directional path loss is equal to the transmit power plus the TX and RX antenna gains, minus the directional received power [1], [2], [61], [62]. For generating Fig. 2.7, the antenna azimuth and elevation HPBWs are set to 10.9° and 8.6°, respectively, at both the TX and the RX, to match the antenna HPBWs used in the 28 GHz measurements [1], [2]. The simulated PLE and shadow fading standard deviation values agree well with the measured results presented in Table V and Table VIII of [2]. Directional path loss and directional PLE will always be larger (i.e., a directional channel is more lossy) than the omnidirectional case, because the directional antenna will spatially filter out many multipath components due to its directional pattern, such that the RX receives fewer multipath components hence less energy, thereby the directional path loss is higher after removing the antenna gain effect from the received power [2], [7].

If the generated path loss in a simulation run exceeds the corresponding dynamic range, i.e., if there are no detectable multipath components, then it will be shown on the output figures that "No Detectable Multipath Components above the Threshold of XXX dBm", where the threshold value equals the transmit power in dBm minus the dynamic range in dB for that simulation run, such as -190 dBm. Note that no path loss data points will be shown
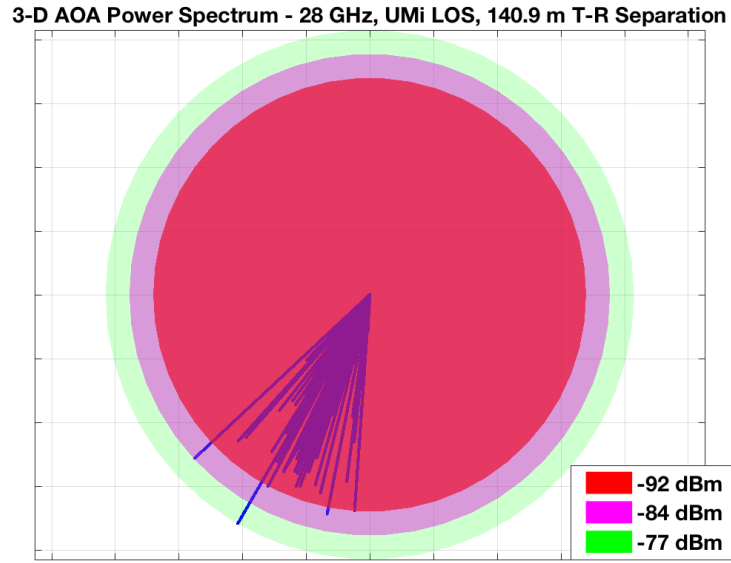
FIGURE 2.3: Example of a 3D AOA power spectrum generated from NYUSIM.
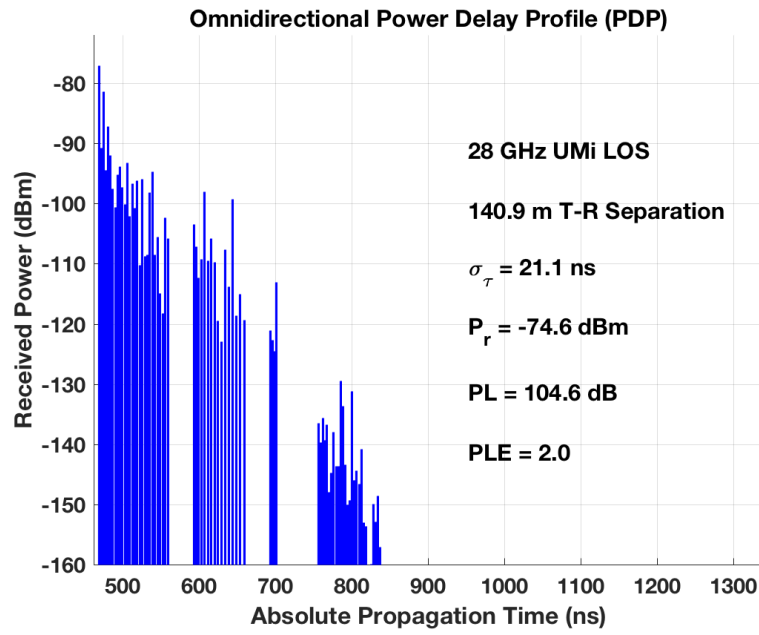
FIGURE 2.4: Example of an omnidirectional PDP generated from NYUSIM.

Directional PDP with Strongest Power

28 GHz UMi LOS

140.9 m T-R Separation

σ_τ = 2.4 ns

P_r = -27.8 dBm

PL = 107.0 dB

PLE = 2.1

TX Ant. HPBW: 10° AZ, 10° EL

TX Ant. Gain: 24.6 dBi

RX Ant. HPBW: 10° AZ, 10° EL

RX Ant. Gain: 24.6 dBi
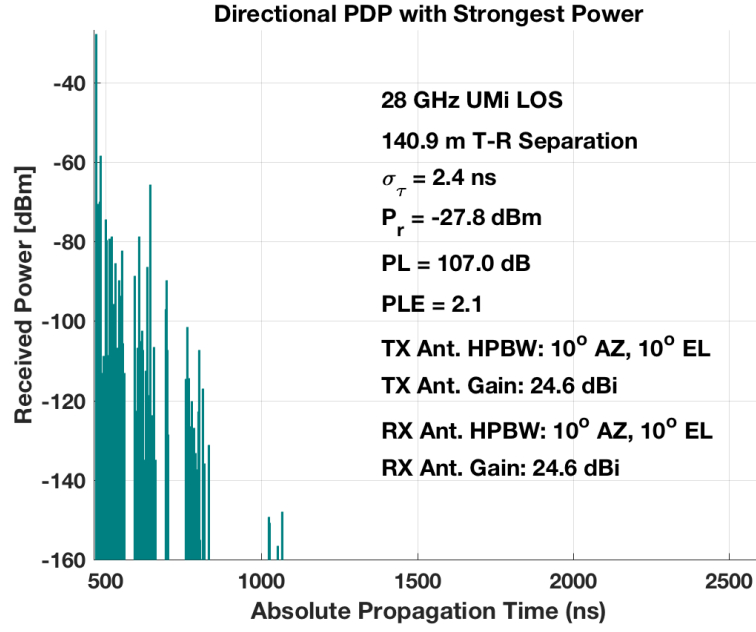
FIGURE 2.5: Example of a directional PDP with the strongest received power generated from NYUSIM. "Ant." denotes antenna.

Small Scale PDPs - 28 GHz, UMi LOS, 140.9 m T-R Separation
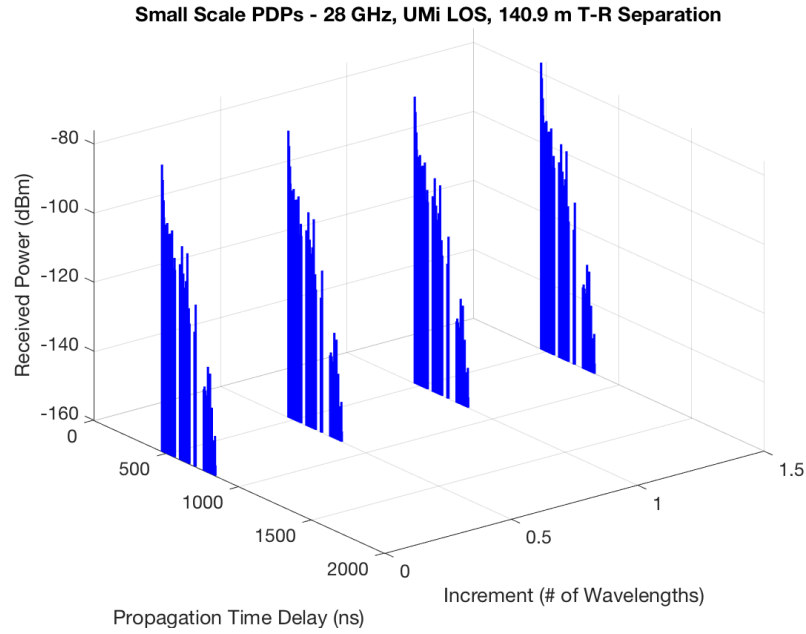
FIGURE 2.6: Example of the PDPs over different receive antenna elements generated from NYUSIM.

17
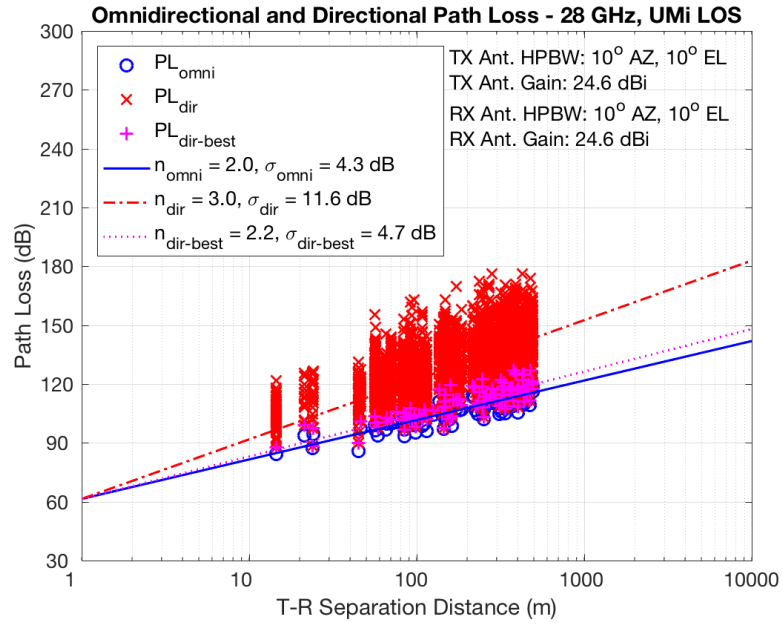
FIGURE 2.7: Example of a scatter plot showing the omnidirectional and directional path loss values generated from NYUSIM with 100 simulation runs for the 28 GHz UMi LOS scenario. n denotes the pass loss exponent (PLE), σ is the shadow fading standard deviation, "omni" denotes omnidirectional, "dir" represents directional, "dir-best" means the direction with the strongest received power, "Ant." denotes antenna, "AZ" and "EL" stand for azimuth and elevation, respectively.

on the path loss scatter plot as long as there are no detectable multipath components in the omnidirectional PDP, regardless of the directional PDP. Users may modify this in "NYUSIM_MainCode.m" per your own needs.

— Spatial Consistency Mode

The spatial consistency mode assumes a UT travels a specific path, and generates correlated and consecutive channel impulse responses for successive sampling points on the path. A series of spatially correlated and time-variant channel responses are easily generated in NYUSIM under the spatial consistency mode. A simulation run may produce hundreds or thousands of closely-spaced channel impulse responses based on the UT trajectory and velocity.

For each simulation run, five figures will be generated and stored that are based on the particular results of the simulation that is being run. These five figures will pop up on the screen for visual purposes. The contents of those figures are as follows.

- A map of spatially correlated shadow fading with the UT and BS locations and UT track is output as shown in Fig. 2.8. Some basic information such as frequency, environment, T-R separation distance, standard deviation of shadowing fading, track distance, velocity, is displayed in the figure.

- A map for spatially correlated LOS/NLOS condition using scenario-specific LOS probability is output as illustrated in Fig. 2.9, which indicates that all locations in a local area experience the same propagation condition (LOS or NLOS). Some basic information such as frequency, environment, T-R separation distance, standard deviation of shadowing fading, track distance, velocity is displayed in the figure.

- User track: The part of the map for spatially correlated shadow fading along which the UT moves as illustrated in Fig. 2.10. The moving direction and track distance are shown in this figure.

- Consecutive omnidirectional PDPs along the user trajectory are displayed in Fig. 2.11 to show the power variation and delay drifting of MPCs, where directional antenna gain patterns are implemented at the TX and/or RX. Some fundamental information such as frequency, environment, T-R separation distance, track distance, velocity is shown in the PDP plot.

- Consecutive directional PDPs with the strongest received power along the user trajectory are displayed in Fig. 2.12 to show the power variation and delay drifting of MPCs. Some fundamental information such as frequency, environment, T-R separation distance, track distance, velocity is shown in the PDP plot.

2.2.2 Output Data Files

— Drop-based Mode

For each simulation run, five sets of .txt files and five corresponding .mat files are generated, namely, "AODLobePowerSpectrum$n$_Lobe$x$.txt",
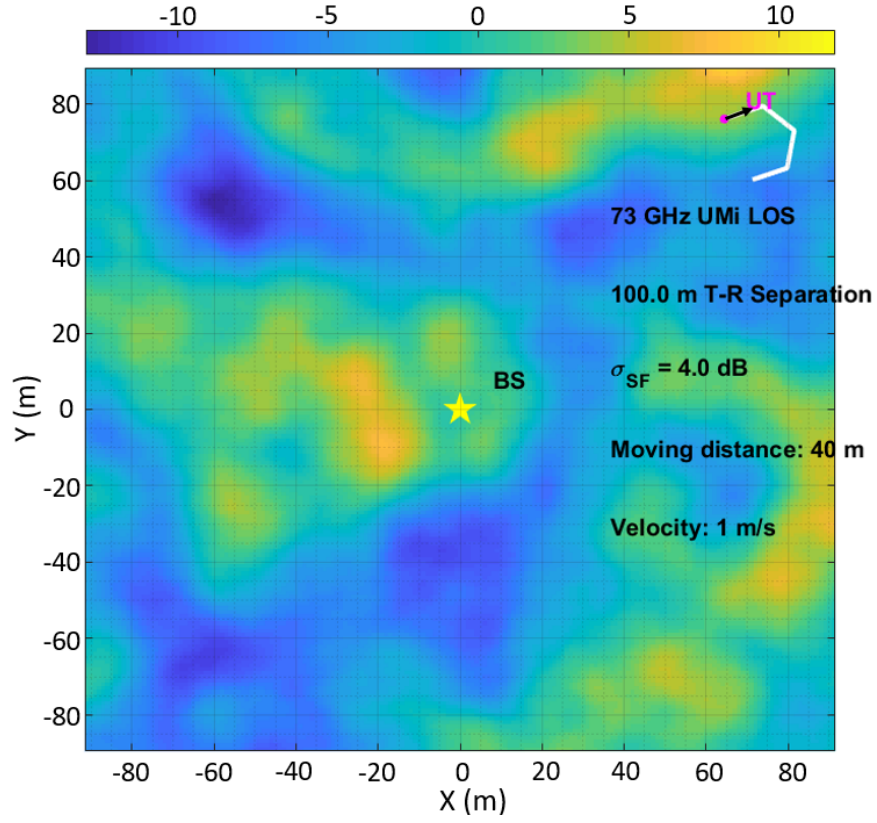
FIGURE 2.8: A map of spatially correlated shadow fading with the BS and UT locations. The map of spatially correlated shadow fading is generated by filtering a map of independent shadow fading using an exponential function in (3.5). Shadow fading [dB]∼N(0,4) in a UMi LOS scenario. T-R separation distance is 100 m.
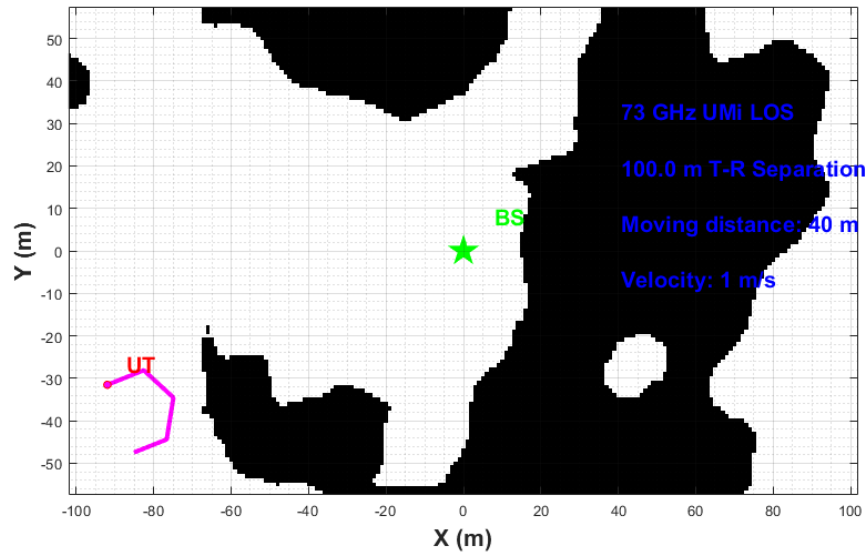
FIGURE 2.9: A sample map of spatially correlated LOS/NLOS condition
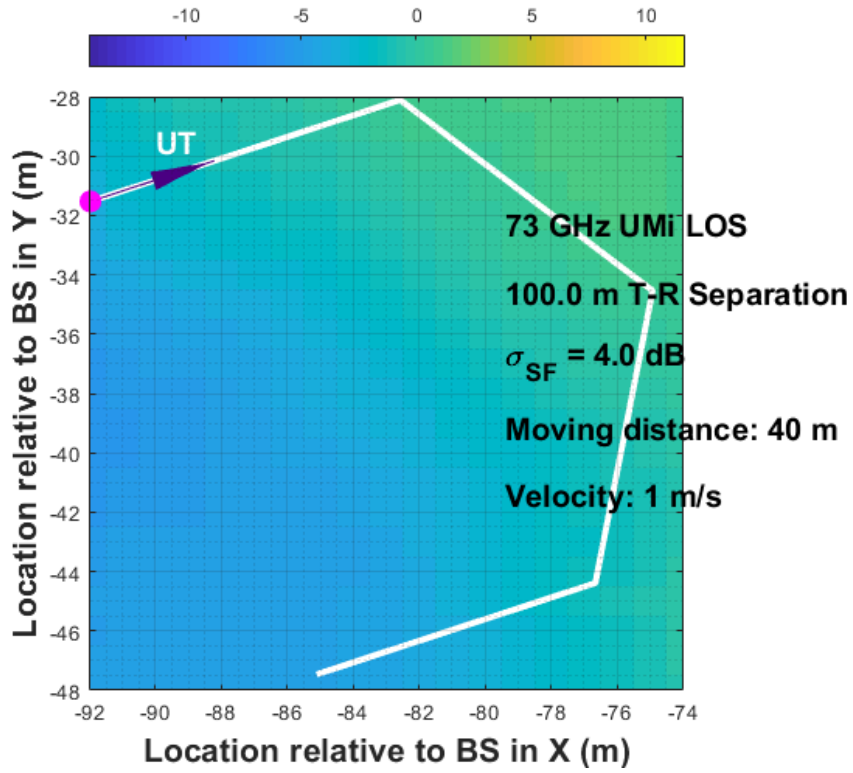
FIGURE 2.10: A sample user track
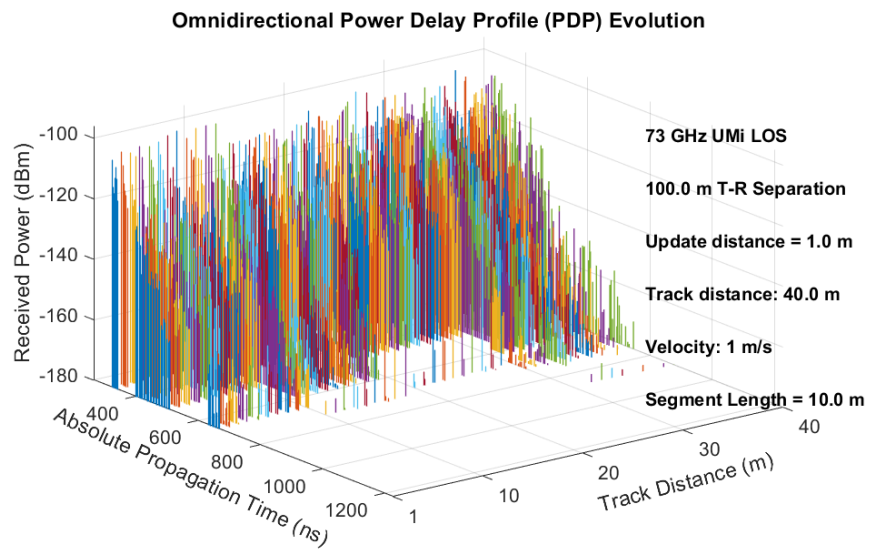
FIGURE 2.11: A sample consecutive omnidirectional PDPs
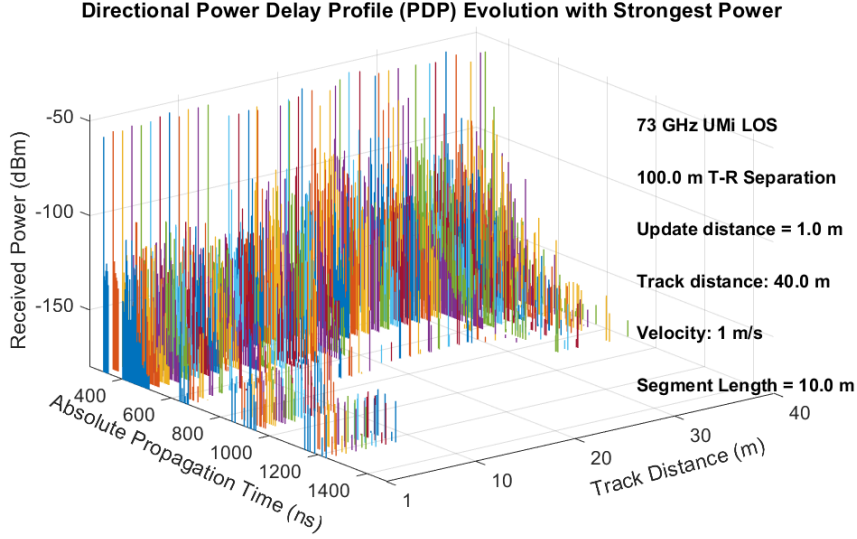
FIGURE 2.12: A sample consecutive directional PDPs

"AODLobePowerSpectrum$n$.mat", "AOALobePowerSpectrum$n$_Lobe$x$.txt", "AOALobePowerSpectrum$n$.mat", "OmniPDPn.txt", "OmniPDPn.mat", "DirectionalPDPn.txt", "DirectionalPDPn.mat", "SmallScalePDPn.txt", and "SmallScalePDPn.mat", where n denotes the nth RX location (i.e., n^{th} simulation run), and x represents the xth spatial lobe. After N ($N \geq 1$) continuous simulation runs with the same input parameters are complete, another three .txt files and three corresponding .mat files are produced, i.e., "BasicParameters.txt", "BasicParameters.mat", "OmniPDPInfo.txt", "OmniPDPInfo.mat", "DirPDPInfo.txt", and "DirPDPInfo.mat".

Each text file "AODLobePowerSpectrum$n$_Lobe$x$" is associated with the output figure of 3D AOD power spectrum, and contains five parameters (columns) of each resolvable multipath component in an AOD spatial lobe, which are listed and explained below.

1. pathDelay (ns): an array containing the absolute propagation time delays of all resolvable multipath components in nanoseconds (ns).

2. pathPower (mWatts): an array containing the received powers of all resolvable multipath components in mWatts.

3. pathPhase (rad): an array containing the phases of all resolvable multipath components in radians.

4. AOD (degree): an array containing the azimuth AODs of all resolvable multipath components in degrees.

5. ZOD (degree): an array containing the ZODs of all resolvable multipath components in degrees.

Note that inside the corresponding .mat file "AODLobePowerSpectrum$n$" is a structure containing the lobe matrices, each of which is composed of five columns as described above.

Each text file "AOALobePowerSpectrum$n$_Lobe$x$" is associated with the output figure of 3D AOA power spectrum, and contains five parameters

22

(columns) of each resolvable multipath component in an AOA spatial lobe, which are listed and explained below.

1. pathDelay (ns): an array containing the absolute propagation time delays of all resolvable multipath components in nanoseconds (ns).

2. pathPower (mWatts): an array containing the received powers of all resolvable multipath components in mWatts.

3. pathPhase (rad): an array containing the phases of all resolvable multipath components in radians.

4. AOA (degree): an array containing the azimuth AOAs of all resolvable multipath components in degrees.

5. ZOA (degree): an array containing the ZOAs of all resolvable multipath components in degrees.

Note that inside the corresponding .mat file "AOALobePowerSpectrum$n$" is a structure containing the lobe matrices, each of which is composed of five columns as described above.

Each .txt and .mat file "OmniPDPn" is associated with the output figure of omnidirectional PDP, and contains two columns: the first column denotes the propagation time delay in nanoseconds, and the second column represents the received power in dBm.

Each .txt and .mat file "DirectionalPDPn" is associated with the output figure of omnidirectional PDP with directional antenna gain patterns implemented, and contains two columns: the first column denotes the propagation time delay in nanoseconds, and the second column represents the received power in dBm.

Each .txt and .mat file "SmallScalePDPn" is associated with the output figure of the series of omnidirectional PDPs over RX antenna elements, and contains three columns: the first column denotes the receiver antenna separation in terms of number of wavelengths, the second column is the propagation time delay in nanoseconds, and the third column represents the received power in dBm. Note that the noise power is set to -150 dBm for visual purpose.

The text file "BasicParameters.txt" and the .mat file "BasicParameters.mat" subsume all the input parameter values as shown on the GUI when running the simulation.

The text file "OmniPDPInfo.txt" and the .mat file "OmniPDPInfo.mat" contain five columns where each column represents a key parameter for each of the N omnidirectional PDPs from N continuous simulation runs. The parameters are listed and explained below.

1. T-R Separation Distance (m)

2. Received Power (dBm): omnidirectional received power in dBm

3. Path Loss (dB): omnidirectional path loss in dB

4. RMS Delay Spread (ns): omnidirectional RMS delay spread in nanosecond (ns)

5. Ricean K-factor (dB): ratio of the strongest power of the multipath component (the first arriving multipath component in LOS) to the sum of powers of the other multipath components [4], converted from linear to the dB scale.

The text file "DirPDPInfo.txt" and the .mat file "DirPDPInfo.mat" contain 11 columns where each column represents a key parameter for each of the directional PDPs from N continuous simulation runs, where the same kind of parameters from each simulation run are cascaded in the same column. The parameters are listed and explained below.

1. Simulation run number

2. T-R Separation Distance (m)

3. Time Delay (ns): absolute propagation time delay of each resolvable multipath component in ns

4. Received Power (dBm): received power of each resolvable multipath component in dBm without antenna gains

5. Phase (rad): phase of each resolvable multipath component in radians

6. Azimuth AoD (degree): azimuth AoD of each resolvable multipath component in degrees

7. Elevation AoD (degree): elevation AoD of each resolvable multipath component in degrees

8. Azimuth AoA (degree): azimuth AoA of each resolvable multipath component in degrees

9. Elevation AoA (degree): elevation AoA of each resolvable multipath component in degrees

10. Path Loss (dB): directional path loss obtained by aligning the TX/RX antenna boresight on the AoD/AoA of each resolvable multipath component. The directional path loss equal the transmit power plus the TX/RX antenna boresight gains, minus directional received power.

11. RMS Delay Spread (ns): directional RMS delay spread in ns for each directional PDP

— Spatial Consistency Mode

For each simulation run, five sets of .txt files and five corresponding .mat files are generated, namely, "OmniPDP_Snap$x$.txt(/.mat)", "DirectionalPDP_Snap$x$.txt(/.mat)", "OmniPDPInfo.txt(/.mat)", "DirPDPInfo.txt(/.mat)", and "BasicParameters.txt(/.mat)". x represents the index of a channel snapshot.

Each text file "OmniPDP_Snap$x$" contains seven parameters (rows) of all resolvable MPCs (columns), which are listed and explained below.

1. pathDelay (ns): The first column represents delays of MPCs in ns.

2. pathPower (dBm): The second column represents powers of MPCs with omnidirectional antennas at TX and RX in dBm.

3. pathPhase (rad): The third column represents phases of MPCs in rad.

4. AOD (degree): The fourth column represents AODs of MPCs in degree.

5. ZOD (degree): The fifth column represents ZODs of MPCs in degree.

6. AOA (degree): The sixth column represents AOAs of MPCs in degree.

7. ZOA (degree): The seventh column represents ZOAs of MPCs in degree.

Each text file "DirectionalPDP_Snap$x$" contains seven parameters (rows) of all resolvable MPCs (columns) of the xth channel snapshot, which are listed and explained below.

1. pathDelay (ns): The first column represents delays of MPCs in ns.

2. pathPower (dBm): The second column represents powers of MPCs with user-specified directional antenna patterns at TX and RX in dBm.

3. pathPhase (rad): The third column represents phases of MPCs in rad.

4. AOD (degree): The fourth column represents AODs of MPCs in degree.

5. ZOD (degree): The fifth column represents ZODs of MPCs in degree.

6. AOA (degree): The sixth column represents AOAs of MPCs in degree.

7. ZOA (degree): The seventh column represents ZOAs of MPCs in degree.

The text file "OmniPDPInfo" contains five columns where each column represents a key parameter for each of omnidirectional PDPs from all simulated channel snapshots. Each row corresponds to a channel snapshot. The parameters are listed and explained below.

1. T-R Separation Distance (m)

2. Received Power (dBm): omnidirectional received power in dBm

3. Path Loss (dB): omnidirectional path loss in dB

4. RMS Delay Spread (ns): omnidirectional RMS delay spread in nanosecond (ns)

5. Ricean K-factor (dB): ratio of the strongest power of the multipath component (the first arriving multipath component in LOS) to the sum of powers of the other multipath components [4], converted from linear to the dB scale.

The text file "OmniPDPInfo" contains five columns where each column represents a key parameter for each of directional PDPs from all simulated channel snapshots, where the same kind of parameters from each channel snapshot are cascaded in the same column. The number of rows of each channel snapshot corresponds to the number of MPCs of that channel snapshot. The parameters are listed and explained below.

1. Snapshot index

2. T-R Separation Distance (m)

3. Received Power (dBm): directional received power in dBm

4. Path Loss (dB): omnidirectional path loss in dB

5. RMS Delay Spread (ns): omnidirectional RMS delay spread in nanosecond (ns)

The text file "BasicParameters" contains all user-input parameters such as channel parameters, antenna properties, spatial consistency parameters, and human blockage parameters.

3. Channel Model Supported by NYUSIM

The broadband statistical spatial channel model (SSCM) [3] developed by NYU is used in NYUSIM as a base. Spatial consistency procedure [14], [15], [45] and human blockage model [47], [59] developed by NYU, and the O2I penetration loss model in [50], [51] are used as additional features.

3.1 Supported Scenarios

Earlier versions included outdoor urban microcell (UMi), urban macrocell (UMa) and rural macrocell (RMa) scenarios, spatial consistency, human blockage, and outdoor-to-indoor penetration loss modeling components [13], [16]. With the release of NYUSIM 3.0, we have added the drop-based channel models for indoor office scenario developed based on the conventional drop-based statistical channel model [17], [18]. NYUSIM version 1.x implemented the initial drop-based channel model for outdoor UMi, UMa, and RMa scenarios including for carrier frequencies from 0.5 GHz to 100 GHz [13]. Then, NYUSIM version 2.x implemented a spatial consistency-enabled channel model with human blockage, and outdoor-to-indoor penetration loss modeling components for outdoor scenarios [16]. The current NYUSIM version 3.0 can simulate the indoor hotspot (InH) scenario and extends the carrier frequency range of 0.5 GHz to 150 GHz for the InH scenario [18]. Section 3.4 introduces the path loss model and the small-scale multipath channel model for the indoor scenario.

3.2 Path Loss Model

The close-in free space reference distance (CI) path loss model with a 1 m anchor point, with an extra attenuation term due to various atmospheric attenuation factors [52], is employed in NYUSIM, which is expressed as [2], [5], [63]:

$$\text{PL}^{\text{CI}}(f, d)[\text{dB}] = \text{FSPL}(f, 1 \text{ m})[\text{dB}] + 10n\log_{10}\left(\frac{d}{d_0}\right) + \text{AT}[\text{dB}] + \chi_\sigma^{\text{CI}},$$
$$\text{where } d \geq d_0 \text{ m}$$

(3.1)

where f denotes the carrier frequency in GHz, d is the 3D T-R separation distance, n represents the path loss exponent (PLE), d_0 denotes the free space reference distance in meters, which is set to 1 m in the NYUSIM channel model [5]. Users can change d_0 to some value other than 1 m in NYUSIM_MainCode.m, but d_0 should not exceed 5 m to guarantee free space propagation within d_0. AT is the attenuation term induced by the

27
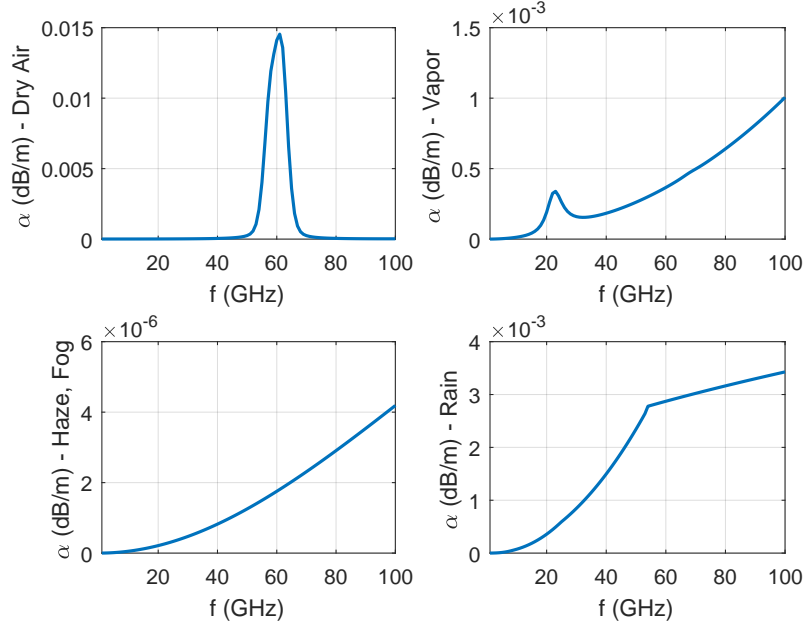
FIGURE 3.1: Propagation attenuation due to dry air, vapor, haze, and rain at mmWave frequencies, with a barometric pressure of 1013.25 mbar, a relative humidity of 80%, a temperature of 20°C, and a rain rate of 5 mm/hr [52].

atmosphere, $\chi_\sigma^{\mathrm{CI}}$ is a zero-mean Gaussian random variable with a standard deviation σ in dB, and $\mathrm{FSPL}(f, 1\,\mathrm{m})$ denotes the free space path loss in dB at a T-R separation distance of 1 m at the carrier frequency f:

$$\mathrm{FSPL}(f, 1\,\mathrm{m})[\mathrm{dB}] = 20\log_{10}\left(\frac{4\pi f \times 10^9}{c}\right) = 32.4[\mathrm{dB}] + 20\log_{10}(f) \quad (3.2)$$

where c is the speed of light, and f is in GHz. The term AT is characterized by:

$$\mathrm{AT}[\mathrm{dB}] = \alpha[\mathrm{dB/m}] \times d[\mathrm{m}] \quad (3.3)$$

where α is the attenuation factor in $\mathrm{dB/m}$ for the frequency range of 1 GHz to 100 GHz, which includes the collective attenuation effects of dry air (including oxygen), water vapor, rain, and haze [52]. d is the 3D T-R separation distance as in (3.1).

Fig. 3.1 illustrates example propagation attenuation values due to dry air, vapor, haze, and rain at mmWave frequencies from 1 GHz to 100 GHz, with a barometric pressure of 1013.25 mbar, a relative humidity of 80%, a temperature of 20°C, and a rain rate of 5 mm/hr, while the collective attenuation effects of these four main natural absorbers are displayed in Fig. 3.2. These results were obtained and reproduced from five reported controlled experiments on atmospheric attenuation [52].

Note that the CI model inherently has an intrinsic frequency dependency of path loss already embedded within the FSPL term. A useful property of (3.1) is that $10n$ describes path loss in dB in terms of decades of distances beginning at 1 m (making it very easy to compute power over distance in
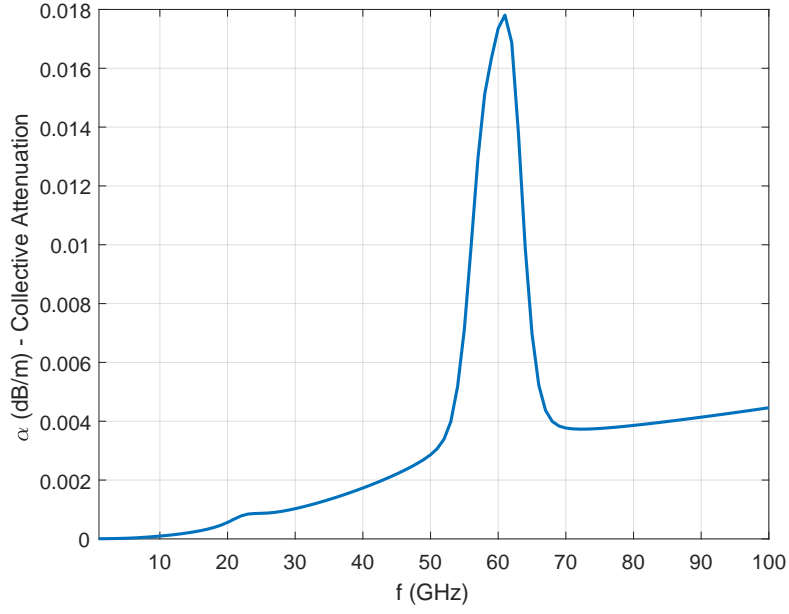
FIGURE 3.2: Collective attenuation effects of dry air, vapor, haze, and rain at mmWave frequencies, with a barometric pressure of 1013.25 mbar, a relative humidity of 80%, a temperature of 20°C, and a rain rate of 5 mm/hr [52].

one's mind).

The CI path loss model is based on fundamental principles of wireless propagation, dating back to Friis and Bullington, where the PLE parameter offers insight into path loss based on the environment, having a PLE value of 2 in free space (as shown by Friis) and a value of 4 for the asymptotic two-ray ground bounce propagation model (as shown by Bullington). Standardizing to a reference distance of 1 m makes comparisons of measurements and models simple, and provides a standard definition for the PLE, while enabling intuition and rapid computation of path loss [5].

Compared with the existing alpha-beta-gamma (ABG) path loss model used in 3GPP/ITU channel models [5], [7], [64], the CI model has an identical mathematical form, while offering intuitive appeal, better model parameter stability, and better prediction performance over a vast range of microwave and mmWave frequencies, distances, and scenarios, with fewer parameters [5].

In the current version of NYUSIM, the PLE and shadow fading standard deviations for UMi, UMa, and RMa scenarios are displayed in Table 3.1. The CI path loss model is employed for UMi and UMa scenarios, while for the RMa scenario, the CIH model (CI model with a height-dependent PLE) is adopted, as given by Eqs. (21) and (22) in [12]. The RMa PLE values in Table 3.1 are for a base station height of 35 m. **For RMa, the base station height provided by the user on the GUI is used for the CIH path loss model, while other scenarios do not use base station height at all.** Note that although the channel parameters for the UMi scenario are also used for

the UMa and RMa (except for the path loss model parameters) scenarios in this simulator, users can adjust the UMa and RMa channel parameters in the source code according to their own needs.

TABLE 3.1: Omnidirectional PLEs and shadow fading standard deviations for different scenarios in NYUSIM [5]. The RMa PLEs are for a base station height of 35 m [12].

Scenario		PLE	Shadow Fading Standard Deviation (dB)
UMi	LOS	2	4.0
	NLOS	3.2	7.0
UMa	LOS	2	4.0
	NLOS	2.9	7.0
RMa	LOS	2.31	1.7
	NLOS	3.07	6.7

3.2.1 Range Extension

Extensive mmWave propagation measurements conducted by NYU WIRELESS have shown that in dense urban environments, mmWave signals can cover around 200 m cell radius even under NLOS conditions [1], [2], [63], and is likely to reach 500 m in lightly populated urban and suburban areas. Furthermore, recent RMa propagation measurements at 73 GHz demonstrated over 10 km coverage range in clear weather [12]. To make NYUSIM cater for more users and wider applications, the maximum allowable T-R separation distance is extended from 500 m to 1 km in NYUSIM v1.6, by removing all the lower bounds on received power (including cluster power, subpath power, and lobe power), or equivalently, upper bounds on path loss, assuming there exits such a virtual receiver that can detect very low received power.

For LOS environments, calculated path loss beyond 500 m is still accurate using the NYUSIM path loss models (e.g., CI and CIH [5], [12]) since they are applicable to over 10 km distances. For NLOS environments, however, the NLOS path loss models employed in NYUSIM may not be accurate for distances larger than 500 m since they were developed for ranges within 500 m [5], thus caution should be given when setting the distance beyond 500 m for UMi or UMa NLOS scenarios. The dynamic range for multipath components in the extended range is extended to 220 dB from the default value of 190 dB used for distances no larger than 500 m.

3.3 Wideband Temporal/Spatial Clustering Algorithm

The SSCM given here utilizes *time clusters* (TC) and *spatial lobes* (SL) to model the omnidirectional CIR and corresponding joint AOD/AOA power spectra, which have been used successfully in modeling mmWave channels [3]. *Time clusters* are composed of multipath components traveling close in time, and that arrive from potentially different angular directions in a short propagation time window. *Spatial lobes* represent main directions of

arrival (or departure) where energy arrives over several hundred nanoseconds. This SSCM structure is motivated by field measurements, which have shown that multiple paths within a time cluster can arrive at unique pointing angles, detectable due to high gain directional antennas, and this feature has not been modeled in current 3GPP and WINNER models. These definitions de-couple the time and space dimensions by extracting temporal and spatial statistics separately. The definition of time cluster here considers multipath components traveling close in time, but that can arrive from many angular directions, whereas current 3GPP and WINNER models assume that subpaths belonging to a cluster travel along the same propagation path, but arrive at the same time delay over a certain AOA angular spread.

The TCSL approach implements a physically-based clustering scheme (e.g., the use of a fixed inter-cluster void interval representing the minimum propagation time between likely reflection or scattering objects) derived from field observations, and can be used to extract time cluster and spatial lobe statistics for any ray-tracing or measurement data sets [3]. The time-partitioning methodology delineates the beginning and end times of each time cluster, using a 25 ns minimum inter-cluster void interval. Sequentially arriving multipath components that occur within 25 ns of each other are assumed to belong to one time cluster. The 3D spatial distribution of received power was reconstructed from the 28 GHz and 73 GHz LOS and NLOS directional received powers by linearly interpolating adjacent power level segments in azimuth and elevation with a 1° resolution, and extracting 3D spatial angular statistics. A -10 dB threshold below maximum peak power in the 3D power spectrum is used in both LOS and NLOS environments, where all power segments below this threshold are disregarded for further processing. Fig. 3.3 illustrates an omnidirectional PDP, where there are four multipath taps which are grouped into two time clusters with exponentially decaying amplitudes. The four multipath taps are then grouped into two AOA spatial lobes, as shown in Fig. 3.4.

Sample Omni. PDP Output Function
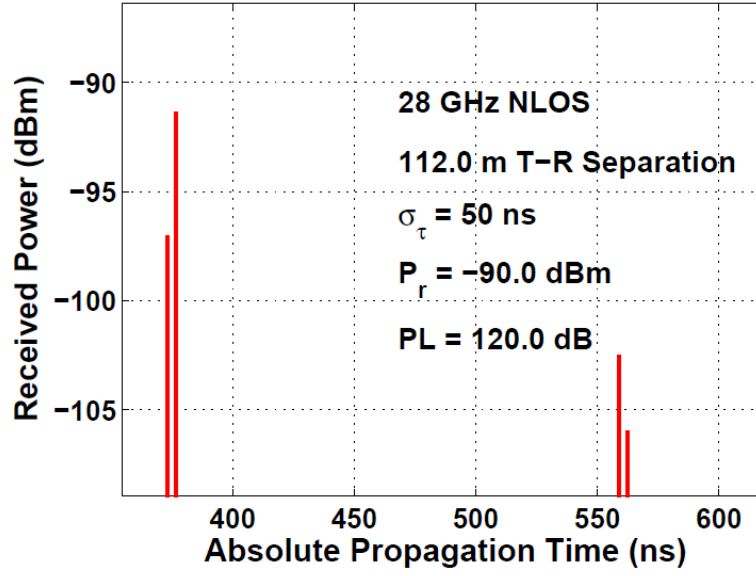
FIGURE 3.3: Example of an omnidirectional PDP with four multipath taps [3].

3-D AOA Power Spectrum - 28 GHz NLOS
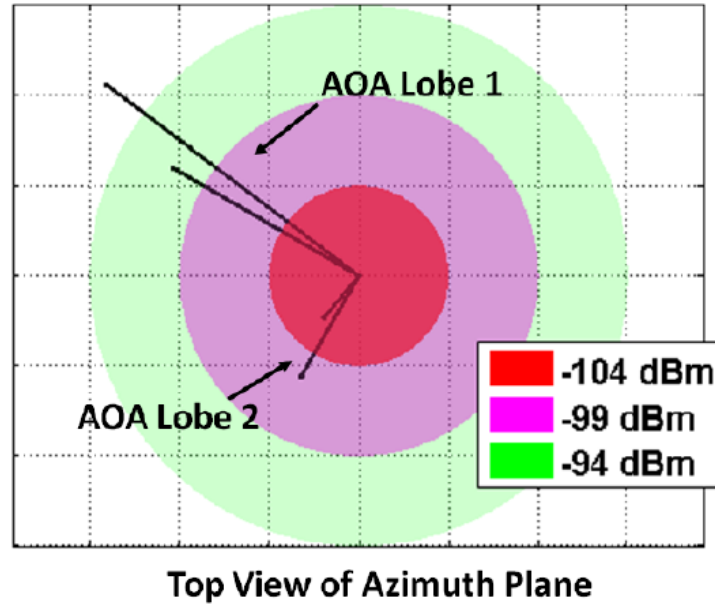
FIGURE 3.4: Example of an AOA power spectrum with four multipath taps [3].

It is noteworthy that for the RMa scenario, the number of time clusters and the number of spatial lobes are both set to one, and the maximum number of multipath components is set to two, based on our RMa mmWave field measurements [12]. The base station height is only used for RMa in the CIH path loss model but not other scenarios.

TABLE 3.2: Measured PLE and SF for 28 and 140 GHz in LOS and NLOS scenarios.

PLE, SF [dB]	28 GHz	140 GHz
LOS	1.2, 1.8	1.8, 2.9
NLOS	2.7, 9.7	2.7, 6.6

3.4 Indoor statistical channel model

3.4.1 Large-scale Path Loss Model

Path loss models describe the distance-power law that the received power decreases exponentially with distance and are commonly used in the prediction of signal strength and cell range. A popular path loss model, close-in free space reference distance (CI) path loss model with 1 m reference distance, is given by 3.1.

PLE n indicates that the power decays by $10n$ dB per decade of distance beyond 1 m [65]. Fig. 3.5 shows that PLE for 28 GHz LOS and NLOS scenarios via minimum mean square error (MMSE) fitting are 1.2 and 2.8, respectively. 1.2 is derived from 2 MetroTech dataset for 28 GHz LOS case, which is lower than 1.3-1.9 found in the literature [66]–[68]. To verify this low PLE, we conducted LOS measurements in another office building, 370 Jay, at 28 GHz. The resulting PLE for 370 Jay dataset is also 1.2, suggesting that the power attenuates much slower (12 dB per ten meters) than values reported in the literature, which might be attributed to the strong waveguide effect of long and narrow corridors in the indoor environment. The PLE and the standard deviation of shadow fading (SF) measured at 28 and 140 GHz in LOS and NLOS scenarios are given in Table 3.2.
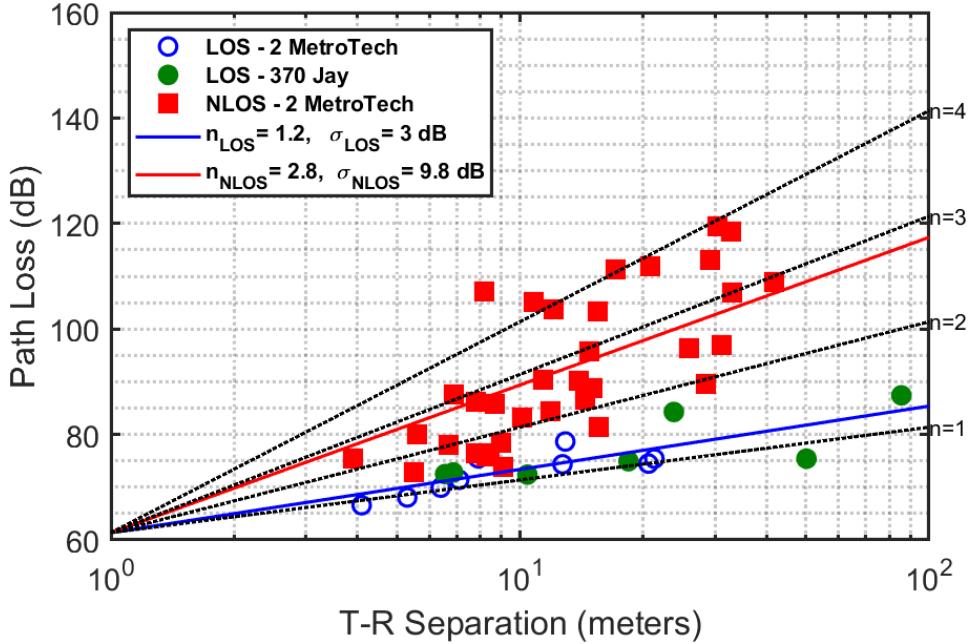
FIGURE 3.5: 28 GHz indoor omnidirectional path loss scatter plot and MMSE-fitted CI path loss model with distance for LOS and NLOS scenarios [17].

3.4.2 Small-scale Channel Impulse Response Model

Input parameters of channel generation procedure

The outdoor and indoor scenarios share the same set of input parameters for channel coefficient generation procedure, but the probabilistic distribution of several parameters such as the number of time clusters, cluster subpaths, and spatial lobes are different. The number of time clusters and cluster subpaths for NLOS environment is no longer uniformly distributed. Instead, the number of time clusters for the indoor environments is Poisson distributed, and the number of cluster subpaths is modeled as a composite distribution of a discrete exponential (DE) distribution and a δ-function, as given in Table 3.3.

Parameter frequency-dependency for the indoor scenario

For the indoor scenario, two sets of channel measurements (28 GHz and 140 GHz) are available for developing the NYUSIM channel model across the mmWave and sub-Terahertz bands. Distinct channel characteristics measured at 28 and 140 GHz (e.g., the number of time clusters and cluster subpaths) motivated us to make generated channels frequency-variant by using frequency-dependent input parameters listed in Table 3.3. Since only two center frequencies (i.e., 28 GHz and 140 GHz) were measured, a linear interpolation is used to generate channel parameters between 28 and 140 GHz. Note that the allowable user-specified carrier frequency of NYUSIM ranges from 0.5 GHz to 150 GHz for the indoor scenario. Thus, the input parameters for frequencies below 28 GHz are set to be equal to the values at 28 GHz; the input parameters for frequencies above 140 GHz are set to be equal to the values at 140 GHz. The relation is given by

$$p(f) = \begin{cases} p(28) & , f \leqslant 28 \\ \frac{p(140)-p(28)}{140-28}f + \frac{5p(28)-p(140)}{4} & , 28 < f < 140 \\ p(140) & , f \geqslant 140 \end{cases} \quad (3.4)$$

where $p(f)$ denotes an input parameter at frequency f (GHz).

A special case is the PLE for the indoor LOS scenario due to the low value of the measured PLE. The measured PLE in the 2 MetroTech building for 28 GHz LOS case is 1.2 [17] while the reported PLEs in the literature for the indoor LOS scenario at 28 and 60 GHz are 1.7 [66] and 1.88 [67], respectively. To verify the measured PLE in the 2 MetroTech building, we conducted another set of indoor LOS measurements in the 370 Jay office building, which showed that the resulting PLE is also 1.2 [17]. Such low PLE is attributed to strong waveguide effect in the corridor.

We also found the measurement results at 1.5 GHz from [69], which showed that the PLE for the indoor scenario was about 1.8. Thus, it is not sensible to apply a single-slope function for frequencies from 0.5 to 150 GHz; however, a dual-slope function is used specifically for the indoor LOS scenario. Without loss of generality, we assume another frequency reference point at 1 GHz with PLE 1.8. Similar to the interpolation applied above, another linear interpolation between 1 and 28 GHz is adopted to make the simulated PLE more realistic. Fig. 3.6 shows the frequency-dependent PLE values for the indoor LOS scenario.
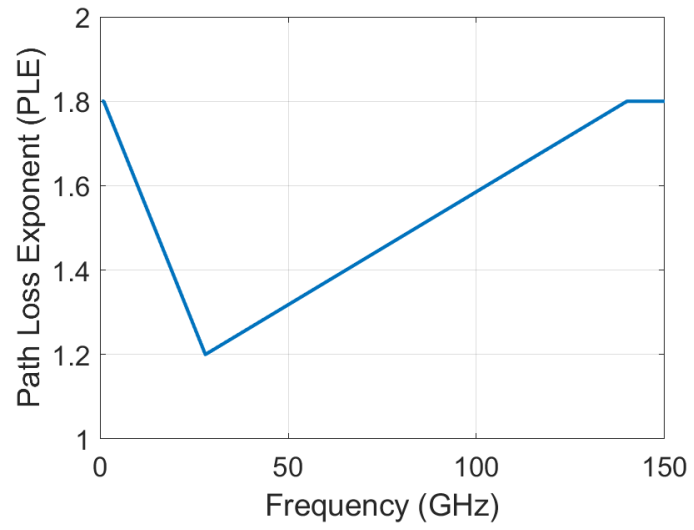
FIGURE 3.6: Frequency-dependent PLE for the indoor LOS scenario.

TABLE 3.3: INPUT PARAMETERS FOR CHANNEL COEFFICIENT GENERATION PROCEDURE [18]

Channel Parameters	28 - 73 GHz UMi [25]	28 - 140 GHz InH [18]
# Time clusters N	$N \sim \mathrm{DU}(1, N_c)$	$N \sim \mathrm{Poisson}(\lambda_c)$
# Cluster subpaths M_n	$M_n \sim \mathrm{DU}(1, M_s)$	$M_n \sim (1 - \beta)\delta(M_n) + \mathrm{DE}(\mu_s)$
Cluster delay τ_n (ns)	$\tau_n'' \sim \mathrm{Exp}(\mu_\tau) \text{ or } \mathrm{Logn}(\mu_\tau, \sigma_\tau)$ $\Delta\tau_n = \mathrm{sort}(\tau_n'') - \min(\tau_n'')$ $\tau_n = \begin{cases} 0 & , n = 1 \\ \tau_{n-1} + \rho_{M_{n-1}, n-1} + \Delta\tau_n + \mathrm{MTI} & , n = 2, ... N \end{cases}$	
Intra-cluster delay $\rho_{m,n}$ (ns)	$\rho_{m,n} = \left[\dfrac{1}{B_{bb}} \times (m - 1) \right]^{1 + X_n},$ $m = 1, 2, ..., M_n, \ n = 1, 2, ..., N$	$\rho_{m,n} \sim \mathrm{Exp}(\mu_\rho)$
Cluster power P_n (mW)	$P_n' = \bar{P}_0 e^{-\frac{\tau_n}{\Gamma}} 10^{\frac{Z_n}{10}},$ $P_n = \dfrac{P_n'}{\sum_{k=1}^{N} P_k'} \times P_r[mW],$ $Z_n \sim N(0, \sigma_Z), \ n = 1, 2, ..., N$	
Subpath power $\Pi_{m,n}$ (mW)	$\Pi_{m,n}' = \bar{\Pi}_0 e^{-\frac{\rho_{m,n}}{\gamma}} 10^{\frac{U_{m,n}}{10}},$ $\Pi_{m,n} = \dfrac{\Pi_{m,n}'}{\sum_{k=1}^{M_n} \Pi_{k,n}'} \times P_n[mW],$ $U_{m,n} \sim N(0, \sigma_U), \ m = 1, 2, ..., M_n$	
SP phase φ (rad)	$\mathrm{Uniform}(0, 2\pi)$	
# Spatial lobes L	$L_{\mathrm{AOD}} \sim \min\{L_{\max}, \max\{1, \mathrm{Poisson}(\mu_{\mathrm{AOD}})\}\}$ $L_{\mathrm{AOA}} \sim \min\{L_{\max}, \max\{1, \mathrm{Poisson}(\mu_{\mathrm{AOA}})\}\}$	$L_{\mathrm{AOD}} \sim \mathrm{DU}(1, L_{\mathrm{AOD,max}})$ $L_{\mathrm{AOA}} \sim \mathrm{DU}(1, L_{\mathrm{AOA,max}})$
SL mean angle ϕ_i, θ_i (^{o})	$\phi_i \sim U(\phi_{\min}, \phi_{\max}), \phi_{\min} = \frac{360(i-1)}{L}, \phi_{\max} = \frac{360i}{L}, i = 1, 2, ..., L$ $\theta_i \sim N(\mu_l, \sigma_l)$	
SP angle offset $\Delta\phi_i, \Delta\theta_i$ w.r.t ϕ_i, θ_i (^{o})	$i \sim \mathrm{DU}[1, L_{\mathrm{AOD}}], j \sim \mathrm{DU}[1, L_{\mathrm{AOA}}]$ $(\Delta\phi_i)_{m,n,\mathrm{AOD}} \sim \mathcal{N}(0, \sigma_{\phi,\mathrm{AOD}})$ $(\Delta\theta_i)_{m,n,\mathrm{ZOD}} \sim \mathcal{N}(0, \sigma_{\theta,\mathrm{ZOD}})$ $(\Delta\phi_j)_{m,n,\mathrm{AOA}} \sim \mathcal{N}(0, \sigma_{\phi,\mathrm{AOA}})$ $(\Delta\theta_j)_{m,n,\mathrm{ZOA}} \sim \mathcal{N}(0, \sigma_{\theta,\mathrm{ZOA}})$	

3.5 Channel Bandwidth and Resolvable MPC

The temporal resolution of wireless channels depend on the channel bandwidth. More specifically, the time resolution is the inverse of one half of the RF bandwidth. For example, 800 MHz channel bandwidth corresponds to 2.5 ns time resolution, which means two MPCs within 2.5 ns cannot be resolved by the receiver. Two extreme cases of bandwidth are single-frequency continuous wave and ideally infinite bandwidth, which respectively correspond to infinite and zero time resolution. Thus, fewer MPCs can be resolved at narrower bandwidth. When MPCs arrive within a time bin, these MPCs are vectorially summed. The functions, "getNewPower-Spectrum.m" and "getLocalCIR.m", are used to generate bandwidth-adjusted power spectrum for SISO and MIMO channels, respectively. Note that in the angular domain, the angular information of the first arriving MPC in a set of MPCs, which falls in one time bin (cannot be resolved) will be used as the angles of the combined MPC.

3.6 Spatial Consistency Procedure

In NYUSIM 3.0, spatial consistency is only implemented for outdoor scenarios. Spatial consistency indicates continuous and realistic channel evolution along the UT trajectory in a local area. To realize spatial consistency, spatially correlated large-scale parameters such as shadow fading, LOS/NLOS condition are generated, and time-variant small-scale parameters such as angles, power, delay, phase of each MPC are generated [14], [15]. The correlation distance of LSPs precisely characterizes the concept of "a local area", which also confines the length of a channel segment (where a channel segment is 10-15 m long) [15]. In a channel segment, the channels are considered highly correlated and updated using spatial consistency procedure. A channel segment can be divided into several channel snapshots. The distance between two channel snapshots is the update distance (e.g. 1 m), which means the channel coefficients are updated for every 1 m increment along a traveled path.

Spatially Correlated Map of Shadow Fading: LSPs defined in the 3GPP 38.901 model are delay spread, angular spread, Rician K factor, SF, and LOS/NLOS condition [70]. The two LSPs explicitly used in the channel generation procedure in NYUSIM is SF and LOS/NLOS condition. Spatially correlated SF and LOS/NLOS condition values are generated in the same way. For SF, a 2-dimensional (2-D) grid map is generated to contain values of spatially correlated SF in a simulated area. The granularity of the map is set to be 1 m, which means the distance between two neighboring grid points is 1 m. SF is modeled as a log-normal random variable with zero mean and σ dB standard deviation as shown in (3.1). The map of SF is initialized by assigning an i.i.d normal distributed random variable at each grid. A 2-D exponential filter is applied to the map, which is given by [14]:

$$h(p, q) = \exp(-\frac{\sqrt{p^2 + q^2}}{d_{\text{co}}}), \tag{3.5}$$

where p and q are coordinates with respect to the center of the filter. $\sqrt{(p^2+q^2)}$ represents the distance to the center of the filter. d_{co} is the correlation distance of SF. L is the length of the filter, which is set as 8-fold d_{co} since the correlation is negligible beyond 4-fold d_{co}. Applying this 2-D filtering, the correlated values in the map is calculated by:

$$M_c(i,j) = \sum_p \sum_q h(p,q)M(i-p+1, j-q+1) \tag{3.6}$$

where M_c is the correlated map and M is the initialized independent map. i and j are the coordinates of grid points in the map. A map of spatially correlated shadow fading over a 200 m x 200 m area is shown in Fig. 2.8. The correlation distance of shadow fading in a UMi LOS scenario is set to be 10 m [15], [45]. The UT moved 40 m in a partial hexagon track, which is also illustrated in Fig. 2.8. Shadow fading varies from -10 dB to 10 dB in a continuous manner. Similar shadow fading values are observed at closely spaced locations whereas independent values for close locations are always used in the drop-based model.

Spatially Correlated Map of LOS/NLOS Condition: LOS/NLOS condition is important to evaluate the wireless communication systems, especially at mmWave frequencies. LOS/NLOS condition will determine path loss exponent (PLE) and variance of shadow fading, and the transition between LOS and NLOS condition will cause a drastic change in the received power when a user moves. LOS propagation can provide more reliable performance in mmWave communications as compared to NLOS propagation. Generally, LOS/NLOS condition does not change when a user moves in a local area (within the correlation distance of LOS/NLOS condition).

By generating a map of spatially correlated LOS/NLOS condition, a UT will experience the same visibility condition in a local area. In each channel segment, the visibility condition is kept constant, which indicates the large-scale parameters are spatially consistent. When a UT moves from one channel segment to the next channel segment, and the visibility condition is changed according to the UT location in the map, different values of parameters for LOS or NLOS are used to initialize the channel coefficients for the new channel segment. In other words, LOS/NLOS transition can be realized by the spatially correlated map.

Similar with the spatially correlated shadow fading, a 2-D grid map is also generated for LOS/NLOS condition. The same 2-D double-side exponential function is used. The length of filter coefficient is 8-fold correlation distance of LOS/NLOS condition (e.g. 50 m in UMi and UMa scenario [70]) divided by the granularity (e.g. 1 m), since the correlation coefficient of the filter is close to zero beyond fourfold correlation distance. A 2-D geographical grid map is generated, the size of which depends on the distance between BS and UT and the UT trajectory. The granularity of the map is determined such as 1 m. An i.i.d standard Gaussian random variable is associated to each grid point. Then, the 2-D grid map is filtered by the 2-D exponential function and have spatially correlated Gaussian random variables. A transformation from Gaussian distribution to uniform distribution is required to generate spatially correlated uniform random variables,

which is given by

$$\tilde{u} = g^{-1}(\tilde{v}) = F_{\tilde{u}}^{-1}(F_{\tilde{v}}(\tilde{v})), \tag{3.7}$$

where $\tilde{u}$ and $\tilde{v}$ are the spatially correlated uniform and Gaussian random variable, respectively. $F_{\tilde{u}}$ and $F_{\tilde{v}}$ are the CDF of the uniform distribution and Gaussian distribution, respectively. Using cumulative distribution function (CDF) approach, the relation is given by

$$\tilde{u} = \frac{1}{2}\left(1 + \mathrm{erf}(\frac{\tilde{v}}{\sqrt{(2)}})\right), \tag{3.8}$$

where erf(x) is the error function and given by

$$\int_{-\infty}^{x} \frac{1}{\sqrt{(2\pi)}} \exp(-\frac{t^2}{2}) dt, \tag{3.9}$$

The method of deciding the LOS/NLOS condition at a certain location is to compare a uniformly distributed random variable to LOS probability at that location. There are several LOS probability models available in the literature such as 3GPP 38.901 model [70], 5GCM model [51], and METIS model [71]. In NYUSIM, NYU squared model for LOS probability is applied for UMi and UMa scenario [72], and 3GPP 38.901 model for LOS probability is used for RMa scenario [70]. The LOS probability model used in NYUSIM for three scenarios is given in Table 3.4.

TABLE 3.4: LOS probability models in the UMi, UMa and RMa scenario [72]

Scenarios	LOS probability models (distances are in meters)	Parameters
UMi [72]	$\mathrm{Pr}_{\mathrm{LOS}}(d) = (\min(d_1/d, 1)(1 - \exp(-d/d_2)) + \exp(-d/d_2))^2$	$d_1 = 22$ m $d_2 = 100$ m
UMa [72]	$\mathrm{Pr}_{\mathrm{LOS}}(d) = ((\min(d_1/d, 1)(1 - \exp(-d/d_2)) + \exp(-d/d_2))(1 + C(d, h_{UT})))^2$ where, $$C(d, h_{UT}) = \begin{cases} 0, & h_{UE} < 13 \text{ m} \\ \left(\frac{h_{UT}-13}{10}\right)^{1.5} g(d), & 13 \text{ m} \le h_{UT} \le 23 \text{ m} \end{cases}$$ and, $$g(d) = \begin{cases} 0, & d \le 18 \text{ m} \\ (1.25 \times 10^{-6}) \cdot d^3 \exp(-d/150), & d > 18 \text{ m} \end{cases}$$	$d_1 = 20$ m $d_2 = 160$ m
RMa [70]	$$\mathrm{Pr}_{\mathrm{LOS}}(d) = \begin{cases} 1, & d < 18 \text{ m} \\ \exp(-\frac{d-10}{1000}), & d > 10 \text{ m} \end{cases}$$	
Note : d is the 2D Euclidean distance between BS and UT.		

Thus, a UT at a certain location under LOS condition or NLOS condition is determined by comparing correlated value $\tilde{u}$ to the LOS probability $Pr_{\mathrm{LOS}}(d)$

$$\text{Condition} = \begin{cases} \text{LOS} & \tilde{u} <= \mathrm{Pr}_{\mathrm{LOS}}(d) \\ \text{NLOS} & \tilde{u} > \mathrm{Pr}_{\mathrm{LOS}}(d) \end{cases} \tag{3.10}$$

A map of spatially correlated LOS/NLOS condition in UMi scenario using LOS probability equations in Table 3.4 shown in Fig. 3.7. The "white" represents LOS whereas the "black" represents NLOS. The size of a UMi cell for mmWave communication systems is typically 200 m [72]. Thus, the simulated area is set to be 400 m x 400 m. The correlation distance is 15 m

[73]. The granularity of the map is 1 m. The heights of the BS and UT are 10 m and 1.5 m, respectively.
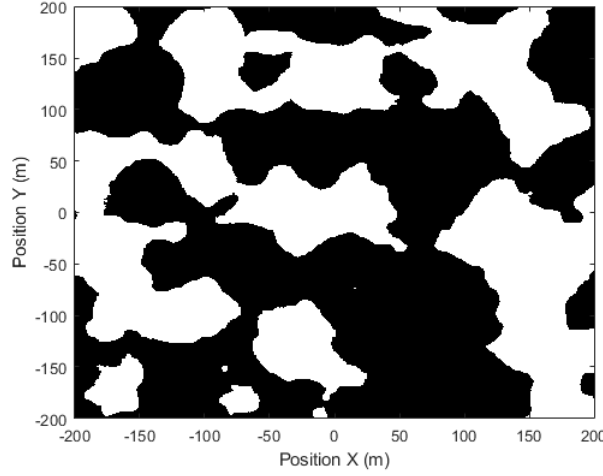
FIGURE 3.7: A 400 m x 400 m spatially correlated map for LOS/NLOS condition in UMi scenario using a 2-D filter. The correlation distance is 15 m. The granularity of the map is 1 m. The heights of the BS and UT are 10 m and 1.5 m, respectively. The LOS and NLOS condition transition may happen along the UT trajectory according to the UT location in the map.

Small-scale Parameters: Small-scale parameters in the NYUSIM channel model are angles (i.e. AOD, ZOD, AOA, ZOA), delay, power, phase for each MPC. A geometry-based approach using multiple reflection surfaces originated from [74] is derived to update the angles for each NLOS MPC. First, the update equations for LOS component is derived based on geometry. For NLOS components, the mirror images of a UT and the UT velocity are calculated by using multiple reflection surfaces. Then, the NLOS components can be updated using the same equations as the LOS component with mirrored UT location and velocity. The delay and phase of each MPC is updated simply based on the path length change using Law of cosines [16], [45]. The power of each MPC is updated by redistributing cluster powers and MPC powers in each cluster following the same way that these powers were initialized using the cluster time excess delay and intra-cluster time excess delay, explained in [25].

LOS case: To derive the update equations of four angles (AOD, ZOD, AOA, and ZOA) of UT at time t along the UT trajectory, we assume that the UT only has azimuthal movement for simplicity, which means $\theta_v = 90°$. The UT location at time t_0 is [75]

$$
\begin{pmatrix}
d_{\text{2D}} \cos(\phi_{\text{AOD}}(t_0)) \\
d_{\text{2D}} \sin(\phi_{\text{AOD}}(t_0)) \\
h_{UE}
\end{pmatrix}, \tag{3.11}
$$

40

where d_{2D} is the projection of the T-R separation distance r in the azimuth plane. The UT location at time t is [75]

$$\begin{pmatrix} d_{2D} \cos(\phi_{AOD}(t_0)) + vt \cos(\phi_v) \\ d_{2D} \sin(\phi_{AOD}(t_0)) + vt \sin(\phi_v) \\ h_{UE} \end{pmatrix} \quad (3.12)$$

Then, the accurate AOD at time t can be given by [75]

$$\phi_{AOD}(t) = \arctan(\frac{d_{2D} \sin(\phi_{AOD}(t_0)) + vt \sin(\phi_v)}{d_{2D} \cos(\phi_{AOD}(t_0)) + vt \cos(\phi_v)}). \quad (3.13)$$

The problem for this accurate AOD update shown above is computationally expensive. Considering that the moving distance (less than a meter) is much smaller than the separation distance between TX and RX (r), the change of r can be ignored. Then, the moving distance (or trajectory) of the UT can be approximated as the corresponding arc length with the BS as the center as shown in Fig. 3.8. The change of AOD, $\Delta\phi_{AOD}$ can be calculated by the central angle of the arc. Thus, it is assumed that the track distance in each channel snapshot is set to be within a meter, which, usually, is much smaller than the distance (r) between the BS and UT in outdoor environments such as UMi and UMa. The angle deviation or change is expected to be small, and user track within 1 m can be regarded as a short arc centering at BS with radius r. Thus, a linear approximation method is valid to update time-variant angles, which is given by [70], [74]

$$\phi_{angle}(t_k) = \phi_{angle}(t_{k-1}) + S_{angle} \cdot \Delta t, \quad (3.14)$$

where "angle" is an index for AOD, ZOD, AOA, and ZOA. t_k and t_{k-1}
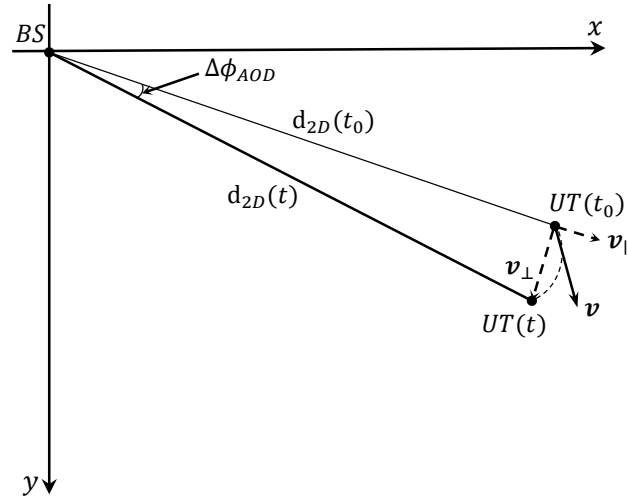
FIGURE 3.8: UT movement and change of AOD in the azimuth plane. The moving distance of the UT is approximated as the corresponding arc length with the BS as the center

are two successive time instances, and the interval between two successive time instances is Δt. S_{angle} is the linear changing rate for "angle".
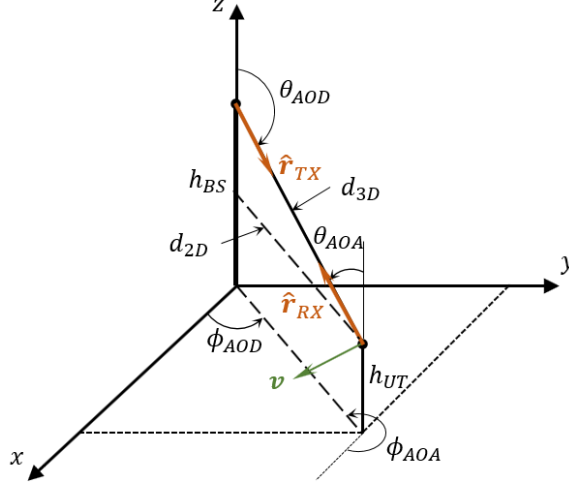
FIGURE 3.9: 3D geometry illustration of the coordination system for a LOS component. AOD and ZOD from the BS and AOA and ZOA from the UT are shown.

To obtain expressions for S_{angle}, the definitions of four angles (AOD, ZOD, AOA, ZOA) and the GCS for LOS component is shown in 3.9. $\mathbf{r}_{RX}$ is the spherical unit vector with AOD (ϕ_{AOD}) and ZOD (θ_{ZOD}), which is given by [76]

$$\mathbf{r}_{RX}(t) = -r(t) \begin{bmatrix} \sin\theta_{\text{ZOD}}(t)\cos\phi_{\text{AOD}}(t) \\ \sin\theta_{\text{ZOD}}(t)\cos\phi_{\text{AOD}}(t) \\ \cos\theta_{\text{ZOD}}(t) \end{bmatrix}, \tag{3.15}$$

where $r(t)$ is the T-R separation distance at time t. The RX velocity vector is equal to the derivative of $\mathbf{r}_{RX}(t)$, which is given by [76]

$$\mathbf{v} = \begin{bmatrix} v_x \\ v_y \\ v_z \end{bmatrix} = \frac{d\mathbf{r}_{RX}(t)}{dt} = \frac{d \begin{bmatrix} r(t)\sin(\theta_{\text{ZOD}}(t))\cos(\phi_{\text{AOD}}(t)) \\ r(t)\sin(\theta_{\text{ZOD}}(t))\sin(\phi_{\text{AOD}}(t)) \\ r(t)\cos(\theta_{\text{ZOD}}(t)) \end{bmatrix}}{dt}, \tag{3.16}$$

$$\begin{bmatrix} v_x \\ v_y \\ v_z \end{bmatrix} = \begin{bmatrix} \sin(\theta_{\text{ZOD}})\cos(\phi_{\text{AOD}}) & r\cos(\theta_{\text{ZOD}})\cos(\phi_{\text{AOD}}) & -r\sin(\theta_{\text{ZOD}})\sin(\phi_{\text{AOD}}) \\ \sin(\theta_{\text{ZOD}})\sin(\phi_{\text{AOD}}) & r\cos(\theta_{\text{ZOD}})\sin(\phi_{\text{AOD}}) & r\sin(\theta_{\text{ZOD}})\cos(\phi_{\text{AOD}}) \\ \cos(\theta_{\text{ZOD}}) & -r\sin(\theta_{\text{ZOD}}) & 0 \end{bmatrix} \cdot \begin{bmatrix} \dot{r} \\ \dot{\theta}_{\text{ZOD}} \\ \dot{\phi}_{\text{AOD}} \end{bmatrix} \tag{3.17}$$

By calculating the inverse of the above matrix [76],

$$\begin{bmatrix} \dot{r} \\ \dot{\theta}_{\text{ZOD}} \\ \dot{\phi}_{\text{AOD}} \end{bmatrix} = \begin{bmatrix} \cos(\phi_{\text{AOD}})\sin(\theta_{\text{ZOD}}) & \sin(\phi_{\text{AOD}})\sin(\theta_{\text{ZOD}}) & \cos(\theta_{\text{ZOD}}) \\ \cos(\phi_{\text{AOD}})\cos(\theta_{\text{ZOD}})/r & \sin(\phi_{\text{AOD}})\cos(\theta_{\text{ZOD}})/r & -\sin(\theta_{\text{ZOD}})/r \\ -\sin(\phi_{\text{AOD}})/(r\sin(\theta_{\text{ZOD}})) & \cos(\phi_{\text{AOD}})/(r\sin(\theta_{\text{ZOD}})) & 0 \end{bmatrix} \cdot \begin{bmatrix} v_x \\ v_y \\ v_z \end{bmatrix}, \tag{3.18}$$

where $\dot{\theta}_{\text{ZOD}}$ and $\dot{\phi}_{\text{AOD}}$ are S_{ZOD} and S_{AOD}. Linear changing rates for four angles for a LOS component are given by [76]

$$S_{\text{AOD}} = \frac{v_y \cos(\phi_{\text{AOD}}) - v_x \sin(\phi_{\text{AOD}})}{r \sin(\theta_{\text{ZOD}})}$$

$$S_{\text{ZOD}} = \frac{v_x \cos(\phi_{\text{AOD}}) \cos(\theta_{\text{ZOD}}) + v_y \cos(\theta_{\text{ZOD}}) \sin(\phi_{\text{AOD}}) - v_z \sin(\theta_{\text{ZOD}})}{r}$$

$$S_{\text{AOA}} = \frac{v_y \cos(\phi_{\text{AOA}}) - v_x \sin(\phi_{\text{AOA}})}{r \sin(\theta_{\text{ZOA}})}$$

$$S_{\text{ZOA}} = \frac{v_x \cos(\phi_{\text{AOA}}) \cos(\theta_{\text{ZOA}}) + v_y \cos(\theta_{\text{ZOA}}) \sin(\phi_{\text{AOA}}) - v_z \sin(\theta_{\text{ZOA}})}{r}$$

$$(3.19)$$
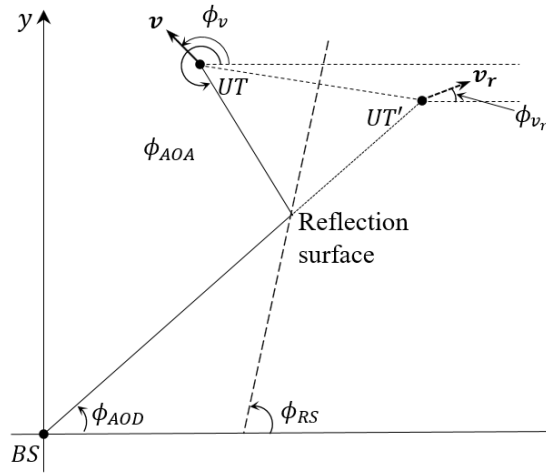
FIGURE 3.10: UT movement and change of AOD in the azimuth plane in NLOS scenarios. The mirror images of the UT location and velocity direction ϕ_v are shown as UT' and ϕ_{v_r}

NLOS case: For NLOS components, there is no direct path between TX and RX. MPCs are reflected, diffracted, or scattered at least once. A multiple reflection surfaces method is first proposed here to update angles of NLOS components, which is motivated by a simple case from [74], where the MPC is only reflected once before it reaches the UT. By obtaining the relation between the actual UT location and the mirror image of the actual UT location, the mirror image of the UT velocity vector can be calculated using the image theory. Then, the NLOS component is transformed to a virtual LOS component, and the angles of NLOS components can be updated using the update equations for the LOS component. More details are explained below.

An illustration of the single reflection of a NLOS MPC is shown in Fig. 3.10. The reflection surface is assumed to be perpendicular to the azimuth plane and has a reflection surface angle, ϕ_{RS} [74]. ϕ_{RS} is within $[0,\pi]$. The mirror image of the UT location and the UT velocity vector with respect to the reflection surface is also shown in Fig. 3.10. From the view of BS, UT is equivalent to moving at the velocity of v_r at the location UT'. Note that UT' is in the LOS condition from the BS. Thus, angles can be updated using equations for the LOS component with assuming that UT' moves at

the velocity of v_r. Then, ϕ_{v_r} and ϕ_{AOA} are given by

$$\phi_{\text{AOA}} = 2\phi_{RS} + \pi - \phi_{\text{AOD}}$$
$$\phi_{v_r} = 2\phi_{RS} - \phi_v$$

(3.20)
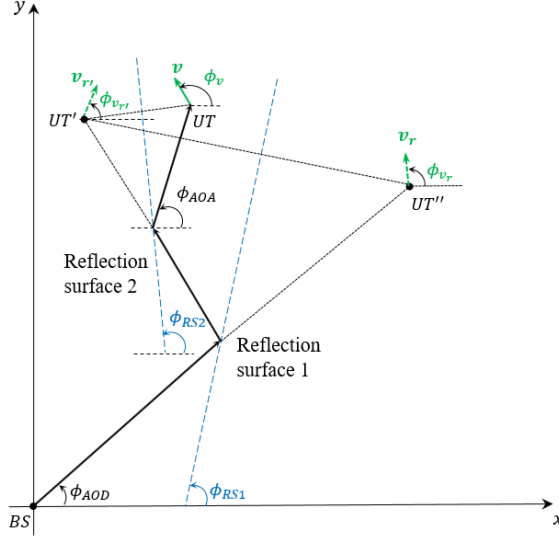
FIGURE 3.11: UT movement and change of AOD in the azimuth plane in NLOS scenarios.

Then, we consider that a NLOS MPC is reflected twice before it reaches the UT, which is illustrated in Fig. 3.11, ϕ_{v_r} and ϕ_{AOA} are given by

$$\phi_{\text{AOA}} = 2\phi_{RS2} - 2\phi_{RS} + \phi_{\text{AOD}} = \Delta_{RS} + \phi_{\text{AOD}}$$
$$\phi_{vr} = 2\phi_{RS2} - 2\phi_{RS} + \phi_v = \Delta_{RS} + \phi_v$$

(3.21)

where ϕ_{RS1} and ϕ_{RS2} are the angles of the first and second reflection surfaces with respect to the x axis. Further, a general relation with M reflection surfaces between ϕ_{AOA} and ϕ_{AOD}, and between ϕ_{vr} and ϕ_v can be given by

$$\phi_{\text{AOA}} = (-1)^M \phi_{\text{AOD}} + 2\sum_{i=1}^{M}(-1)^i\phi_{RSi} + M\pi = \Delta_{RS} + (-1)^M\phi_{\text{AOD}} + M\pi$$

$$\phi_{vr} = (-1)^M \phi_v + 2\sum_{i=1}^{M}(-1)^i\phi_{RSi} = \Delta_{RS} + (-1)^M\phi_v$$

(3.22)

where ϕ_{RSi} is the angle of the ith reflection surface with respect to the x axis, where the reflection surfaces are assumed to be perpendicular to the x-y plane (ground). It can be seen from (3.22) that there are possibilities of the relation between ϕ_{AOD} and ϕ_{AOA}. Same is the relation between ϕ_r and ϕ_{vr}, which depends on the number of reflection surfaces a NLOS MPC goes through. If it is an odd number of reflection surfaces, (3.20) is applied; if it is an even number of reflection surfaces, (3.21) is applied. Since ϕ_{AOD} and ϕ_{AOA} are known, ϕ_{vr} can be calculated based on Δ_{RS} and ϕ_v. Using ϕ_{vr} instead of ϕ_v, the changing relation for four angles for NLOS component

are given by

$$S_{\text{AOD}} = B \cdot S_{\text{AOA}}$$
$$S_{\text{ZOD}} = -S_{\text{ZOA}}$$

(3.23)

where B can be -1 (even reflections)or 1 (odd reflections) with 50 % and 50 % probability, which indicates that the probabilities that a NLOS MPC experiences an odd or an even number of MPCs are assumed to be equal. Finally, the update equations for AOD, ZOD, AOA, and ZOA are summarized as

$$\phi_{\text{angle}}(t_k) = \phi_{\text{angle}}(t_{k-1}) + S_{\text{angle}}(t_k - t_{k-1}),$$

(3.24)

where S_{angle} for a LOS component are given by

$$S_{\text{AOD}} = \frac{v_y \cos(\phi_{\text{AOD}}) - v_x \sin(\phi_{\text{AOD}})}{r \sin(\theta_{\text{ZOD}})}$$

$$S_{\text{ZOD}} = \frac{v_x \cos(\phi_{\text{AOD}}) \cos(\theta_{\text{ZOD}}) + v_y \cos(\theta_{\text{ZOD}}) \sin(\phi_{\text{AOD}}) - v_z \sin(\theta_{\text{ZOD}})}{r}$$

$$S_{\text{AOA}} = \frac{v_y \cos(\phi_{\text{AOA}}) - v_x \sin(\phi_{\text{AOA}})}{r \sin(\theta_{\text{ZOA}})}$$

$$S_{\text{ZOA}} = \frac{v_x \cos(\phi_{\text{AOA}}) \cos(\theta_{\text{ZOA}}) + v_y \cos(\theta_{\text{ZOA}}) \sin(\phi_{\text{AOA}}) - v_z \sin(\theta_{\text{ZOA}})}{r},$$

(3.25)

and S_{angle} for NLOS components are given by

$$S_{\text{AOD}} = \frac{v_{r,y} \cos(\phi_{\text{AOD}}) - v_{r,x} \sin(\phi_{\text{AOD}})}{l \sin(\theta_{\text{ZOD}})}$$

$$S_{\text{ZOD}} = \frac{v_{r,x} \cos(\phi_{\text{AOD}}) \cos(\theta_{\text{ZOD}}) + v_{r,y} \cos(\theta_{\text{ZOD}}) \sin(\phi_{\text{AOD}}) - v_{r,z} \sin(\theta_{\text{ZOD}})}{l}$$

$$S_{\text{AOA}} = B \frac{v_{r,y} \cos(\phi_{\text{AOA}}) - v_{r,x} \sin(\phi_{\text{AOA}})}{l \sin(\theta_{\text{ZOA}})}$$

$$S_{\text{ZOA}} = \frac{v_{r,x} \cos(\phi_{\text{AOA}}) \cos(\theta_{\text{ZOA}}) + v_{r,y} \cos(\theta_{\text{ZOA}}) \sin(\phi_{\text{AOA}}) - v_{v,z} \sin(\theta_{\text{ZOA}})}{l},$$

(3.26)

Note that r is the T-R separation distance while l is the actual path length for a certain NLOS component, as shown in Fig. 3.10 and Fig. 3.11. It is impossible to acquire the actual path length using geometry without deterministic reflection surface information. Thus, the path length is calculated by multiplying the absolute time delay generated from the NYUSIM channel model with the speed of light.

Delay, Power, and Phase Update: The update of the delay of each MPC uses reflection surfaces based on geometry. Basically, the change of the delay is the change of the path length divided by the speed of light, as shown in Fig. 3.12. Using law of cosines, the update of the delay can be given by

$$\tau(t) = \tau(t_0) + \frac{\Delta l}{c}$$
$$\tau(t) = \sqrt{(v\Delta t)^2 + (c\tau(t_0))^2 - 2v(\Delta t) \cdot c\tau(t_0) \cdot \cos(\phi_v - \phi_{\text{AOA}})}$$

(3.27)
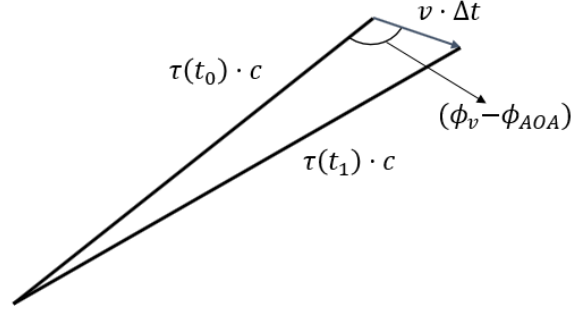
FIGURE 3.12: Update of delay and phase based on the change of path length in time interval Δt. $\tau(t_0)$, ϕ_v, and ϕ_{AOA} are known, $\tau(t_1)$ can be calculated using the law of cosine.

where Δl is the change of the path length, and Δt is the update time. $\tau(t)$ is the absolute time delay at time t. ϕ_v is the UT moving direction in azimuth plane, and ϕ_{AOA} is the AOA of a MPC received at the UT.

Similarly, the update of the phase of each MPC is also based on the change of the path length. The update of the phase can be given by

$$\varphi(t) = \varphi(t_0) + \Delta l \cdot k = \varphi(t_0) + \frac{2\pi\Delta l}{\lambda} \tag{3.28}$$

where Δl is the change of the path length given in (3.27). k is the wavenumber depending on the wavelength, $k = 2\pi/\lambda$. Note that the initial phase generation of MPCs is assumed to be i.i.d, and uniform between 0 and 2π since each MPC experiences a different scattering environment, thus arriving at arbitrary AOA spatial lobe. However, the update of the phase should add the phase change to the initialized phase, but is not generated randomly again.

The update of the power of each MPC is based on the updated delay information. Using the same generation procedure for cluster powers and cluster subpath powers in [25], the powers of MPCs are re-distributed based on the updated delay. Generation of cluster powers P_n (mW) is given by [25]

$$
\begin{aligned}
P_n' &= \bar{P}_0 e^{-\frac{\tau_n}{\Gamma}} 10^{\frac{Z_n}{10}} \\
P_n &= \frac{P_n'}{\sum_{i=1}^{N} P_i'} \times P_r [mW] \\
Z_n &\sim N(0, \sigma_Z)
\end{aligned}
\tag{3.29}
$$

where $\bar{P}_0$ is the average power in the first arriving MPC, Γ is the cluster decay time constant, and Z_n is a lognormal random variable with 0 dB mean and STD σ_Z. N is the number of time clusters. The actual cluster powers P_n are calculated by ensuring the sum of P_n to be equal to the total received power P_r. Generation of subpath powers $\Pi_{m,n}$ in each cluster is given by

[25]

$$\Pi'_{m,n} = \bar{\bar{\Pi}}_0 e^{-\frac{\rho_{m,n}}{\gamma}} 10^{\frac{U_{m,n}}{10}}$$

$$\Pi_{m,n} = \frac{\Pi'_{m,n}}{\sum_{j=1}^{M_n} \Pi'_{j,n}} \times P_n [mW] \qquad (3.30)$$

$$U_{m,n} \sim N(0, \sigma_U)$$

where $\bar{\bar{\Pi}}_0$ is the average power in the first received intra-cluster subpath, γ is the subpath delay time constant, and $U_{m,n}$ is a lognormal random variable with 0 dB mean and STD σ_U. M_n is the number of subpaths in the nth cluster.

In a word, the cluster powers are modeled as an exponential function over time excess delay. The cluster subpath powers in each cluster are also modeled as an exponential function over intra-cluster time excess delay [25]. By re-distributing cluster powers and subpath powers, the channel model with spatial consistency can model the power variation along the UT movement. Considering the cluster powers and subpath powers still follow exponential decay, the power of each MPC will not change drastically within the update distance (e.g. 10 m), which matches the observations in [15].

The update procedure for SSPs of each MPC which are angles, delay, power, phase is described above. A geometry-based approach using reflection surfaces is applied to update time-variant angles (AOA, AOD, ZOA, ZOD). The delay and phase is updated based on the change of path length, which is calculated using reflection surfaces. Cluster powers are re-distributed using the total received power with respect to the time excess delay of clusters, and cluster subpath powers are re-distributed using cluster powers with respect to the intra-cluster time excess delay of subpaths.

LSPs and SSPs have been continuously updated in each channel segment, while the initial channel coefficients of channel segments are independently generated. Therefore, a smooth transition procedure is applied to "connect" channel segment by cluster birth and death. The power of one old cluster ramps down and one new cluster ramps up [77]. Since the number of time clusters in two channel segments may be different, the power of one cluster can ramp up or down individually. Note that cluster birth and death only happen to one time cluster in a channel snapshot.

3.7 Outdoor to Indoor Penetration Loss Model

A simple parabolic model was first proposed in [50], which fits the measured building penetration loss with standard glass and IRR glass. The parabolic model is given by [51]

$$\text{BPL[dB]} = 10\log_{10}(A + B \cdot f_c^2) + N(0, \sigma_P^2) \qquad (3.31)$$

where f_c is the carrier frequency. $A = 5$, $B = 0.03$, and $\sigma_P = 4.0$ for low-loss buildings (with standard glass). $A = 10$, $B = 5$, and $\sigma_P = 6.0$ for high-loss buildings(with IRR glass). Most O2I penetration loss measurements set the incident angle as 0 degree (perpendicular to the building wall). However,

the losses have been observed to increase by up to 15 to 20 dB as the incidence angle becomes more larger (parallel to the building wall).

3.8 Human Blockage Shadowing Loss Model

Measurement-based two-state and four-state Markov models for human blockage shadowing loss were proposed in [78]. The human blockage measurements were conducted by precious researchers at NYU WIRELESS in an open square in downtown Brooklyn. Measurements captured the effects of large moving crowds in an urban setting for a peer-to-peer communication links at mmWave (73 GHz) [78]. Three types of horn antennas were used to study the effects of antenna beamwidth on the blockage event. The antenna gain and azimuth and elevation half power beamwidth (HPBW) are given in Table. 3.5. TX and RX antennas were boresight-aligned and remained fixed during the measurements. In an observation window of 135 s, people crossed the LOS link, and 40,800 PDP snapshots were recorded with a 3.3 ms time separation between two consecutive PDPs. Details of the measurement setup and hardware specifications are provided in [78]. A 135 s long time-variant received power trace was obtained with 135 s long, which was then used to determine the probability of blockage occurrences and the statistics of the shadowing loss of each blockage event. Note that aforementioned human blockage measurements are on peer-to-peer level, and are not representative of a BS-UT setting. However, T-R separation distances were usually taken to be greater than 40 m, BSs were on the horizon and thus were at similar heights relative to the UT. Thus, it is reasonable to extend blockage statistics obtained from peer-to-peer measurements to the BS-UT setting. The knife edge diffraction (KED) model is another method of modeling the blockage effect, which is not implemented in NYUSIM [79].

TABLE 3.5: ANTENNA SPECIFICATIONS IN THE URBAN ENVIRONMENT MEASUREMENTS [80]

Antenna Index	Antenna 1	Antenna 2	Antenna 3
TX&RX Antenna Gain	27 dBi	20 dBi	9.1 dBi
TX&RX Az./El. HPBW	7°/7°	15°/15°	60°/60°

A simple two-state Markov model can be used to characterize shadowed and unshadowed states for a communication link in the presence of pedestrian induced variations in the received signal strength [80]. A better four-state piece wise linear approach can also be used to characterize blockage with the following states: unshadowed, shadowed, a decaying period from unshadowed to shadowed, and a rising period from shadowed to unshadowed, which is given by [78], [81]

$$SE(t) = \begin{cases} r_{\text{decay}} \cdot t, & \text{for } 0 \leq t \leq \frac{SE_{\text{mean}}}{r_{\text{decay}}} \\ SE_{\text{mean}}, & \text{for } \frac{SE_{\text{mean}}}{r_{\text{decay}}} \leq t \leq t_D - \frac{SE_{\text{mean}}}{r_{\text{rise}}} \\ SE_{\text{mean}} - r_{\text{rise}} \cdot t, & \text{for } t_D - \frac{SE_{\text{mean}}}{r_{\text{rise}}} \leq t \leq t_D \\ 0, & \text{otherwise} \end{cases} \quad (3.32)$$

where SE_{mean} is the mean attenuation (in dB) of a blockage event, which is calculated over the interval $[\frac{1}{3}t_D, \frac{2}{3}t_D]$. t_D is the blockage event time duration in ms, which is the time interval between the between the last zero-crossing before and the first zero-crossing after the rapid signal fade. r_{decay} is the decay rate of the signal strength in dB/ms, which is the slope of the line segment between the last zero-crossing before the rapid fading and the first SE_{mean}-crossing in the rapid fading. r_{rise} is the rising rate of the signal strength in dB/ms, which is the slope of the line segment between the first zero-crossing after the rapid fading and the last SE_{mean}-crossing in the rapid fading.

Base on the piece wise function in (3.32), a four-state Markov model corresponding to four stages was proposed to characterize blockage events [80], [82]. The corresponding transition matrix is shown in Fig. 3.13 [78] and is given by

$$\begin{bmatrix} 1 - p_{\text{decay}} & p_{\text{decay}} & 0 & 0 \\ 0 & 1 - p_{\text{shad}} & p_{\text{shad}} & 0 \\ 0 & 0 & 1 - p_{\text{rise}} & p_{\text{rise}} \\ p_{\text{unshad}} & 0 & 0 & 1 - p_{\text{unshad}} \end{bmatrix} \tag{3.33}$$
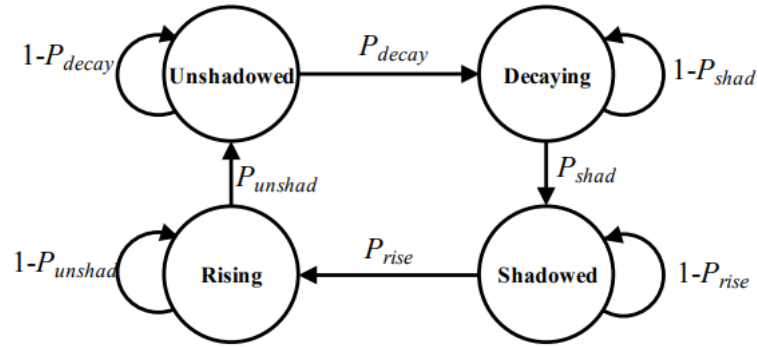
FIGURE 3.13: Four-state Markov model for unshadowed, decaying, shadowed, and rising states for modeling blockage events [78].

Using the four-state Markov model, transition rates with three antenna settings (7°, 15°, 60°) are calculated based on measurements and given in Table V in [78]. While the work in [80] offers values for the Markov model for three different antenna beamwidths, more measurements with different beamwidths and different shadowing scenarios will be needed to more accurately parameterize the four-state Markov model for various applications that may emerge in the future. For this reason, NYUSIM offers both a default setting as a linear fit of different beamwidths based on [78], but also allows the user to input different Markov model parameters for different human shadowing models that may be developed from future measurements. The simple linear fit of transition rates with respect to the RX antenna azimuth HPBW in degrees is adopted in the NYUSIM channel model

and given by

$$
\begin{aligned}
\lambda_{\text{decay}} &= 0.2 \\
\lambda_{\text{shad}} &= 0.065 * \text{HPBW}(°) + 7.425 \\
\lambda_{\text{rise}} &= 0.05 * \text{HPBW}(°) + 7.35 \\
\lambda_{\text{unshad}} &= 6.7
\end{aligned}
\tag{3.34}
$$

λ is the transition rate from one state to the next state. The transition probability $p = \lambda \cdot t$, and t is the time resolution, which is set to be 1 ms in NYUSIM. Using this four-state Markov model given transition rates, a arbitrarily long Markov trace (20 s used in NYUSIM) is generated with time resolution 1 ms, which has 20,000 points in total. Each point on the trace is assigned a state (unshadowed, shadowed, decay, or rise). The blockage fade duration, decay time, and rising time are determined. The attenuation of all the points in the shadowed state are the same (SE_{mean}). The attenuation of the points in the decay state is decreasing from 0 to SE_{mean} linearly, and the attenuation of the points in the rising state is increasing from SE_{mean} to 0 in a linear manner.

Note that the mean attenuation of a blockage event (SE_{mean}) is still unknown. SE_{mean} is modeled as a log-normal random variable with the average mean attenuation μ_A and the variance σ_A. The average mean attenuation μ_A depends on the RX antenna azimuth HPBW in degrees, and a simple analytical expression is given in [78]:

$$
\mu_A[dB] = 10\log_{10}\left(b + \frac{180}{\text{HPBW}(°)}\right)
\tag{3.35}
$$

where b is a constant, and HPBW is the RX antenna azimuth HPBW in degrees, which can be from 1° to 180°. In NYUSIM, $b = 9.8$ and $\sigma_A = 0.31$ are obtained by curve fitting the measured data with three antenna settings. For different antenna settings, σ_A is always assumed to be 0.31, which can be characterized by a better model based on more measurements in the future. Admittedly, the measurements are limited and may not provide a accurate relation between the transition rate and mean attenuation and antenna beamwidth. More measurements with different antenna settings are required to accurately parameterize the four-state Markov model.

NYUSIM can generate omnidirectional and directional channels, for either a drop realization in the drop-based mode or a channel snapshot in the spatial consistency mode. For omnidirectional channels generated from NYUSIM, antenna HPBW is not applicable, the spatial lobe width, instead, is used to calculate transition rates and mean attenuation. Spatial lobes represent main directions of arrival (or departure) where energy may arrive over several hundreds of nanoseconds. A spatial lobe is modeled as a Gaussian distribution, with a variance equal to the lobe angular spread. The largest value of lobe angular spread obtained from measurements was 11.5° in a LOS scenario [25]. The typical width of a spatial lobe is less than 11.5°×6 = 69° with 99.7% probability, which is close to the 60° HPBW antenna used in the measurements [80]. Thus, it is valid to assume that all MPCs in this spatial lobe will experience the same amount of shadowing loss when a blockage event happens in the direction within the range of a spatial lobe. Based on field measurements, the number of main directions

of arrival (AOA spatial lobes n_{AOA}) and the number of main directions of departure (AOD spatial lobes n_{AOD}) are between 1 and 5. The generated MPCs are randomly assigned to both an AOA and an AOD spatial lobes. In other words, MPCs in an AOD spatial lobe may belong to different AOA spatial lobes, and vice versa. Thus, there are $n_{\text{AOA}} \cdot n_{\text{AOD}}$ lobe combinations in the channel. For each lobe combination, the human blockage is generated independently.

In addition, a directional channel realization output from NYUSIM is generated by applying the user-specified antenna pattern in the strongest MPC direction to the omnidirectional channel realization. The applied antenna pattern emulates the horn antenna pattern used in the mmWave field measurements [48], and can be calculated by the user-specified antenna azimuth and elevation HPBW. For directional channels generated from NYUSIM, a blockage event will only induce the same shadowing loss to the MPCs within the RX antenna HPBW.

3GPP 38.901 proposed 5 potential independent blockers for each path [70]. In NYUSIM, it is assumed that m independent blockage events (uniformly distributed between 1 and 5) may occur for each spatial lobe. m independent blockage events correspond to m independent Markov traces. m Markov traces are superimposed to obtain a total loss trace. The actual shadowing loss for a spatial lobe is attained by randomly selecting a time instance t_0 over the total loss trace. An example of 5 independent Markov traces running the drop-based mode in NYUSIM is shown in Fig. 3.14.
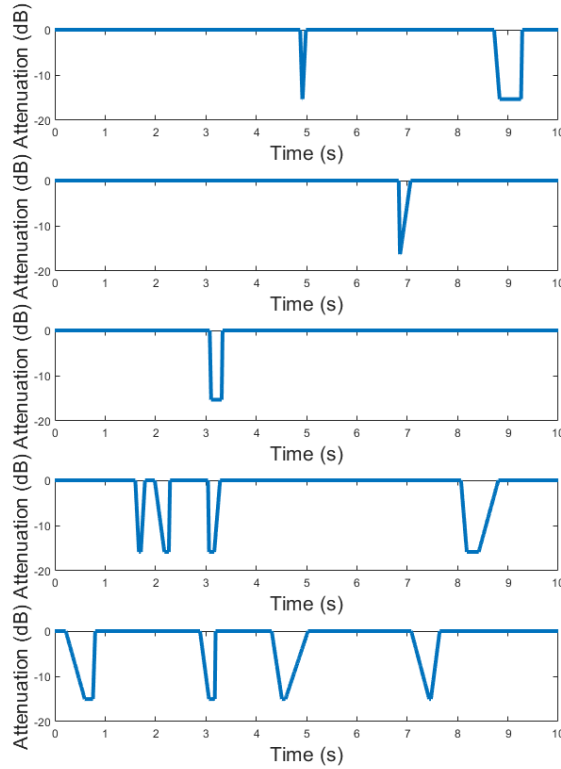

FIGURE 3.14: Five independently simulated Markov traces.

51

3.9   Polarization Model

Dual-polarized transmitter and receiver antenna arrays have become a standard setup for mmWave wireless systems in 5G to deliver more signal energy and increase channel rank for higher-order MIMO diversity and multiplexing. Correspondingly, the channel simulators are expected to generate different polarization combinations for a single channel realization at the same time. Therefore, NYUSIM 3.1 enables simultaneous multiple polarization realizations for channel simulations from 500 MHz to 150 GHz in indoor and outdoor environments. The adopted model for polarization is described as follows.

Cross-polarization discrimination (XPD) is defined as the signal power attenuation (in dB) when the transmit antenna is vertically polarized and the receive antenna horizontally polarized (i.e., cross-polarization) compared to the case that both transmit and receive antennas are vertically or horizontally polarized (i.e., co-polarization) including channel effect. XPD values over microwave and millimeter-wave frequencies at various indoor and outdoor environments have been reported in the literature [2], [7], [18], [29]–[37], showing that the XPD increases as the carrier frequency increases. Thus, a linear function of frequency is used to fit the reported XPDs and calculate the XPD over the NYUSIM supported frequency range (500 MHz to 150 GHz), which is given by

$$\text{XPD (dB)} = k \cdot f \, (\text{GHz}) + b, \tag{3.36}$$

where k and b are the slope and intercept, respectively. In addition, the XPDs are found larger in LOS environments than those in NLOS environments since the boresight path generally does not have a depolarization effect. Two linear functions with different values are used for the LOS and NLOS environments. Here we apply a single XPD to the total omnidirectional received power instead of applying different XPDs to different multipath components (MPCs) due to the limited available MPC-wise XPD values in the literature, which makes the polarization model succinct yet valid. The used XPD values and linear fits for the LOS and NLOS environments are shown in Fig. 3.15.
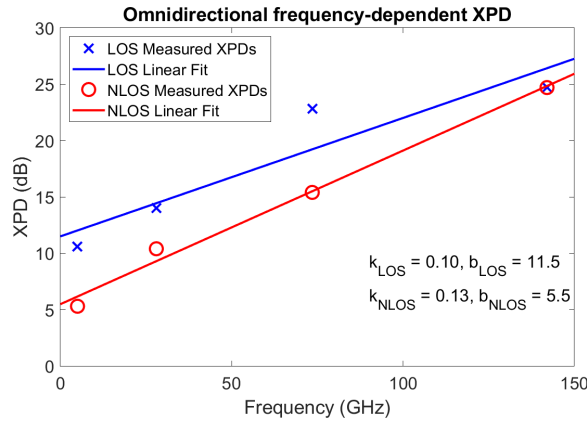
FIGURE 3.15: The measured XPDs with linear fits for the LOS and NLOS environments.

Similarly, co-polarization discrimination (CPD) can be defined as the

52

power difference (in dB) between the V-V and H-H polarization settings or the V-H and H-V polarization settings. The studies on the CPD are very limited [29], [33], [38], [39], showing that the V-V polarization usually has a slightly larger received power than the H-H polarization when walls are the primary reflectors in the environment. However, the difference in the overall received power is typically negligible (within 1 dB) [29], [33], [38], [39]. One exception is the tunnel scenario, where the particular confined waveguide shape causes the CPD variation between -20 dB and 80 dB with a mean of 5.4 dB [38]. NYUSIM focuses on the common indoor and outdoor environments. Thus the CPD is modeled as a zero-mean Gaussian random variable with a small standard deviation (1.6 dB used in NYUSIM 3.1) [29], [33], [38].

NYUSIM 3.1 allows users to use one polarization (co- or cross-polarization), two polarizations (co- and cross-polarization), or four polarizations (vertical-to-vertical (V-V), horizontal-to-horizontal (H-H), vertical-to-horizontal (V-H), and horizontal-to-vertical (H-V) polarizations) for every single channel realization. The output figures and files are named with the specified polarization.

4. Applications of NYUSIM

The output figure and data files generated from NYUSIM can be used in various ways based on users' needs, e.g., to simulate channel impulse responses for mmWave systems, to investigate MIMO performance, etc. Here we present five example applications for how NYUSIM may be used.

4.1 Application 1: MIMO Channel Condition Number

First we show an example of how to obtain the condition number of a MIMO channel by making use of the output data files "BasicParameters.mat" and "DirPDPInfo.mat", assuming OFDM modulation is utilized. This application also shows the wide range of parameters that a user may adjust in NYUSIM2.01.

The condition number is defined as the ratio of the largest to smallest singular value in the singular value decomposition of a matrix, and is a metric to characterize the quality of MIMO channels in the context of wireless communications [63], [83]–[85]. The condition number will be high (e.g., over 20 dB) if the minimum singular value is close to zero, and will be 0 dB if singular values are equal. Physically, a small condition number value (e.g., below 20 dB) indicates good orthogonality of different sub-channels (a sub-channel usually has a distinct spatial direction), and the channel gains are comparable in different spatial directions. The rank of a matrix is the dimension of the vector space generated (or spanned) by its columns (or rows) [86], and it determines how many data streams can be multiplexed over the channel in the context of MIMO communications [83], [87], [88]. The condition number is related to the rank of a matrix: a low condition number usually corresponds to a high rank and vice versa; the matrix has full rank (the highest rank) when the condition number is equal or close to 0 dB (the lowest theoretical condition number).

Let's look at the condition number of a MIMO channel matrix for a single sub-carrier in an OFDM system. As described in Section 2.2.2, the output data files "BasicParameters.mat" and "DirPDPInfo.mat" contain paramount parameters of each resolvable multipath component, which will be useful in generating the MIMO channel coefficient for an OFDM sub-carrier. Take ULAs at both the transmitter and receiver for example, the equation for generating such a channel coefficient is provided below, which is adapted

from Eq.(2) in [89]:

$$h_{m,k}(f) = \sum_p \alpha_{m,k,p} e^{j\Phi_{m,k,p}} e^{-j2\pi f\tau_{m,k,p}} e^{-j2\pi d_T m \sin(\phi_{m,k,p})} e^{-j2\pi d_R k \sin(\varphi_{m,k,p})}$$

(4.1)

where $h_{m,k}(f)$ denotes the MIMO channel coefficient between the mth transmit antenna and the kth receive antenna for the sub-carrier f, p represents the pth resolvable multipath component, α is the amplitude of the channel gain, Φ denotes the phase of the multipath component, τ represents the time delay, d_T and d_R are the antenna element spacing at the transmitter and receiver, respectively, while ϕ and φ denote the azimuth angle of departure and angle of arrival, respectively. All of the above parameters can be extracted from the files "BasicParameters.mat" and "DirPDPInfo.mat". For each sub-carrier f in a MIMO-OFDM system, there exists an $N_t \times N_r$ channel matrix H whose elements are $h_{m,k}(f)$, where $m = 1, ..., N_t$ and $k = 1, ..., N_r$. The condition number of H can be obtained consequently.

Using the above mentioned approach, and the input parameters on the NYUSIM GUI with the following values:

- Distance Range Option: Standard (10-500 m)

- Frequency: 28 GHz

- RF bandwidth: 800 MHz

- Scenario: UMi

- Environment: LOS

- Lower Bound of T-R Separation Distance: 100 m

- Upper Bound of T-R Separation Distance: 100 m

- TX Power: 30 dBm

- Base Station Height: 35 m (This parameter is ignored by the program because it is the UMi scenario, and not the RMa scenario.)

- Barometric Pressure: 1013.25 mbar

- Humidity: 50%

- Temperature: 20°C

- Rain Rate: 0 mm/hr

- Polarization: Co-Pol

- Foliage Loss: No

- Number of RX Locations: 100

- TX Array Type: ULA

- RX Array Type: ULA

- Number of TX Antenna Elements N_t: 2

- Number of RX Antenna Elements N_r: 2

- TX Antenna Spacing: 0.5 wavelength

- RX Antenna Spacing: 0.5 wavelength

- Number of TX Antenna Elements Per Row W_t: 2

- Number of RX Antenna Elements Per Row W_r: 2

- TX Antenna Azimuth HPBW: $10°$

- TX Antenna Elevation HPBW: $10°$

- RX Antenna Azimuth HPBW: $10°$

- RX Antenna Elevation HPBW: $10°$

and assuming the frequency interval between adjacent sub-carriers is 500 kHz, which corresponds to 800 MHz/500 kHz = 1600 sub-carriers, we perform 100 simulation runs (i.e., set the number of RX locations to 100) to emulate 100 random MIMO channel realizations with the input parameters described above. Then the following changes are made to the four input parameters below with all the other input parameter values remaining the same:

- Number of TX Antenna Elements N_t: 3

- Number of RX Antenna Elements N_r: 3

- Number of TX Antenna Elements Per Row W_t: 3

- Number of RX Antenna Elements Per Row W_r: 3

Fig. 4.1 illustrates the empirical CDF of the condition number of channel matrices for OFDM sub-carriers with the above two sets of input parameters in one of the 100 simulation runs. The empirical CDF of the corresponding rank of the channel matrices are plotted in Fig. 4.2, where the rank here is defined as the number of singular values of the channel matrix that are larger than $\sigma_m/1000$, where σ_m is the maximum singular value of the channel matrix. By this definition of rank, we are essentially ignoring the singular values that are 30 dB smaller than the maximum singular value, which is physically reasonable since the singular value is a measure of the channel gain along its corresponding singular vector and it makes little sense to consider the direction with an extremely small channel gain. It is apparent from Fig. 4.1 that the condition numbers of the individual OFDM sub-carriers for a 3×3 MIMO channel is about 18 dB larger compared to the 2×2 case on average, and the relatively large condition number of the 3×3 channel matrix may stem from the fact that the matrix is rank deficient, as evident from Fig. 4.2, in which about 96% of the channel matrices have a rank of 2 instead of 3 (full rank).

Based on the results from the 100 random simulation runs, it is found that the average median value of the condition numbers of the channel matrices for individual sub-carriers over the 100 simulation runs is around 13 dB (i.e., the difference in dB between the largest and smallest singular value of

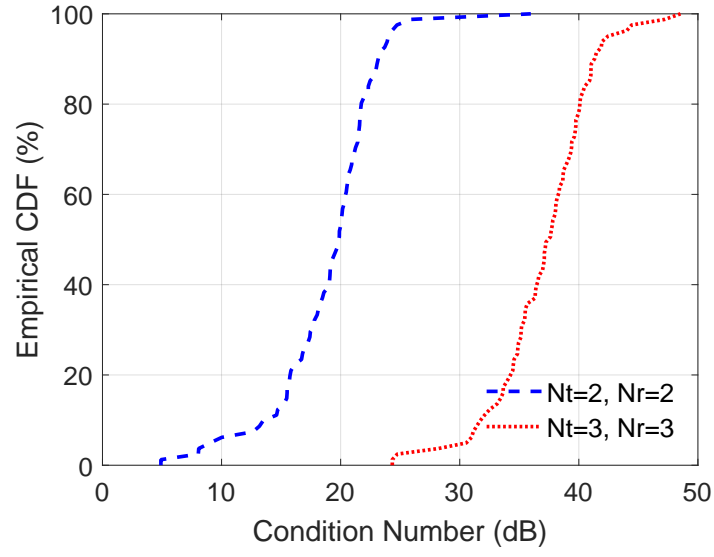FIGURE 4.1: Empirical CDF of the condition number of channel matrices for OFDM sub-carriers with different transmit and receive antenna elements N_t and N_r for MIMO-OFDM channels in one simulation run.
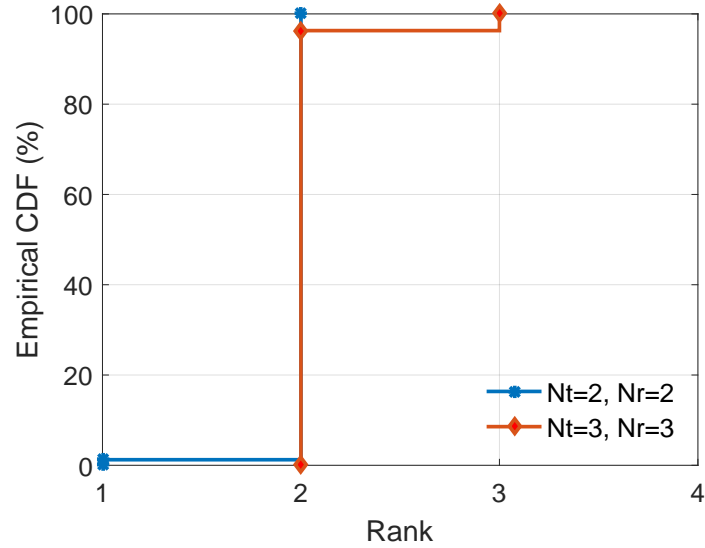

FIGURE 4.2: Empirical CDF of the rank of channel matrices for OFDM sub-carriers with different transmit and receive antenna elements N_t and N_r for MIMO-OFDM channels in one simulation run.

the channel matrix is 13 dB), and the average matrix rank is 2. When the numbers of TX and RX antenna elements are both changed to 3, the average median value of the condition number increase to 31 dB, with a mean rank of roughly 2, indicating that two spatial streams can be sent simultaneously using the spatial multiplexing technique in this case.

The Matlab code for extracting channel coefficients based on Eq. (4.1), generating the channel matrix for each sub-carrier frequency, and calculating the condition number and rank in the example above is contained in the package named "Application Example Code" available on the NYUSIM downloading website.

4.2 Application 2: Spectral Efficiency Comparison Between 3GPP and NYUSIM Channel Models

As mentioned in NYUSIM Overview on Page ii of this user manual, the 3GPP TR 38.900 Release 14 channel model [64] contains unrealistic number of clusters (e.g., 19 clusters for UMi NLOS) and up to 20 rays per cluster, which is excessively large and not borne out by measurements, and is likely to result in incorrect predictions on MIMO system performance such as spectral efficiency (SE). in this subsection, we use the 3GPP TR 38.900 Release 14 channel model [64] and NYUSIM channel model to analyze and compare the spectral efficiency for mmWave MIMO channels.

Let us assume a single-cell single-user MIMO system without multiple-access interference, operating at 28 GHz with an RF bandwidth of 100 MHz in the UMi scenario. The base station (BS) is equipped with 256 antenna elements comprising a uniform rectangular array (URA) with cross-polarized elements, which can reduce the hardware size and make better use of multipath components with different polarizations since the cross-polarization discrimination ratio is 8-9 dB in both models, where the antenna pattern on Page 23 of [64] is adopted. The user equipment (UE) has 16 antenna elements constituting a URA with cross-polarized omnidirectional elements. Signal-to-noise ratios (SNRs) are fixed at certain values to investigate the SE achieved by the 3GPP [64] and NYUSIM models described in [3] and Section 3 of this user manual. Two hundred random channel realizations using random distances ranging from 10 to 435 m were performed for each channel model, where the NYUSIM code runs about 30 times faster than the 3GPP code.

Fig. 4.3 illustrates the SE achieved by the hybrid beamforming algorithm proposed in [90] for a 256×16 mmWave system at 28 GHz with rectangular planar arrays at the transmitter and receiver for various numbers of data streams N_s, using the 3GPP and NYUSIM models. As shown by Fig. 4.3, the SE generated by the 3GPP channel model is just slightly smaller than that yielded by the NYUSIM channel model for $N_s = 1$, but much larger for $N_s = 4$. For instance, for an SNR of 20 dB and $N_s = 4$, the 3GPP SE (40 bits/s/Hz) is about 13 bits/s/Hz greater than the NYUSIM SE (about 27
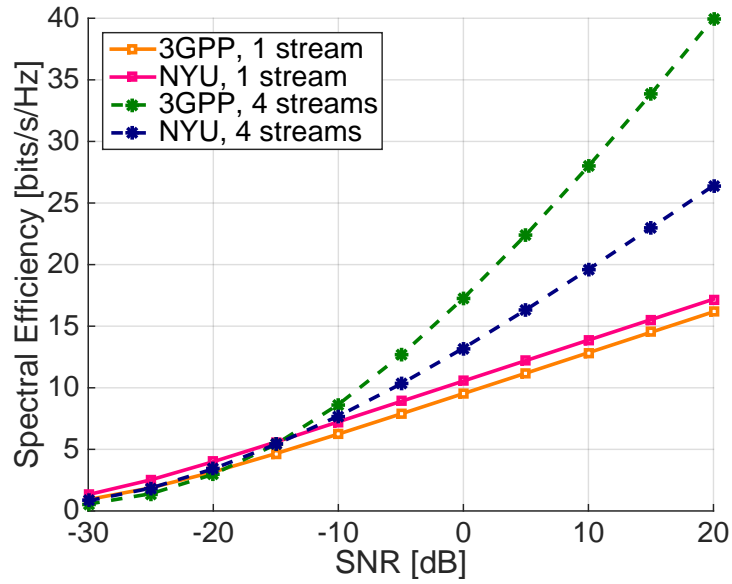
FIGURE 4.3: Spectral efficiency achieved by hybrid beamforming for a 256×16 system at 28 GHz with rectangular antenna arrays at the transmitter and receiver with four RF chains.

bits/s/Hz). This is likely because NYUSIM yields one or two strong dominant clusters and much weaker non-dominant clusters, while the 3GPP model has less focused directional energy than what realistically exists. The results indicate that the 3GPP channel model is optimistic when predicting diversity and the achievable SE at mmWave frequencies, while NYUSIM provides realistic channel parameters and SE predictions due to the use of extensive real-world measurement data at mmWave frequencies, thus could help avoid system errors inherent with legacy modeling approaches.

4.3 Application 3: Temporal Large-scale Path Loss Variation Due to Spatial Consistency

Spatial consistency is used for simulating the changing channel conditions of a user as it moves in a local area, or may be used to generate correlated channels for closely-spaced users (as opposed to independent responses generated from the drop-based mode). As an example of spatial consistency mode in NYUSIM, time-variant large-scale path loss based on the UT trajectory is calculated using the map of spatially correlated shadow fading and UT and BS locations. A map of spatially correlated shadow fading over a 200 m x 200 m area is shown in Fig. 4.4. The correlation distance of shadow fading in a UMi LOS scenario is set to be 10 m [16], [44]. The UT moved 40 m in a partial hexagon track, which is also illustrated in Fig. 4.4. Shadow fading varies from -10 dB to 10 dB in a continuous manner. Similar shadow fading values are observed at closely spaced locations whereas independent values for close locations are always used in the drop-based model.
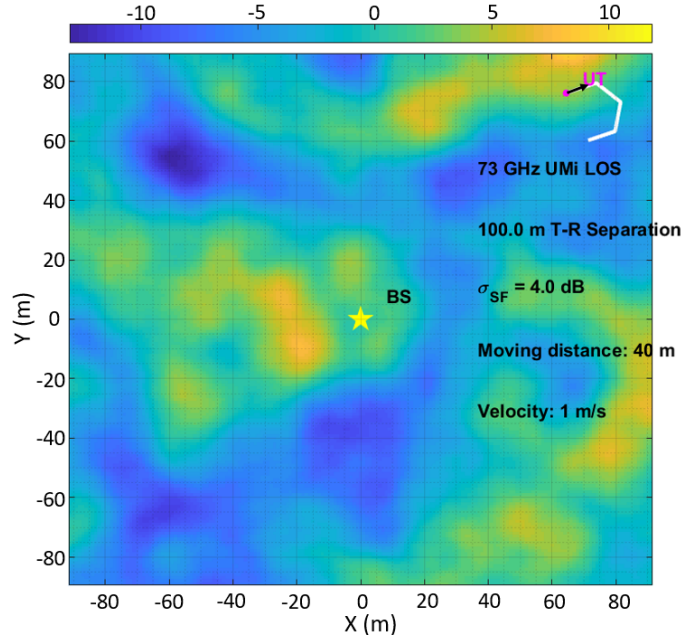
FIGURE 4.4: A map of spatially correlated shadow fading with the BS and UT locations. The map of spatially correlated shadow fading is generated by filtering a map of independent shadow fading using an exponential function in (3.5). Shadow fading [dB]~N(0,4) in a UMi LOS scenario. T-R separation distance is 100 m.

The time-variant path loss is shown in Fig. 4.5 [16], [45]. It can be seen that the path loss varies rapidly about 16 dB with independent shadow fading values. However, the path loss varies smoothly with spatially correlated shadow fading, which corresponds to the UT trajectory. The path loss increases first and then drops as the UT first moves away from the base station and then comes back. Spatially correlated shadow fading supports a more realistic link budget analysis and cellular coverage prediction.

FIGURE 4.5: The UT moves in a partial hexagon track in a clockwise manner. The track distance is 40 m, the side length of the hexagon is 10 m.

4.4 Application 4: Human Blockage Shadowing Loss Simulations
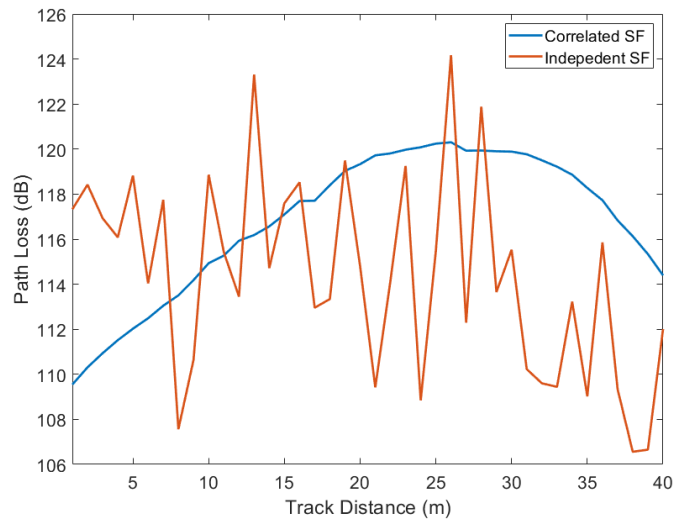
To investigate the human blockage effect on directional channels generated from NYUSIM, four sets of TX and RX antennas with HPBW 7°, 15°, 30°, and 60° are selected in a UMi scenario at 73 GHz. The T-R separation distance ranges from 100 m to 500 m. 1000 simulations (i.e. 1000 UT locations) are performed for each TX and RX antenna setting. A comparison of CDFs of shadowing loss for directional channels in the UMi NLOS scenario using four sets of TX and RX antennas with HPBW 7°, 15°, 30°, and 60° is shown in Fig. 4.6 [16], [45]. UTs equipped with narrower HPBW antennas are more likely to experience severe blockage shadowing loss. 31% of UTs equipped with 7° HPBW antenna experience more than 15 dB shadowing loss.
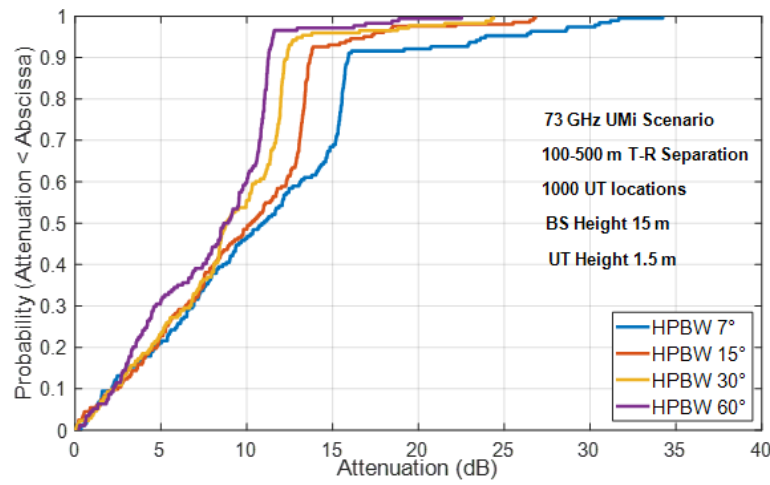
FIGURE 4.6: CDFs of simulated human blockage shadowing loss using the four-state Markov model for directional channels with RX antenna azimuth HPBWs (7°, 15°, 30°, and 60°.

4.5 Application 5: O2I Penetration Loss Simulations

The O2I feature will be turned on if the option "Outdoor to Indoor (O2I) Penetration Loss" is "Yes" under the drop-based mode, as shown in Fig. 4.7.This application is used for simulating the channel responses for users inside buildings.

The simulated O2I penetration loss value can be read from the omnidirectional and directional PDPs, as shown in Fig. 4.8 and Fig. 4.9. There is an additional 15.0 dB O2I penetration loss added to the total path loss.

FIGURE 4.7: An example of NYUSIM run with O2I penetration loss.

FIGURE 4.8: Omnidirectional PDP output from a NYUSIM run with 15.0 dB O2I penetration loss.
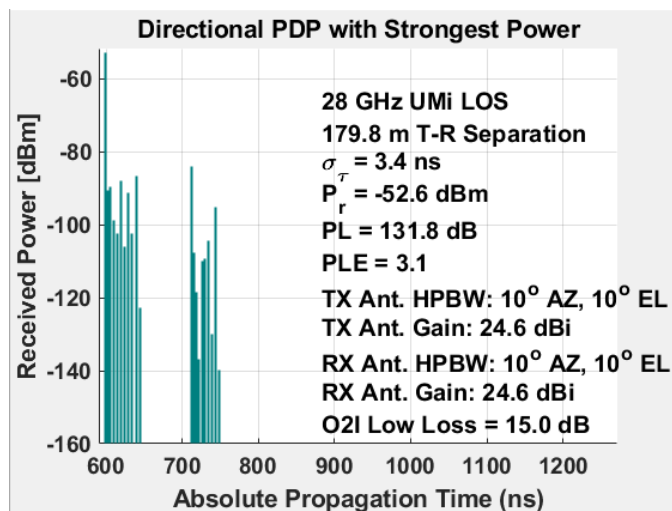
FIGURE 4.9: Directional PDP output from a NYUSIM run with 15.0 dB O2I penetration loss.

Apart from the example demonstrated above, NYUSIM can also find applications in other types of analysis, such as the design of antenna arrays [91] and bit error simulation [22], [92].

4.6   Application 6: Indoor Coverage Prediction

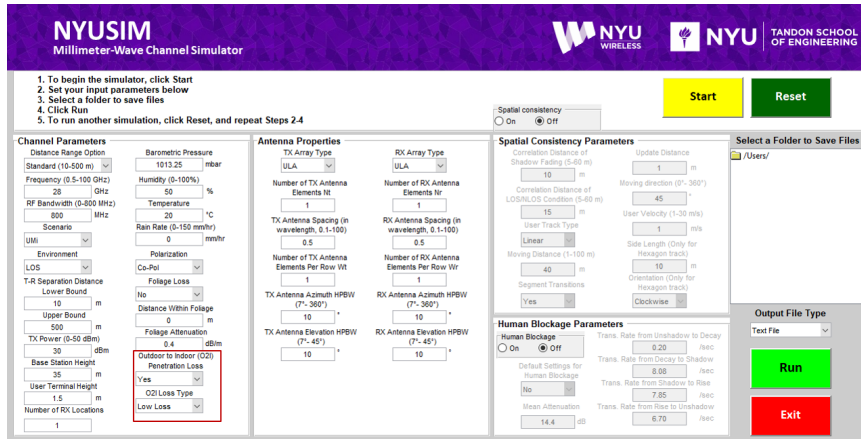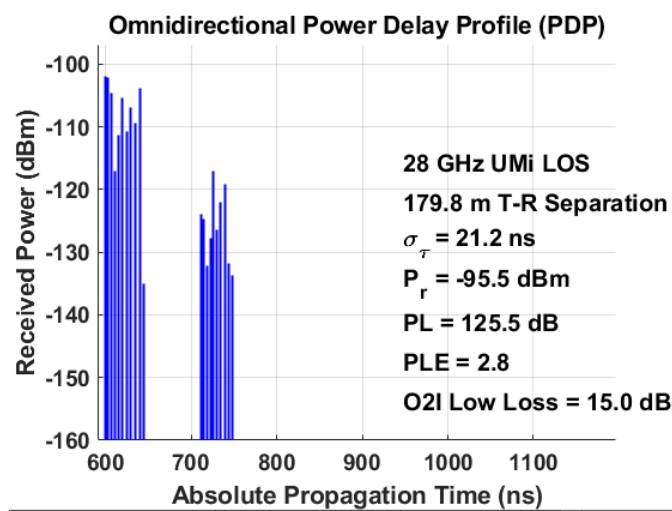The prediction of the coverage of an indoor WiFi hotspot is crucial for the deployment of large WiFi networks. Due to the increasing path loss within the first meter of propagation distance at sub-THz frequencies, the cell size shrinks and the ultra dense network is required to provide sufficient link margin. Here we show an example of using NYUSIM 3.0 to predict the typical coverage of a sub-THz indoor wireless system. The input parameters on the NYUSIM are set with the following values:

- Frequency: 140 GHz

- RF bandwidth: 800 MHz

- Scenario: InH

- Distance Range Option: Indoor (5-50 m)

- Environment: LOS and NLOS

- Lower Bound of T-R Separation Distance: 5 m

- Upper Bound of T-R Separation Distance: 50 m

- TX Power: 10 dBm

- Base Station Height: 2.5 m

- Polarization: Co-Pol

- Number of RX Locations: 100 in LOS and 100 in NLOS

- TX Array Type: URA

- RX Array Type: URA

- Number of TX Antenna Elements N_t: 16

- Number of RX Antenna Elements N_r: 4

- TX Antenna Spacing: 0.5 wavelength

- RX Antenna Spacing: 0.5 wavelength

- Number of TX Antenna Elements Per Row W_t: 4

- Number of RX Antenna Elements Per Row W_r: 2

- TX Antenna Azimuth HPBW: 10°

- TX Antenna Elevation HPBW: 10°

- RX Antenna Azimuth HPBW: 30°

- RX Antenna Elevation HPBW: 30°

We assume the receiver sensitivity of a mobile receiver under the WLAN compliance is -82 dBm. Fig. 4.10 shows the scatter plot of the received powers and the average power level of the received signals at distances from 5 to 50 m for indoor directional channels in both LOS and NLOS environments. Antenna arrays providing narrow beams with HPBW beamwidths of 10° and 30° are used at the transmitter and receiver, respectively, which can provide good directional gains and eliminate interference from communication links of other hotspots or mobile devices. The TX and RX beams are pointed in the boresight direction in the LOS environment while the beams are pointed in the strongest reflection direction in the NLOS environment. Fig. 4.10 suggests that the receiver maintains a sufficient SNR level for distances even beyond 50 m in the LOS environment. However, in the NLOS environment, the received power drops below the receiver sensitivity (-82 dBm) at the separation distance of 35.8 m when the TX and RX antennas are pointed to the strongest reflection direction, indicating the potential usage of multi-beam antenna combing [93] and reconfigurable intelligent surfaces [94] to extend the signal coverage.
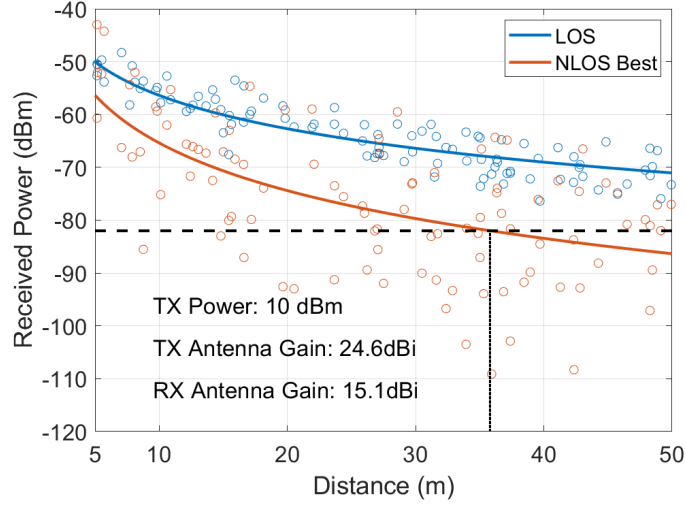

FIGURE 4.10: Scatter plot of the received powers and the average power level of the received signals at distances from 5 to 50 m for LOS and NLOS indoor directional channels. For the NLOS environment, the average power level of received signals drops below the receiver sensitivity beyond 35.8 m.

Bibliography

[1] T. S. Rappaport, S. Sun, R. Mayzus, H. Zhao, Y. Azar, K. Wang, G. N. Wong, J. K. Schulz, M. Samimi, and F. Gutierrez, "Millimeter wave mobile communications for 5G cellular: It will work!" *IEEE Access*, vol. 1, pp. 335–349, 2013. [Online]. Available: http://ieeexplore.ieee.org/document/6515173/.

[2] T. S. Rappaport, G. R. MacCartney, Jr., M. K. Samimi, and S. Sun, "Wideband millimeter-wave propagation measurements and channel models for future wireless communication system design (*Invited Paper*)," *IEEE Transactions on Communications*, vol. 63, no. 9, pp. 3029–3056, Sep. 2015. [Online]. Available: http://ieeexplore.ieee.org/document/7109864/.

[3] M. K. Samimi and T. S. Rappaport, "3-D millimeter-wave statistical channel model for 5G wireless system design," *IEEE Transactions on Microwave Theory and Techniques*, vol. 64, no. 7, pp. 2207–2225, Jul. 2016. [Online]. Available: http://ieeexplore.ieee.org/document/7501500/.

[4] ——, "Local multipath model parameters for generating 5G millimeter-wave 3GPP-like channel impulse response," *the 10th European Conference on Antennas and Propagation (EuCAP 2016)*, Apr. 2016. [Online]. Available: http://arxiv.org/abs/1511.06941.

[5] S. Sun *et al.*, "Investigation of prediction accuracy, sensitivity, and parameter stability of large-scale propagation path loss models for 5G wireless communications," *IEEE Transactions on Vehicular Technology*, vol. 65, no. 5, pp. 2843–2860, May 2016. [Online]. Available: http://ieeexplore.ieee.org/document/7434656/.

[6] S. Sun, G. R. MacCartney, M. K. Samimi, and T. S. Rappaport, "Synthesizing omnidirectional antenna patterns, received power and path loss from directional antennas for 5G millimeter-wave communications," in *2015 IEEE Global Communications Conference (GLOBECOM)*, Dec. 2015, pp. 1–7. [Online]. Available: http://arxiv.org/abs/1511.07271.

[7] G. R. MacCartney, Jr., T. S. Rappaport, S. Sun, and S. Deng, "Indoor office wideband millimeter-wave propagation measurements and channel models at 28 and 73 GHz for ultra-dense 5G wireless networks," *IEEE Access*, vol. 3, pp. 2388–2424, 2015. [Online]. Available: http://ieeexplore.ieee.org/document/7289335/.

[8] T. S. Rappaport, S. Sun, and M. Shafi, "Investigation and comparison of 3GPP and NYUSIM channel models for 5G wireless communications," in *2017 IEEE 86th Vehicular Technology Conference (VTC-Fall)*, Sep. 2017, pp. 1–5. [Online]. Available: https://arxiv.org/pdf/1707.00291.pdf.

[9] G. R. MacCartney, Jr., S. Sun, T. S. Rappaport, Y. Xing, H. Yan, J. Koka, R. Wang, and D. Yu, "Millimeter wave wireless communications: New results for rural connectivity," in *All Things Cellular'16, in conjunction with ACM MobiCom*, Oct. 2016. [Online]. Available: https://arxiv.org/abs/1608.05384.

[10] "Investigation of prediction accuracy, sensitivity, and parameter stability of large-scale propagation path loss models from 500 MHz to 100 GHz," [Online]. Available: http://wireless.engineering.nyu.edu/presentations/NTIA-propagation-presentation-JUNE-15-2016_v1-3.pdf.

[11] T. S. Rappaport, S. Sun, and M. Shafi, "5G channel model with improved accuracy and efficiency in mmWave bands," *IEEE 5G Tech Focus*, vol. 1, no. 1, Mar. 2017. [Online]. Available: https://5g.ieee.org/tech-focus/march-2017/5g-channel-model.

[12] G. R. MacCartney and T. S. Rappaport, "Rural macrocell path loss models for millimeter wave wireless communications," *IEEE Journal on Selected Areas in Communications*, vol. 35, no. 7, pp. 1663–1677, Jul. 2017. [Online]. Available: http://ieeexplore.ieee.org/stamp/stamp.jsp?tp=&arnumber=7914696.

[13] S. Sun, G. R. MacCartney, and T. S. Rappaport, "A novel millimeter-wave channel simulator and applications for 5G wireless communications," in *2017 IEEE International Conference on Communications (ICC)*, May 2017, pp. 1–7. [Online]. Available: https://arxiv.org/pdf/1703.08232.pdf.

[14] S. Ju and T. S. Rappaport, "Simulating motion - incorporating spatial consistency into the NYUSIM channel model," *2018 IEEE 88th Vehicular Technology Conference Workshops*, pp. 1–6, Aug. 2018.

[15] ——, "Millimeter-wave extended nyusim channel model for spatial consistency," *2018 IEEE Global Communications Conference (Globecom)*, pp. 1–6, Dec. 2018.

[16] S. Ju, Y. Xing, O. Kanhere, and T. S. Rappaport, "A Millimeter-Wave Channel Simulator NYUSIM with Spatial Consistency and Human Blockage," *IEEE 2019 Global Communications Conference*, pp. 1–6, Dec. 2019.

[17] ——, "3-D Statistical Indoor Channel Model for Millimeter-Wave and Sub-Terahertz Bands," *IEEE 2020 Global Communications Conference*, pp. 1–7, Dec. 2020.

[18] S. Ju, Y. Xing, O. Kanhere, and T. S. Rappaport, "Millimeter wave and sub-Terahertz spatial statistical channel model for an indoor office building," *IEEE Journal on Selected Areas in Communications, Special Issue on TeraHertz Communications and Networking*, pp. 1–15, Second Quarter 2021.

[19] Y. Xing and T. S. Rappaport, "Spectrum coexistence between active and passive systems in space and on the ground at frequencies above 100 ghz (invited)," *in submission to IEEE Communications Letters*, pp. 1–5, Feb. 2021.

[20] Y. Xing, T. S. Rappaport, and A. Ghosh, "Millimeter wave and sub-thz indoor radio propagation channel measurements, models, and comparisons in an office environment (invited)," *in submission to IEEE Communications Letters*, pp. 1–5, Feb. 2021.

[21] Y. Xing and T. S. Rappaport, "Propagation Measurements and Path Loss models for sub-THz in Urban Microcells," *submitted to 2021 IEEE International Conference on Communications (ICC)*, pp. 1–5, Jun. 2021.

[22] V. Fung, T. S. Rappaport, and B. Thoma, "Bit error simulation for pi/4 DQPSK mobile radio communications using two-ray and measurement-based impulse response models," *IEEE Journal on Selected Areas in Communications*, vol. 11, no. 3, pp. 393–405, Apr. 1993. [Online]. Available: http://ieeexplore.ieee.org/document/219546/.

[23] J. C. Liberti and T. S. Rappaport, "Analysis of CDMA cellular radio systems employing adaptive antennas in multipath environments," in *IEEE 46th Vehicular Technology Conference*, vol. 2, Apr. 1996, pp. 1076–1080. [Online]. Available: http://ieeexplore.ieee.org/document/501477/.

[24] J. Lota, S. Sun, T. S. Rappaport, and A. Demosthenous, "5G uniform linear arrays with beamforming and spatial multiplexing at 28, 37, 64, and 71 GHz for outdoor urban communication: A two-level approach," *IEEE Transactions on Vehicular Technology*, vol. 66, no. 11, pp. 9972–9985, Nov. 2017. [Online]. Available: http://ieeexplore.ieee.org/document/8012543/.

[25] M. K. Samimi and T. S. Rappaport, "3-D millimeter-wave statistical channel model for 5G wireless system design," *IEEE Transactions on Microwave Theory and Techniques*, vol. 64, no. 7, pp. 2207–2225, Jul. 2016.

[26] 3GPP, "Study on channel model for frequencies from 0.5 to 100 GHz," 3rd Generation Partnership Project (3GPP), TR 38.901 V14.1.1, Jul. 2017. [Online]. Available: https://portal.3gpp.org/desktopmodules/Specifications/SpecificationDetails.aspx?specificationId=3173.

[27] S. Sun, T. S. Rappaport, M. Shafi, P. Tang, J. Zhang, and P. J. Smith, "Propagation models and performance evaluation for 5G millimeter-wave bands," *IEEE Transactions on Vehicular Technology*, vol. 67, no. 9, pp. 8422–8439, Sep. 2018.

[28] S. Sun, T. S. Rappaport, M. Shafi, and H. Tataria, "Analytical framework of hybrid beamforming in multi-cell millimeter-wave systems," *IEEE Transactions on Wireless Communications*, vol. 17, no. 11, pp. 7528–7543, Nov. 2018.

[29] T. Manabe, K. Sato, H. Masuzawa, K. Taira, T. Ihara, Y. Kasashima, and K. Yamaki, "Polarization dependence of multipath propagation and high-speed transmission characteristics of indoor millimeter-wave channel at 60 ghz," *IEEE Transactions on Vehicular Technology*, vol. 44, no. 2, pp. 268–274, 1995.

[30] Y. Xing, O. Kanhere, S. Ju, and T. S. Rappaport, "Indoor Wireless Channel Properties at Millimeter Wave and Sub-Terahertz Frequencies," *IEEE 2019 Global Communications Conference*, pp. 1–6, Dec. 2019.

[31] Y. Xing and T. S. Rappaport, "Propagation measurement system and approach at 140 ghz–moving to 6g and above 100 ghz," in *2018 IEEE Global Communications Conference (GLOBECOM)*, Dec. 2018, pp. 1–6.

[32] A. Maltsev *et al.*, "Impact of polarization characteristics on 60-GHz indoor radio communication systems," *IEEE Antennas and Wireless Propagation Letters*, vol. 9, pp. 413–416, May 2010.

[33] J.-M. Molina-Garcia-Pardo, J.-V. Rodriguez, and L. Juan-Llacer, "Polarized indoor mimo channel measurements at 2.45 ghz," *IEEE Transactions on Antennas and Propagation*, vol. 56, no. 12, pp. 3818–3828, 2008.

[34] A. Jagannatham and V. Erceg, "Mimo indoor wlan channel measurements and parameter modeling at 5.25 ghz," in *IEEE 60th Vehicular Technology Conference, 2004. VTC2004-Fall. 2004*, vol. 1, 2004, 106–110 Vol. 1.

[35] P. Zhang, J. Li, H. Wang, H. Wang, and W. Hong, "Indoor small-scale spatiotemporal propagation characteristics at multiple millimeter-wave bands," *IEEE Antennas and Wireless Propagation Letters*, vol. 17, no. 12, pp. 2250–2254, 2018.

[36] D. Solomitckii, M. Allén, D. Yolchyan, H. Hovsepyan, M. Valkama, and Y. Koucheryavy, "Millimeter-wave channel measurements at 28 ghz in digital fabrication facilities," in *2019 16th International Symposium on Wireless Communication Systems (ISWCS)*, 2019, pp. 548–552.

[37] M. Khalily, S. Taheri, S. Payami, M. Ghoraishi, and R. Tafazolli, "Indoor wideband directional millimeter wave channel measurements and analysis at 26 ghz, 32 ghz, and 39 ghz," *Transactions on Emerging Telecommunications Technologies*, vol. 29, no. 10, e3311, 2018.

[38] D. He, B. Ai, K. Guan, Z. Zhong, B. Hui, J. Kim, H. Chung, and I. Kim, "Channel measurement, simulation, and analysis for high-speed railway communications in 5g millimeter-wave band," *IEEE Transactions on Intelligent Transportation Systems*, vol. 19, no. 10, pp. 3144–3158, 2018.

[39] X. Liu, X. Yin, and G. Zheng, "Experimental investigation of millimeter-wave mimo channel characteristics in tunnel," *IEEE Access*, vol. 7, pp. 108 395–108 399, 2019.

[40] S. Sun, T. S. Rappaport, R. W. Heath, A. Nix, and S. Rangan, "Mimo for millimeter-wave wireless communications: Beamforming, spatial multiplexing, or both?" *IEEE Communications Magazine*, vol. 52, no. 12, pp. 110–121, 2014.

[41] 3GPP, "Technical specification group radio access network; study on channel model for frequencies from 0.5 to 100 GHz (Release 16)," TR 38.901 V16.0.0, Oct. 2019.

[42] A. Maltsev *et al.*, "Channel models for IEEE 802.11ay," doc.: IEEE 802.11-15/1150r9, May 2016.

[43] S. Ju and T. S. Rappaport, "Simulating motion - incorporating spatial consistency into the NYUSIM channel model," *2018 IEEE 88th Vehicular Technology Conference Workshops*, pp. 1–6, Aug. 2018.

[44] ——, "Millimeter-wave extended NYUSIM channel model for spatial consistency," *2018 IEEE Globecom*, pp. 1–6, Dec. 2018.

[45] S. Ju, "Channel modeling and channel simulation for fifth-generation and beyond millimeter-wave wireless communications," Ph.D. dissertation, NEW YORK UNIVERSITY, TANDON SCHOOL OF ENGINEERING, May 2019.

[46] G. R. MacCartney, T. S. Rappaport, and S. Rangan, "Rapid fading due to human blockage in pedestrian crowds at 5G millimeter-wave frequencies," in *2017 IEEE Global Communications Conference*, Dec. 2017, pp. 1–7.

[47] G. R. MacCartney *et al.*, "Millimeter-wave base station diversity for 5G coordinated multipoint (CoMP) applications," *IEEE Transactions on Wireless Communications*, May 2019.

[48] T. S. Rappaport *et al.*, "Millimeter Wave Mobile Communications for 5G Cellular: It Will Work!" *IEEE Access*, vol. 1, pp. 335–349, May 2013.

[49] H. Zhao *et al.*, "28 GHz millimeter wave cellular communication measurements for reflection and penetration loss in and around buildings in New York city," in *2013 IEEE International Conference on Communications (ICC)*, Jun. 2013, pp. 5163–5167.

[50] K. Haneda *et al.*, "5G 3GPP-like channel models for outdoor urban microcellular and macrocellular environments," in *2016 IEEE 83rd Vehicular Technology Conference (VTC2016-Spring)*, May 2016, pp. 1–7.

[51] Aalto University, AT&T, BUPT, CMCC, Ericsson, Huawei, Intel, KT Corporation, Nokia, NTT DOCOMO, New York University, Qualcomm, Samsung, University of Bristol, and University of Southern California, "5G channel model for bands up to 100 GHz," 2016, Oct. 21. [Online]. Available: http://www.5gworkshops.com/5GCM.html.

[52] H. J. Liebe, G. A. Hufford, and M. G. Cotton, "Propagation modeling of moist air and suspended water/ice particles at frequencies below 1000 GHz," *AGARD Conference Proceedings 542*, May 1993. [Online]. Available: http://www.its.bldrdoc.gov/publications/2670.aspx.

[53] J. J. A. Lempianen, J. K. Laiho-Steffens, and A. F. Wacker, "Experimental results of cross polarization discrimination and signal correlation values for a polarization diversity scheme," in *IEEE 47th Vehicular Technology Conference*, vol. 3, May 1997, pp. 1498–1502. [Online]. Available: http://ieeexplore.ieee.org/document/605617/.

[54] H.-l. Xiao, S. Ouyang, and Z.-p. Nie, "The cross polarization discrimination of MIMO antennas at mobile station," in *International Conference on Communications, Circuits and Systems (ICCCAS)*, May 2008, pp. 203–206. [Online]. Available: http://ieeexplore.ieee.org/document/4657759/.

[55] T. S. Rappaport and S. Deng, "73 GHz wideband millimeter-wave foliage and ground reflection measurements and models," in *2015 IEEE International Conference on Communication Workshop (ICCW)*, Jun. 2015, pp. 1238–1243. [Online]. Available: https://arxiv.org/pdf/1509.00436.

[56] K. Haneda *et al.*, "Indoor 5G 3GPP-like channel models for office and shopping mall environments," in *2016 IEEE International Conference on Communications Workshops (ICCW)*, May 2016, pp. 694–699.

[57] T. S. Rappaport and R. A. Brickhouse, "A simulation of cellular system growth and its effect on urban in-building parasitic frequency reuse," *IEEE Transactions on Vehicular Technology*, vol. 48, no. 1, pp. 286–294, Jan. 1999. [Online]. Available: http://ieeexplore.ieee.org/document/740107/.

[58] T. Bai, A. Alkhateeb, and R. W. Heath, "Coverage and capacity of millimeter-wave cellular networks," *IEEE Communications Magazine*, vol. 52, no. 9, pp. 70–77, Sep. 2014. [Online]. Available: http://ieeexplore.ieee.org/document/6894455/.

[59] G. R. MacCartney, Jr., T. S. Rappaport, and S. Rangan, "Rapid fading due to human blockage in pedestrian crowds at 5g millimeter-wave frequencies," in *2017 IEEE Global Communications Conference (GLOBECOM)*, Dec. 2017, pp. 1–7.

[60] A. Alkhateeb and R. W. Heath, "Frequency selective hybrid precoding for limited feedback millimeter wave systems," *IEEE Transactions on Communications*, vol. 64, no. 5, pp. 1801–1818, May 2016. [Online]. Available: http://ieeexplore.ieee.org/document/7448873/.

[61] A. I. Sulyman, A. T. Nassar, M. K. Samimi, G. R. Maccartney, T. S. Rappaport, and A. Alsanie, "Radio propagation path loss models for 5G cellular networks in the 28 GHz and 38 GHz millimeter-wave bands," *IEEE Communications Magazine*, vol. 52, no. 9, pp. 78–86, Sep. 2014. [Online]. Available: http://ieeexplore.ieee.org/document/6894456/.

[62] A. I. Sulyman, A. Alwarafy, G. R. MacCartney, T. S. Rappaport, and A. Alsanie, "Directional radio propagation path loss models for millimeter-wave wireless networks in the 28-, 60-, and 73-GHz bands," *IEEE Transactions on Wireless Communications*, vol. 15, no. 10, pp. 6939–6947, Oct. 2016. [Online]. Available: http://ieeexplore.ieee.org/document/7522613/.

[63] T. S. Rappaport, R. W. Heath, Jr., R. C. Daniels, and J. N. Murdock, *Millimeter Wave Wireless Communications*. Pearson/Prentice Hall 2015.

[64] 3GPP, "Study on channel model for frequency spectrum above 6 GHz," 3rd Generation Partnership Project (3GPP), TR 38.900 V14.2.0, Dec. 2016. [Online]. Available: http://www.3gpp.org/DynaReport/38900.htm.

[65] T. S. Rappaport *et al.*, "Wideband millimeter-wave propagation measurements and channel models for future wireless communication system design (Invited Paper)," *IEEE Transactions on Communications*, vol. 63, no. 9, pp. 3029–3056, Sep. 2015.

[66] J. Ko, S. U. Lee, Y. S. Kim, and D.-J. Park, "Measurements and analyses of 28 GHz indoor channel propagation based on a synchronized channel sounder using directional antennas," *Journal of Electromagnetic Waves and Applications*, vol. 30, no. 15, pp. 2039–2054, Jun. 2016.

[67] Hao Xu, V. Kukshya, and T. S. Rappaport, "Spatial and temporal characteristics of 60-GHz indoor channels," *IEEE Journal on Selected Areas in Communications*, vol. 20, no. 3, pp. 620–630, Apr. 2002.

[68] L. Rubio *et al.*, "Wideband propagation channel measurements in an indoor office environment at 26 GHz," in *2019 IEEE International Symposium on Antennas and Propagation and USNC-URSI Radio Science Meeting*, Oct. 2019, pp. 2075–2076.

[69] A. Saleh and R. A. Valenzuela, "A statistical model for indoor multipath propagation," *IEEE Journal on Selected Areas in Communications*, vol. 5, no. 2, pp. 128–137, Feb. 1987.

[70] 3GPP, "Technical specification group radio access network; study on channel model for frequencies from 0.5 to 100 GHz (Release 15)," 3rd Generation Partnership Project (3GPP), TR 25.104 V15.4.0, Sep. 2018. [Online]. Available: http://www.3gpp.org/DynaReport/25104.htm.

[71] METIS, "METIS Channel Model," METIS2020, Deliverable D1.4 v3, Jul. 2015.

[72] T. S. Rappaport *et al.*, "Overview of millimeter wave communications for fifth-generation (5G) wireless networks - with a focus on propagation models," *IEEE Transactions on Antennas and Propagation*, vol. 65, no. 12, pp. 6213–6230, Dec. 2017.

[73] F. Ademaj, M. K. Mueller, S. Schwarz, and M. Rupp, "Modeling of spatially correlated geometry-based stochastic channels," in *2017 IEEE 86th Vehicular Technology Conference (VTC-Fall)*, Sep. 2017, pp. 1–6.

[74] Z. Wang, H. Liu, S. Xu, X. Bu, and J. An, "A diffraction measurement model and particle filter tracking method for RSS-based DFL," *IEEE Journal on Selected Areas in Communications*, vol. 33, no. 11, pp. 2391–2403, Nov. 2015.

[75] Y. Wang, Z. Shi, L. Huang, Z. Yu, and C. Cao, "An extension of spatial channel model with spatial consistency," in *2016 IEEE 84th Vehicular Technology Conference (VTC-Fall)*, Sep. 2016, pp. 1–5.

[76] 3GPP, "Discussion on procedure a for spatially-consistency ut mobility modeling," ZTE, TDOC R1-1707267, May 2017.

[77] P. Kyösti *et al.*, "WINNER II channel models," European Commission, IST-WINNER, D1.1.2 V1.2, Feb. 2008. [Online]. Available: http://projects.celticinitiative.org/winner+/WINNER2-Deliverables/.

[78] G. R. MacCartney, Jr. and T. S. Rappaport, "A flexible millimeter-wave channel sounder with absolute timing," *IEEE Journal on Selected Areas in Communications*, vol. 35, no. 6, pp. 1402–1418, Jun. 2017.

[79] G. R. MacCartney, Jr. *et al.*, "Millimeter-wave human blockage at 73 GHz with a simple double knife-edge diffraction model and extension for directional antennas," in *2016 IEEE 84th Vehicular Technology Conference (VTC2016-Fall)*, Sep. 2016, pp. 1–6.

[80] G. R. MacCartney, Jr. and T. S. Rappaport, "Study on 3GPP rural macrocell path loss models for millimeter wave wireless communications," in *2017 IEEE International Conference on Communications (ICC)*, May 2017, pp. 1–7.

[81] M. Jacob and T. Kürner, "Measurement campaign at 60 GHz in the living room environment at TUBS," doc.: IEEE 802.11-11-09-0743-00-00ad r0, Jul. 2009.

[82] G. R. MacCartney *et al.*, "Millimeter-wave base station diversity for 5g coordinated multipoint (comp) applications," *IEEE Transactions on Wireless Communications*, May 2019.

[83] Q. H. Abbasi, H. E. Sallabi, E. Serpedin, K. Qaraqe, and A. Alomainy, "Condition number variability of ultra wideband MIMO on body channels," in *2016 International Workshop on Antenna Technology (iWAT)*, Feb. 2016, pp. 167–169. [Online]. Available: http://ieeexplore.ieee.org/document/7434833/.

[84] R. W. Heath and D. J. Love, "Multimode antenna selection for spatial multiplexing systems with linear receivers," *IEEE Transactions on Signal Processing*, vol. 53, no. 8, pp. 3042–3056, Aug. 2005. [Online]. Available: http://ieeexplore.ieee.org/document/1468498/.

[85] X. Lu, J. Wu, X. Huang, W. Li, J. Lu, and Z. Gong, "An improved semi-orthogonal user selection algorithm based on condition number for multiuser MIMO systems," *China Communications*, vol. 11, no. 13, pp. 23–30, Supplement 2014. [Online]. Available: http://ieeexplore.ieee.org/document/7022522/.

[86] N. Bourbaki, *Elements of Mathematics, Algebra I*. Hermann 1974.

[87] M. Matthaiou, D. I. Laurenson, and C. X. Wang, "Reduced complexity detection for ricean MIMO channels based on condition number thresholding," in *2008 International Wireless Communications and Mobile Computing Conference*, Aug. 2008, pp. 988–993. [Online]. Available: http://ieeexplore.ieee.org/document/4600070/.

[88] S. Sun, T. S. Rappaport, R. W. Heath, A. Nix, and S. Rangan, "MIMO for millimeter-wave wireless communications: Beamforming, spatial multiplexing, or both?" *IEEE Communications Magazine*, vol. 52, no. 12, pp. 110–121, Dec. 2014. [Online]. Available: http://ieeexplore.ieee.org/document/6979962/.

[89] A. Adhikary, E. A. Safadi, M. K. Samimi, R. Wang, G. Caire, T. S. Rappaport, and A. F. Molisch, "Joint spatial division and multiplexing for mm-wave channels," *IEEE Journal on Selected Areas in Communications*, vol. 32, no. 6, pp. 1239–1255, Jun. 2014. [Online]. Available: http://ieeexplore.ieee.org/document/6823686/.

[90] O. E. Ayach, S. Rajagopal, S. Abu-Surra, Z. Pi, and R. W. Heath, "Spatially sparse precoding in millimeter wave MIMO systems," *IEEE Transactions on Wireless Communications*, vol. 13, no. 3, pp. 1499–1513, Mar. 2014. [Online]. Available: http://ieeexplore.ieee.org/document/6717211/.

[91] R. B. Ertel, P. Cardieri, K. W. Sowerby, T. S. Rappaport, and J. H. Reed, "Overview of spatial channel models for antenna array communication systems," *IEEE Personal Communications*, vol. 5, no. 1, pp. 10–22, Feb. 1998. [Online]. Available: http://ieeexplore.ieee.org/document/656151/.

[92] B. Thoma, T. S. Rappaport, and M. D. Kietz, "Simulation of bit error performance and outage probability of pi/4 DQPSK in frequency-selective indoor radio channels using a measurement-based channel model," in *IEEE Global Telecommunications Conference (GLOBECOM)*, Dec. 1992, 1825–1829 vol.3. [Online]. Available: http://ieeexplore.ieee.org/document/276698/.

[93] S. Sun *et al.*, "Millimeter wave multi-beam antenna combining for 5G cellular link improvement in New York City," in *2014 IEEE International Conference on Communications (ICC)*, Jun. 2014, pp. 5468–5473.

[94] I. Yoo, M. F. Imani, T. Sleasman, H. D. Pfister, and D. R. Smith, "Enhancing capacity of spatial multiplexing systems using reconfigurable cavity-backed metasurface antennas in clustered mimo channels," *IEEE Transactions on Communications*, vol. 67, no. 2, pp. 1070–1084, 2019.